

eman ta zabal zazu



Universidad del País Vasco
Euskal Herriko Unibertsitatea
The University of the Basque Country

DOCTORAL PROGRAMME IN PHYSICS OF NANOSTRUCTURES AND ADVANCED
MATERIALS.

ALD PROCESSES DEVELOPMENT FOR HYBRID NANODEVICES-LIKE NANOSTRUCTURES.

By

Mabel Andrea Moreno Araneda

Chemical Engineer.

MSc. In chemistry.

Tutor: Prof. Dr. José María Pitarke de la Torre.

Advisors: Prof. Dra. Clivia Sotomayor Torres and

Prof. Dr. Guillermo González Moraga.



Dedicated to
My family and A. Aravena-Gross family.

TABLE OF CONTENTS.

	pp
ACKNOWLEDGE	ix
LIST OF TABLES	x
LIST OF FIGURES	xii
ABBREVIATIONS	xxiv
DEFINITIONS	xxvi
ABSTRACT	xxviii

CHAPTER I. INTRODUCTION

1.1 Introduction.....	2
1.2 Hypothesis and Objectives.....	6

CHAPTER II. ALD PROCESSES

2.1 Historical Background of ALD.....	9
2.2 Principle of ALD.....	10
2.3 Materials suitable for ALD.....	15
2.4 Processes performed in an ALD reactor.....	16
2.4.1 Metalation processes of soft molecules and nanostructures.....	17
2.4.2 ALD process.....	20
2.4.3 MLD process.....	22

CHAPTER III. THEORETICAL AND EXPERIMENTAL METHODS

3.1 Density Functional Theory (DFT).....	30
3.2 Experimental Methods.....	33
3.2.1 MALDI-TOF.....	33
3.2.2 NMR.....	35
3.2.3 Infrared and Raman Spectroscopy.....	37
3.2.4 Infrared and Raman Spectroscopy Fundamentals.....	37
3.2.5 UV-visible spectra.	40
3.2.6 Luminescence Properties.....	41

3.2.7 X-ray diffraction (XRD).....	51
3.2.8 X-ray reflectivity (XRR).....	52
3.2.9 Transmission Electron Microscopy (TEM).....	53
3.2.10 Atomic Force Microscopy (AFM).....	56
3.2.11 Nanofabrication Methods.....	56

CHAPTER IV. EXPERIMENTAL PROCEDURE

4.1 IR and NMR spectroscopic correlation of Enterobactin by DFT.....	58
4.2 Zn metalation-VPM of H ₆ EB and FeH ₃ EB.....	68
4.3. Zn metalation-VPM of M _L -NH ₄ V ₇ O ₁₆ square.....	71
4.4. Zn-metalation VPM vs MPI processes of M _W -H ₂ Ti ₃ O ₇ NTs.....	76
4.5 Synthesis of Mn _x O _y , α-V ₂ O ₅ , SnO ₂ ALD.....	79
4.6 Alucones ALD-MLD.....	81

CHAPTER V.

Zn METALATION-VPM AND SPECIFIC BOND FUNCTIONALIZATION: SOFT MOLECULES AND NANOSTRUCTURES

5.1 IR and NMR spectroscopic correlation of H ₆ EB by DFT.....	75
5.2 Zn Metalation-VPM process of H ₆ EB and FeH ₃ EB.....	111
5.3 Zn metalation-VPM process of M _L -NH ₄ V ₇ O ₁₆ square.....	133
5. 4 Conclusion of Zn metalation-VPM process.	159

CHAPTER VI.

H-O AND H-N SPECIFIC BOND FUNCTIONALIZATION AND NPs NUCLEATION BY Zn METALATION VPM vs MPI OF M_W-H₂Ti₃O₇ NTs.

6. Zn-metalation VPM vs MPI processes of M _W -H ₂ Ti ₃ O ₇ NTs.....	161
6.1 T-1 Characterization.....	169
6.2 T-2 Characterizations.....	171
6. 3 T-3 Characterizations.....	176
6.4 Optical Properties.....	180

6.5 Photocatalytic Properties.....	181
6.6 Luminescence Properties.....	182
6.7 Discussion.....	185
6.8 Conclusion.....	187

CHAPTER VII. ALD & MLD PROCESSES

7.1 α -V ₂ O ₅ , MnO ₂ , SnO ₂ and ZnO-ALD.....	186
7. 1.1 α -MnO ₂ ALD.....	192
7.1. 2 α -V ₂ O ₅ ALD.....	196
7.1. 3 Sn _x O _y ALD.....	198
7.1. 4 ZnO ALD.....	201
7.1.5 Nanofabrication.....	200
7.1. 6.MOKE results	202
7. 1.7 Discussion.....	204
7.1.8 Conclusions.....	205
7.2 Alucones ALD-MLD.....	207
7. 2.1 AIO-T ALD-MLD.....	209
7.2.2 AIO-A ALD-MLD.....	238
7.3 Conclusions.....	240

CHAPTER VIII. DISCUSSION.....241

CHAPTER IX.

9.1 Conclusion.....	244
9.2 Future Perspectives.....	246

REFERENCES.....248

ANNEXES.....xxxiv

ACKNOWLEDGMENTS.

I would like to thank my parents; Luis and María for encouraging me to face and overcome the “life challenges”, to my brother and sister; Roberto and Ivonne who supported me economically and emotionally all those large years of education, to Ana Aravena-Gross family to give me the peace and kind love to write my thesis, to my friends and colleagues; Christian, Rodrigo, Ingrid, Geraldine, Leire, Aritz, July, Angela, Miryam, Angélica, Thiago, Sindy, Catherine, Viviane, Melissa and Daniel for their wise advices and help. I thank Dr. M. Knez for giving me the possibility to learn about atomic layer deposition (ALD) reactor and the Nanogune team. I thank; Dra. Andrea Porzel from Leibniz Institute for Biochemical Plants, Dra. A. Zacarias and Prof. Dr. E. K. U. Gross director of Theory department of Max Planck Institute for Microstructure Physics for inviting me to finish part of my thesis in his Department. Extend my gratitude for Prof. Dr. Luis Velasquez director of CIMIS-Chile, Prof. Dr. Fernando Danilo Gonzalez Nilo director of Bioinformatic Center of UAB-Chile, Dra. E. Benavente from UTEM-Chile. I would like also to express my depth gratitude to my supervisors the Prof. Dra. Clivia Sotomayor Torres leader of Photonic and Phononic group (P₂N) from ICN2-Barcelona who suggested a way to structure my PhD. thesis, and my mentor Prof. Dr. Guillermo Gonzalez Moraga, leader of lamellar nanostructures group of Centers for the development of Nanoscience and Nanotechnology (CEDENNA) and Prof. of University of Chile, who believed in me those twelve years, to both for supporting this thesis.

This research was developed and written-up in following research centers: Experimental II and Theory Department from Max Planck Institute for Microstructure Physics (Germany), Leibniz Institute for Biochemical Plant (Germany), Nanocomposite Lab from UTEM-Chile, Inorganic and electrochemical Lab from U. Chile, Bioinformatic Center from UAB-Chile, CIC-Nanogune and ICN2-Barcelona (Spain).

LIST OF TABLES

- Table 2. 1. Some advantages and limitations of a self-limiting film growth in ALD [Puurunen R. L. 2005].
- Table 3.1 Common matrices and stable for MALDI and usable Wavelengths.
- Table 3.2. The principal correlations established through NMR techniques.
- Table 3.3 Some common laser sources for Raman Spectroscopy.
- Table 4.3. Samples “S-1” to “S-4” Summarize.
- Table 4.4. Summary of the nanotubes samples studied.
- Table 4.5 Chemical reagents properties.
- Table 5.1 List of analytes mass/charge ratio of H₆E.B and FeH₃E.B.
- Table 5.2. Experimental ¹³C and ¹H chemical shifts (ppm).
- Table 5.3 Calculated ¹³C and ¹H chemical shifts (ppm) using H₆EB structure-1.
- Table 5.4 Calculated ¹³C and ¹H chemical shifts (ppm) using H₆EB structure-2 and 3.
- Table 5.5. Calculated ¹³C and ¹H chemical shifts (ppm) using H₆EB structure-4 and 5, and average of PBE/QZVP, mPW91/QZVP and mPW91/6-31G DFT-methods.
- Table 5.6 Calculated and experimental ¹³C δ linear correlation results (statistical data).
- Table 5.7. Calculated and experimental ¹H δ linear correlation results (statistical data).
- Table 5.8. Experimental and calculated IR spectra of H₆EB within the range of 2000–4000 cm⁻¹.
- Table 5.9. Experimental and calculated IR spectra of H₆EB within the range of 1000–2000 cm⁻¹.
- Table 5.10. Experimental and calculated IR spectra of H₆EB within the range of 500–1000 cm⁻¹.
- Table 5.11. Calculated and experimental IR PBE-Average linear correlation results (statistical data).
- Table 5.12. Experimental and calculated ¹³C and ¹H chemical shifts (ppm).
- Table 5.13 Amino acid residues localized in the first ligand coordination sphere (at 3 Å).
- Table 5.13 Calculated ¹³C and ¹H chemical shifts (ppm) of model2 and model1+2.
- Table 5.14. Linear correlation result of Zn₃V₃O₈ and ZnO XRD with S- 4, and crystal system data
- Table 6.1 Energy bandgap (E_g) summary.
- Table 6.2 Luminescence peaks of TiO₂ anatase, w-ZnO and T-1, T-2 and T-3 in nm and eV.
- Table 7.1 Crystal cell parameters of some Al_xO_y(OH) structures.
- Table 7.2 AIO-T IR band assignment using DFT models.
- Table 7.3 Excitation energy (nm), oscillator strength (f), excited state and HOMO-LUMO contribution of T.

Table 7.4 Models of AlO-T frontier orbitals (HOMO-LUMO), ΔE_g (energy band-gap), μ (chemical potential), hardness (η), softness (S), A^0 (electron affinity), I^0 (ionization potential), ω - (nucleophilicity index) and ω (electrophilicity index).

Table 7.5. Characteristic modes of the Oh point group

Annex

Table 2.1 S- 3 and 4 IR frequencies and bands assignment. Ref [Markova-Velichkova M. et al 2009, Ni. S. et al 2010]

Table 2.2 S- 2 IR Spectra.

Table 2. 3 S- 3, $\text{NH}_4\text{V}_3\text{O}_8$, NH_4VO_3 and V_2O_5 Raman frequencies and bands assignment.

Table 2.4 S- 3 and 4 surface map Raman spectra.

Table 3.1. The framework structure of $\text{D}_2\text{Ti}_3\text{O}_7$ from 47-0561 JCPDS (To replace 41-192).

Table 3. 2. $\text{H}_2\text{Ti}_3\text{O}_7$ NTs dimensions, interpretation from figure 3.5.

Table 4.1 Model 1-4 and TCl bond distances (\AA).

Table 4.2 Model 1-4 and TCl bond angles ($^\circ$).

Table 4.3 Model 1-4 and TCl dihedral angles ($^\circ$).

Figure 4.1 2ZnO-T Cross-section SEM micrograph; a, b) lamellar overview, and c) EDX-map.

Figure 4.2 2ZnO-EG Cross-section SEM micrograph; a) and b) lamellar overview.

Figure 4.3 V_2O_5 -T cross-section SEM micrograph; a) lamellar nanostructures, and b) EDX- analysis.

Figure 4.4 ZnO-T- SnO_2 cross-section SEM micrograph; a) lamellar nanostructures and b) EDX- analysis.

Figure 4.5 SiO_2 -Cu- Al_2O_3 - SnO_2 (anode)- AlOT (polymer electrolyte)- Mn_xO_y (Cathode) cross-section SEM micrograph; a) lamellar nanostructures and b) EDX- analysis.

LIST OF FIGURES

Figure 5.36 S-3 SAED; (a) Experimental and (b) simulated results for zone axis [001], (c) experimental and (d) simulated results for zone axis [010].

Figure 5.37 XRD patterns of; (a) S-3 XRD simulation using SAED analysis.; (b) S- 2; (c) S-3.

Figure 5.38 S-3 Raman spectra at range 100-1150 cm^{-1} .

Figure 5.39. XRD patterns: S-4 (black), ZnO (violet), $\text{Zn}_3\text{V}_3\text{O}_8$ (green) S- 4 news peaks in * (red).

Figure 5.40 S-4 ESEM-EDX-Map for V, O and Zn.

Figure 5.41 S-4 FIB-SEM; a) Square nanomanipulation using FIB tool (frontal and lateral view) and b) EDX-analysis for the lateral square position (Red frame).

Figure 5.42 S-4 XPS result; a) XPS survey scan and inset; N 1s region (down) and Zn 2p region (up), and b) detailed XPS data of the O 1s and V 2p regions.

Figure 5.43. a) S- 3 (grey) and 4 map surface Raman spectra performed since 100 to 1100 cm^{-1} , inset; square surface micrograph before and after Raman measurement, and b) Raman cross section.

Figure 5.44 S-3 (dark) and 4 (blue) ATR Spectra; a) 4000-2000 range, and b) 2000-450 range, inset; micrograph of the square selected to get ATR spectrum.

Figure 5.45 Representative histogram of S-3 TEM micrographs in different directions.

Figure 5.46 S-4 ($(\text{ZnO})\text{V}_7\text{O}_{16}$) crystallographic model; a) Zn-metalation without presence of interlamellar H_2O , b) with interlamellar H_2O , inset AFM and MF spin interactions.

Figure 5.47. S- 4 and S-2 Magnetic Susceptibility ($1/\chi$).

Figure 5.48. Comparative temperature Hysteresis loops between S-2, S-3 and S-4, at; a) at 4k and b) at 300K.

Figure 5.49. S-4 and 2 Hysteresis loops; a) at 4K, and b) at 300K. Magnetic field in kOe.

Figure 5.50. S-4 VSM results; (a) FC and ZFC and (b) Remanence at 100 kOe.

Figure 6.1 Chapter VI sequence of experiments and characterization; a) T-2 and b) T-3.

Figure 6.2 The framework structure of $\text{H}_2\text{Ti}_3\text{O}_7$ from 47-0561 JCPDS [Feist T. P. 1992].

Figure 6.3 T-1 SEM results at different scale bars; a) 30 μm and b) 1 μm and HRTEM, c) 50 nm and d) 10 nm.

Figure 6.4 XRD of T- 1 (black), $\text{H}_2\text{Ti}_3\text{O}_7$ patterns JCPDS card 47-0561 (grey), TiO_2 anatase (blue) JCPDS card 89-4921, TiO_2 Rutile (green) JCPDS card 89-8304.

Figure 6.5 XRD of T-2 (Violet), w-ZnO (pink) JCPDS Card N° 03-0888, T-1 (black), and $\text{H}_2\text{Ti}_3\text{O}_7$ (grey) from 47-0561 JCPDS [Feist T. P. 1992].

Figure 6.6. T- 2 TEM micrographs a) ZnO NPs between layers, inside and on $\text{H}_2\text{Ti}_3\text{O}_7$ NTs. low magnification, b) ZnO NPs deposition between the layers, c) NTs modified with ZnO NPs and d) ZnO NPs confined on $\text{H}_2\text{Ti}_3\text{O}_7$ lamellas and defects in red arrow.

Figure 6.7. T- 2 IR. a) Region between 4000 and 1000 cm^{-1} , and b) since 1000 to 400 (cm^{-1})

Figure 6.8. T- 2 geometrical model based on; a) histogram analysis of TEM micrographs.

Figure 6.9 XRD of T- 3 (blue), w-ZnO (magenta) ICDD card 361451, Zn_2TiO_4 (green) ICDD 25-1164, ZnTiO_3 (red) ICDD 26-150, $\text{Zn}_2\text{Ti}_3\text{O}_8$ (orange) JCPDS card 87-1781 and T- 1 (black).

Figure 6.10. T- 3 TEM micrographs; ZnO NPs nucleation on and in NTs and between layers with different scale bars (a-d).

Figure 6.11 T- 3 and 1 IR spectroscopy; a) 4000–2000 cm^{-1} , and b) 2000–500 cm^{-1} .

Figure 6.12. T- 3 histogram analysis of TEM micrographs (see figure 6.8b).

Figure 6.13; a) Reflectance diffuse spectra (after Kubelka-Mulk transformation) of T-1, T-2 and T-3 lamellar $\text{H}_2\text{Ti}_3\text{O}_7$ NTs, and (b) plot $(K/S \times hv)^2$ against hv showing the linear fitting to the main linear segment of the curve considering a direct band gap transition.

Figure 6.14 Photodegradation of methylene blue using T-2 and 3.

Figure 6.15 Emission spectra of T-1, T-2 and T-3.

Figure 7.1 ALD window of Mn_xO_y as a function of the number of cycles: thickness vs cycles (black) and growth rate vs cycles (blue).

Figure 7.2. ALD window of Mn_xO_y as a function of temperature: rate vs temperature (black) and growth rate vs cycles (blue).

Figure 7.3 Activation energy (E_a) of Mn_xO_y thin films obtained at 200 cycles at various temperatures (100–200°C).

Figure 7.4. Mn_xO_y XRD, grown at 150°C.

Figure 7.5 (a) AFM-3D topography and (b) EDX analysis of Mn_xO_y thin films.

Figure 7.6. V_xO_y ALD window: thickness vs cycles (black) and GPC vs cycles (blue).

Figure 7.7. V_xO_y ALD window: thickness vs temperature (black) and GPC vs temperature (blue).

Figure 7.8. XRD patterns of (a) $\alpha\text{-V}_2\text{O}_5$ from ALD at 80°C and b) $\alpha\text{-V}_2\text{O}_5$

Figure 7.9. Sn_xO_y ALD window: thickness vs cycles and (black) and growth vs cycles (blue).

Figure 7.10. Sn_xO_y ALD window: thickness vs temperature (black) and growth vs temperature (blue).

Figure 7.11. ESEM of SnO_2 deposition; (a) cross-section and (b) EDX analysis.

Figure 7.12 XRD of a Sn_xO_y thin film

Figure 7.13. ESEM micrograph of a cross-section of a ZnO thin film.

Figure 7.14 AFM of a ZnO thin film.

Figure 7.15 ESEM-cross section micrographs of α -V₂O₅ deposited in AAO dis; a) nanotubes, b and c) defects, and d) homogenous α -V₂O₅ deposition.

Figure 7.16. ESEM-cross section micrographs ZnO deposited in AAO disc; a) homogeneous deposition over all the surface and b) tubes with different ZnO thickness

Figure 7.17 ESEM micrographs of; a) Bare AAO disc and b) AAO deposited with α -V₂O₅.

Figure 7.18 α -V₂O₅ deposition at 80°C in positive photoresist S-1818 pattern at different scale bar; a) 50 μ m and b)100 μ m obtained from optical microscope, and c) 400nm from ESEM cross-section.

Figure 7.19 α -V₂O₅ deposition at 80°C using A-495 PMMA resist like square pattern at different scale bar; a) 1 μ m, b)200 μ m, c) 2 μ m and d) 500 nm.

Figure 7.20 α -V₂O₅ depositions at 80°C on A-495 PMMA resist patterns.

Figure 7.21 α -V₂O₅ MOKE.

Figure 7.22. M_xO_y MOKE.

Figure 7.23 Sequence of experiments and characterization in section 7.2.

Figure 7.24. Schematic energy diagram of a lithium cell at open circuit. Homo and Lumo refer, respectively, to the highest occupied molecular orbital and lowest unoccupied molecular orbital in the electrolyte, reprinted from [Colm O'Dwyer et al. 2015] .

Figure 7.25. Structures and theoretical capacities (C_{th}) of typical aliphatic (a), and aromatic (b) carboxylates. The value of C_{th} was calculated using the formula $C_{th} = nF/3.6M_w$, where n is the number of electrons transferred (n = 2 in compounds 1–5), F is the Faraday constant, and M_w is the molecular weight [Qing Zhao et al 2016, Wang L. et al 2015] .

Figure 7.26 AIO-T ALD window: thickness vs cycles (black) and GPC.

Figure 7.27 AIO-T ALD window: thickness vs temperature (black) and GPC (blue).

Figure 7.28 Determination of the activation energy (E_a) of growing AIO-T thin films, obtained from 50 cycles run at a range of temperatures (150–200°C).

Figure 7.29 AIO-T cross section ESEM-EDX map, including (a) an ESEM micrograph and (b) an EDAX-map of the composition through the interface

Figure 7.30 Cross-section micrograph of an AIO-T thin film showing a view of AIO-T lamellas in a cross-section obtained in FIB-nanolab

Figure 7.31. Cross-section micrographs of AIO-T coated with 50 nm of Cu showing (a) peeling off and (b) a light contrast image of (a).

Figure 7.32 Cross-section EDX analysis of 900 nm of AIO-T coated with 50 nm of Cu.

Figure 7.33 XRD of 900-nm thick AIO-T over a Si-wafer.

Figure 7.34. AFM surface roughness of AIO-T films as a function of substrate cycles.

Figure 7.35. AFM surface roughness of AIO-T films as a function of deposition temperature.

Figure 7.36. AIO-T topography by AFM: (a) 3D topography after growth at 200°C (20.23 nm), and (b) 2D topography.

Figure 7.37 AIO-T models.

Figure 7.38 Correlation of the calculated and experimental IR spectra for AIO-T.

Figure 7.39 Experimental and theoretical UV-Visible spectra.

Figure 7.40 Excitation energy (nm) and HOMO → LUMO contribution and transitions for (a) model 4 and (b) T.

Figure 7.41 (a) Hypothetical energy diagram of electronic transitions. (b) UV-Visible excitation energy with HOMO-LUMO contributions for models 1, (c) 2 and (d) 3.

Figure 7.42. Frontier orbitals (HOMO-LUMO) of Models 1–4, T and TCl.

Figure 7.43. Frontier orbitals (HOMO-LUMO) of model 4, T and solvents such as EC, DEC, DCM and GBL.

Figure 7.44. Hardness of model 4, T and solvents such as H₂O, CH₃OH, CH₃OCH, HCOH and CH₃COH.

Figure 7.45. Softness of model 4, T and solvents such as H₂O, CH₃OH, CH₃OCH, HCOH and CH₃OH.

Figure 7.46. Comparison of the LUMO energies of (a) model 4, (b) T, (c, d) selected salts with carboxylates, (e) oxocarbon, and (f) quinone.

Figure 7.47. Cross section ESEM/EDX mapping of (Li)AIO-T/PF₆/PC: a) qualitative histogram and b) EDAX component distribution through the AIO-T layers.

Figure 7.48 AFM topography of an AIO-T nanomembrane: (a) bare AIO-T (900-nm thick) and (b) AIO-T 900 nm + 4 days of immersion in 1 M LiPF₆/PC.

Figure 7.49 (Li)AIO-T/PF₆-PC IR spectrum (blue) and bare AIO-T (black).

Figure 7.50 ALD window of AIO-A: thickness vs cycles (black) and GPC (blue).

Figure 7.51 (a) TEM micrograph of AIO-A, (b-d) composition through the interface and (e) an overview HAADF-STEM micrograph.

Figure 7.52 STEM of AIO-A: (a, b) EDX-map, and (c) composition throughout the interface.

Figure 9.1. Future projections of the soft nanomaterials here modified and synthesized.

Figure 9.2. Prototype of Integrated Lab-on-Chip & Control Drug Delivery System (CCDS), the system includes; metal oxide semiconductor (MOS) like sensor, a nanobattery and memory nanochip, in addition integrated brain-memory devices with internet signal.

Annex

Figure 1.1. ¹³C-¹H 2D-NMR Spectra of (a) H₆EB(ZnOH)₂ experimental result and (b) extended simulated H₆EB(ZnOH)₂ (model 1).

Figure 1.2. ^{13}C - ^1H 2D-NMR Spectra of the extended simulated $\text{H}_6\text{EB}(\text{ZnOH})_2$ (model 2).

Figure 1.3. ^{13}C - ^1H 2D-NMR Spectra of the extended simulated $\text{H}_6\text{EB}(\text{ZnOH})_2$ (model 1+2).

Figure 1.4. ^{13}C , ^1H Model 1 linear correlation; a) $^1\text{H}_{\text{Experimental}}$ and $^1\text{H}_{\text{Calc}}$ linear correlation ($^1\text{H}_{\text{Experimental}}=0.7386 \ ^1\text{H}_{\text{Calc}} + 0.6531$), and (b) $^{13}\text{C}_{\text{Experimental}}$ and $^{13}\text{C}_{\text{Calc}}$ linear correlation ($^{13}\text{C}_{\text{Experimental}}=0.8384 \ ^{13}\text{C}_{\text{Calc}} + 15.236$).

Figure 1.5. ^{13}C , ^1H Model 2 linear correlation; a) $^1\text{H}_{\text{Experimental}}$ and $^1\text{H}_{\text{Calc}}$ linear correlation ($^1\text{H}_{\text{Experimental}}=0.7822 \ ^1\text{H}_{\text{Calc}} + 1.5418$), and (b) $^{13}\text{C}_{\text{Experimental}}$ and $^{13}\text{C}_{\text{Calc}}$ linear correlation ($^{13}\text{C}_{\text{Experimental}}=0.9132 \ ^{13}\text{C}_{\text{Calc}} + 18.717$).

Figure 1.6. ^{13}C , ^1H Model 1+2 linear correlation; a) $^1\text{H}_{\text{Experimental}}$ and $^1\text{H}_{\text{Calc}}$ linear correlation ($^1\text{H}_{\text{Experimental}}=0.7783 \ ^1\text{H}_{\text{Calc}} + 0.9681$), and (b) $^{13}\text{C}_{\text{Experimental}}$ and $^{13}\text{C}_{\text{Calc}}$ linear correlation ($^{13}\text{C}_{\text{Experimental}}=0.8757 \ ^{13}\text{C}_{\text{Calc}} + 16.743$).

Figure 2.1 S- 2 ESEM micrographs at different scale bars revealing the squares growth.

Figure 2.2 S- 2 HRTEM micrographs at different scale bars; a) 1 μm and b) 0.5 μm and c) SAED analysis.

Figure 2.3 S 2 XPS result; a) XPS survey scan and b) detailed XPS data of the O 1s and V 2p regions.

Figure 2.4 S 2 IR spectra.

Figure 2.5 S 3 ESEM images with different magnification; a) 10 μm , b) 5 μm , c) 5 μm and d) 200nm.

Figure 2.7 shows branches-like arising from the surface, and fringes-like in both edges and corner

Figure 2.7 S- 3 TEM defects images (a,b) Fringe edges-staking faults; (c,d) rolling tubes; (e,f) dislocation.

Figure 2.8 S- 3 XPS result; a) XPS survey scan b) N 1s region and c) detailed XPS data of the O 1s and V 2p regions.

Figure 2.9 S- 4 FIB-SEM-ED micrographs.

Figure 2.10 S- 4 ESEM/EDX results.

Figure 2.11 XRD Linear correlation of $\text{Zn}_3\text{V}_3\text{O}_8$ (a) and ZnO (b) with S- 4.

Figure 3.1 T- 1 EDX.

Figure 3.2 Linear correlation between T- 1 and $\text{H}_2\text{Ti}_3\text{O}_7$ XRD patterns 47-0561 JCPDS.

Figure 3. 3. T- 1 TGA.

Figure 3.4. The framework structure of $\text{D}_2\text{Ti}_3\text{O}_7$ from 47-0561 JCPDS (To replace 41-192)[Feist et al 1992].

Figure 3. 5. T-1 TEM micrographs.

Figure 3. 6. T-2 TEM micrographs; ZnO NPs between $\text{H}_2\text{Ti}_3\text{O}_7$ layers, formation of $(\text{ZnO})\text{Ti}_3\text{O}_7$ layer by layer.

Figure 3.7. T-2 TEM micrographs a) low magnification, b) ZnO NPs deposition between the layers, inside and on $\text{H}_2\text{Ti}_3\text{O}_7$ NTs, showing a widening of the thickness (b,c) and down several regions of (a) with different brightness and contrast.

Figure 3.8. T-2 TEM micrographs showing ZnO NPs deposition between the layers, inside and on $\text{H}_2\text{Ti}_3\text{O}_7$ NTs, showing a widening of the NTs diameter.

Figure 3.9. T-2 TEM micrographs; several regions of figure 3.8, showing ZnO NPs deposition between the layers, inside and on $\text{H}_2\text{Ti}_3\text{O}_7$ NTs, with different brightness and contrast.

Figure 3.10. T-2 micrographs highlight. showing ZnO NPs deposition between the layers, inside and on $\text{H}_2\text{Ti}_3\text{O}_7$ NTs, with different brightness and contrast and size of ZnO NPs, which change since 0.5nm till 2.8nm.

Figure 3. 11. T-2 EDX.

Figure 3. 12. XRD of T-2 (Violet), w-ZnO (magenta) ICDD card 361451, Zn_2TiO_4 (green) ICDD 25-1164, ZnTiO_3 (red) ICDD 26-150, and T- 1 (black).

Figure 3.13. T-3 TEM micrographs; ZnO full nucleation between $\text{H}_2\text{Ti}_3\text{O}_7$ layers, inside and on $\text{H}_2\text{Ti}_3\text{O}_7$ NTs, formation of $(\text{ZnO})\text{Ti}_3\text{O}_7$ NTs/NPs.

Figure 3.14. T- 3 TEM micrographs; ZnO full nucleation between $\text{H}_2\text{Ti}_3\text{O}_7$ layers, inside and on $\text{H}_2\text{Ti}_3\text{O}_7$ NTs, formation of $(\text{ZnO})\text{Ti}_3\text{O}_7$ NTs/NPs.

Figure 3. 15. T- 3 TEM micrographs; ZnO full nucleation between $\text{H}_2\text{Ti}_3\text{O}_7$ layers, inside and on $\text{H}_2\text{Ti}_3\text{O}_7$ NTs, formation of $(\text{ZnO})\text{H}_2\text{Ti}_3\text{O}_7$ NTs/NPs.

Figure 3.16. T-3 TEM micrographs; ZnO full nucleation between $\text{H}_2\text{Ti}_3\text{O}_7$ layers, inside and on $\text{H}_2\text{Ti}_3\text{O}_7$ NTs, formation of $(\text{ZnO})\text{H}_2\text{Ti}_3\text{O}_7$ NTs/NPs.

Figure 3.17. T- 3 EDX.

Figure 3 18.T-2 and T-3 IR spectroscopies in the region between 4000 and 2000 cm^{-1} .

Figure 3.19 XRD of T-3 (blue), w-ZnO (magenta) ICDD card 361451, Zn_2TiO_4 (green) ICDD 25-1164, ZnTiO_3 (red) ICDD 26-150, and T- 1 (black).

ABBREVIATIONS

ALD: Atomic layer deposition.

AC: AdipoylChloride.

AFM: Atomic force Microscopy

CDDS: control drug delivery system.

DOS: Density of State:

DEZn: Diethylzinc

DFT: Density functional theory.

ESEM: Enviromental Scanning Electron Microscopy

EG: Ethylenglicol

EBL: Electron Beam Litography.

EDX: Energy-dispersive X-ray spectroscopy

EBID: Electron beam-induced deposition.

FIB: Focus Ion Beam.

FeH₃EB: FeEnterobactin

H₆EB: Enterobactin

HRTEM: High resolution Transmission Electron Microscopy.

IR: Infrared.

LTI: Leningrad Technological Institute

LOCAD-PTS: Lab-on-Chip Application Development-Portable Test System.

MD: Molecular dynamic.

MOKE: magneto-optic Kerr effect.

MPI: multiple pulsed vapour-phase infiltration.

MALDITOF-MS: matrix-assisted laser desorption/ionization time of the flight mass spectrometry

M_L: Multi layered

M_w: Multiwall.

NMR: Nuclear magnetic resonance.

NPs: Nanoparticles

NTs: Nanotubes

PC: propylencarbonate

SEM: Scanning Electron Microscopy.

SRO: Short Range Order

SAED: Select Area Electron Diffraction

SMO: Semiconductor Metal Oxide.

STEM: Scanning Transmission Electron Microscopy.

TMO: Transition Metal Oxide.

TCL: Therephtaloyl Chloride.

TMA: Trimetyl Alumminium.

TEM: Transmission Electron Microscopy.

VSM: Vibration sample magnetometer.

VPM: vapour phase metalation.

XRR: X-ray reflectivity.

XRD: X-ray diffraction.

XPS: X-ray photoelectron microscopy.

HAADF: High angle annular dark field.

FFT: Fast Fourier Transform.

DSC: Dye-Sensitized Solar Cells.

TMA: trimethyl aluminium (TMA)

VTOP: vanadium triisopropoxide.

Mn(CpEt)₂: bis (ethylcyclopentadienyl) manganese

TDMASn: tetrakis (dimethyl amino) tin.

DEZn: diethylenzinc.

Glycine: Gly

Pro: proline.

Hyp: hydroxyproline.

AVDP: vapour deposition polymerization.

LbL: Layer-by-layer

RT: room temperature.

CVD: Chemical Vapour Deposition.

PVD: Pulsed Vapour Deposition.

MO-ALD: Metal-Oxide Atomic layer deposition
H₂TPP: meso-tetraphenylporphyrin
Zn-TPP: 5,10,15,20-Tetraphenyl-21*H*,23*H*-porphine zinc
MOFs: Metal-organic frameworks.
VTOP: vanadium triisopropoxide.
A.C: Adipoyl Chloride 1,6-hexanediamine
PPTA: poly(*p*-phenylene terephthalamide)
PD: diamine is *p*-phenylenediamine (NH₂C₆H₄NH₂) (PD),
PMDA: 1,2,3,5-benzenetetracarboxylic anhydride)
EDA: ethylenediamine
EG: ethylene glycol.
EA: ethanolamine.
MA: Maleic anhydride.
GPC: growth per cycle.
HQ: hydroquinone.
EXAFS: X-ray absorption fine structure.
VTOP: vanadium tri-isopropoxide.
MALDI is the time of flight (TOF)
HCCA: α-Cyano-4-hydroxycinnamic

GENERAL DEFINITIONS.

Nanotechnology: application of scientific knowledge to manipulate and control matter in the nanoscale in order to make use of size- and structure-dependent properties and phenomena distinct from those associated with individual atoms or molecules or with bulk materials NOTE Manipulate and control includes material synthesis. [DD ISO/TS 80004-1:2010, 2.3]

Nanomaterial: material with any external dimension in the nanoscale or having internal structure or surface structure in the nanoscale.

NOTE 1 This generic term is inclusive of nano-object and nanostructured material.

NOTE 2 See also engineered nanomaterial, manufactured nanomaterial and incidental nanomaterial. [DD ISO/TS 80004-1:2010, 2.4]

Nanostructure: composition of inter-related constituent parts, in which one or more of those parts is a nanoscale region NOTE A region is defined by a boundary representing a discontinuity in properties. [DD ISO/TS 80004-1:2010, 2.6]

Nanostructured material: material having internal nanostructure or surface nanostructure NOTE This definition does not exclude the possibility for a nano-object to have internal structure or surface structure. If external dimension(s) are in the nanoscale, the term nano-object is recommended. [DD ISO/TS 80004-1:2010, 2.7]

Nanocomposite multiphase structure in which at least one of the phases has at least one dimension in the nanoscale [PAS 136:2007, 5.5]

Nanoparticle: Nano-object with all three external dimensions in the nanoscale.

NOTE If the lengths of the longest to the shortest axes of the nano-object differ significantly (typically by more than three times), the terms nanorod or nanoplate are intended to be used instead of the term nanoparticle. [DD CEN ISO/TS 27687:2009, 4.1]

Nanocrystal: nanoscale solid formed with a periodic lattice of atoms, ions or molecules.

Nanotube: hollow nanofibre [DD CEN ISO/TS 27687:2009, 4.4]

Nanophase: discrete phase, within a material, which is in the nanoscale.

Topotactic transition

A transition in which the crystal lattice of the product phase shows one or more crystallographically equivalent, orientational relationships to the crystal lattice of the parent phase. Example: Transitions in which the anionic array is unchanged during the transition but cation reorganization occurs.

Source: PAC, 1994, 66, 577 (*Definitions of terms relating to phase transitions of the solid state (IUPAC Recommendations 1994)*) on page 593.

Functionalization: attachment of chemical functional groups to a surface.

PAS 71:2011

Nano-object material with one, two or three external dimensions in the nanoscale NOTE Generic term for all discrete nanoscale objects. [DD ISO/TS 80004-1:2010, 2.5].

Nanofibre: nano-object with two similar external dimensions in the nanoscale and the third significantly larger

NOTE 1 A nanofibre can be flexible or rigid.

NOTE 2 The two similar external dimensions are considered to differ in size by less than three times and the significantly larger external dimension is considered to differ from the other two by more than three times.

NOTE 3 The larger external dimension is not necessarily in the nanoscale. [DD CEN ISO/TS 27687:2009, 4.3.

Nanoplate: nano-object with one external dimension in the nanoscale and the two other external dimensions significantly larger.

NOTE 1 The smallest external dimension is the thickness of the nanoplate. NOTE 2 The two significantly larger dimensions are considered to differ from the nanoscale dimension by more than three times. NOTE 3 The larger external dimensions are not necessarily in the nanoscale. [DD CEN ISO/TS 27687:2009, 4.2]

Membrane

Structure, having lateral dimensions much greater than its thickness, through which transfer may occur under a variety of driving forces.

Source:

PAC, 1996, 68, 1479 (*Terminology for membranes and membrane processes (IUPAC Recommendations 1996)*) on page 1482

ABSTRACT

The development of new and innovative atomic structures displaying multifunctional properties goes together with progress in advanced processes which enable atomic level control. One leading deposition technique is Atomic layer deposition (ALD), which has emerged as a powerful tool for bond-specific functionalization and the growth of stoichiometric films over wafer scale and high area uniformity. ALD offers a wide range of functionalization routes by means of four processes such as vapour phase metalation (VPM), multiple pulsed vapour-phase infiltration (MPI), ALD and molecular layer deposition (MLD).

As an example of VPM on soft molecules, Zn metalation on Enterobactin (H_6EB) and FeEnterobactin (FeH_3EB) were studied experimentally and theoretically. NMR and IR spectroscopy data were successfully correlated with models of the structures. Docking results between metallized soft molecules and FepA (outer protein) showed an affinity comparable to, and in some cases even higher than, that of their bare counterparts. Thus, we showed that the VPM process could become a route to functionalize soft organic molecules with potential applications in the pharmaceutical field.

Extending VPM growth to hybrid nanostructures, in this case $M_L-(NH_4)V_7O_{16}$ nanostructured squares, enabled studies of their optical and magnetic properties. Samples of $(HDA)V_7O_{16}$ (S-1), $(NH_4)V_7O_{16}$ (S-2), I_2 -functionalized (S-3) and Zn-metallized (S-4) were characterized by state of the art structural techniques (XRD, HRTEM/SAED, FIB, SEM, IR and Raman cross-section microscopy, and XPS). The V_7O_{16} double layer structure was observed, probably for the first time. From SAED HRTEM analysis of $(NH_4)V_7O_{16}$, the triclinic crystal structure and P^{-1} space group was evidenced. The lamellar region of $(NH_4)V_7O_{16}$ was subjected to EDX and Raman scattering cross-section measurements from which we confirmed the presence of Zn in the lamellar region and in the layers, which probably induced the metamorphosis from a triclinic P^{-1} to $Zn_3V_3O_8$ cubic Fd-3m. The observed magnetic behavior of the material is tentatively attributed to a structural metamorphosis from a non-magnetic configuration, passing through the triclinic P^{-1} to a cubic Fd-3m structure, suggesting a transformation from a spin-frustrated semiconductor to a ferromagnet by intercalating ionic species in its interlamellar space. In other words, the Zn metalation-VPM process provides a way to functionalize soft nanostructured materials in order to change their crystal structure and thereby their properties.

Advancing the sophistication of the ALD process, metalation of nanotubes was investigated. Zn metalation by MPI of $M_w\text{-H}_2\text{Ti}_3\text{O}_7$ nanotubes was compared to the VPM process. The structural and optical spectroscopic analysis showed the growth of monocrystals of wurtzite ZnO (w-ZnO) inside and around the $M_L\text{-(NH}_4\text{)V}_7\text{O}_{16}$ square nanostructures, as well as in between the $\text{H}_2\text{Ti}_3\text{O}_7$ nanotube layers. Single layer-by-layer arrangements of ZnO nanoparticles confined between ~ 5 Å thick layered walls of ZnO- $\text{H}_2\text{Ti}_3\text{O}_7$ were clearly observed in material prepared by both processes. The morphological composition of ZnO sheets was found to consist of an arrangement of individual w-ZnO ~ 5 Å nanoparticles. These results show that both Zn-metalation processes allow the successful growth of ZnO nanoparticles inside, between layers and on $\text{H}_2\text{Ti}_3\text{O}_7$ nanotubes due to the presence of internal O-H bonds, exhibiting a preference for structurally-perfect $(\text{ZnO})\text{Ti}_3\text{O}_7$ nanoparticles in nanotubes in single layer-by-layer arrangement, without affecting the general nanotube morphology. Moreover, we found that using DEZn/ H_2O in MPI, promotes the nucleation of ZnO nanoparticles around the nanotube (cactus-like) affecting the morphology and surface properties. The dislocation of some Ti_3O_7 layers together with typical peaks of zinc ortho-titanate (Zn_2TiO_4), suggest a metamorphosis of $\text{H}_2\text{Ti}_3\text{O}_7$ layers to zinc titanate in some regions of the layers. It was found that the electronic energy gap decreases with increasing Zn content, making the $(\text{ZnO})\text{Ti}_3\text{O}_7$ nanoparticle/nanotube nanocomposites potentially useful as photoanode for dye-sensitized solar cells (DSCs) and sensors.

The ALD growth of uniform $M_x\text{O}_y$ thin films where M stands for V, Mn, Sn or Zn was undertaken. The preliminary results show successful deposition of $\alpha\text{-MnO}_2$, $\alpha\text{-V}_2\text{O}_5$, Sn_xO_y and ZnO stoichiometric films, uniform over large areas as characterized by XRR, XRD and AFM measurements. The use of H_2O_2 is better than H_2O for the removal of organic ligand from organometallic precursor when low temperature growth is required. This points towards the possible growth of these oxides which can be considered as energy materials.

Finally, the growth of alucone thin films (AIO-T and AIO-A, T: terephthalate and A: adipate) by ALD and MLD was explored. Stoichiometric thin films with large area uniformity were obtained in both cases, as shown in XRR, XRD and AFM-microscopy data. The use of bifunctional monomers (aromatic and aliphatic carboxylate) in the growth of AIO-T and AIO-A thin films leads to a lamellar phase and to an amorphous one, respectively. The structure of AIO-T is obtained by optimizing four models and correlating experimental data with DFT calculations. The analysis of the electronic band gap using frontier orbital (HOMO-LUMO), of the hardness and softness, alongside the uniform LiPF_6

distribution through the AIO-T, point to future studies of AIO-T for anode and electrolyte nanomembranes with potential applications in carboxylates-based energy storage concepts.

Thus, in this thesis we have shown the versatility of ALD processes to realize novel thin films and pursue various functionalization strategies.

CHAPTER I.

INTRODUCTION

1. Introduction.

Nanotechnology is defined like the application of scientific knowledge to manipulate and control matter in the nanoscale in order to make use of its size- and structure-dependent properties which are different from those associated to the material, either as the discrete atoms or molecules or in the bulk. Nanotechnology currently is emerging as the second major industrial revolution with over 1880 products on the market [Vance, M.E., et al. 2015]. Nanotechnology is currently emerging as the second major industrial revolution, with more than 1880 products on the market [Vance, M. E., et al. 2015]. Nanotechnology is a transformative, rapidly evolving technology that has the potential to greatly improve many areas of human life. This is a new, promising technology for attaining goals including access to novel, clean energy sources, tougher and lighter materials, more effective pharmaceuticals, more nutritious foods, sophisticated safety equipment and revolutionary cancer treatments [Wei, A. 2012].

Thin film deposition is the most popular and useful of the processes used to manufacture high-tech devices like energy conversion and electrochemical storage systems, solar cells, lasers, solid-state lighting, microprocessors, computer memory, and micro or nano electromechanical systems (MEMS or NEMS) [Wang, X., et al. 2015]. The composition, chemical structure, morphology, and thickness of these films directly control their optical, magnetic, and electrical properties, which are often significantly different from those of the bulk [Alivisatos, A. P., 1996].

Atomic layer deposition (ALD) has become one of the most powerful coating tools in the world, being able to produce very thin conformal films with precise control of the thickness, roughness and composition to the atomic level, even at industrial scale. ALD methods appear to be superior to other techniques such as pulsed laser deposition (PLD), chemical vapour deposition (CVD), plasma enhanced chemical vapour deposition (PECVD), sol-gel methodologies, Langmuir-Blodgett thin films, molecular beam epitaxy (MBE) and RF sputter deposition [Wang, X., et al. 2015].

Like CVD, ALD basically consists of the growth of a film by the chemical reaction of typically two gaseous reactants (precursors) on a surface (substrate). However, in this process, the precursors are supplied, one at a time, in a series of sequential non-overlapping pulses by a procedure guaranteeing that no more than one of the precursors is present in the reactor. Thus, each precursor reacts with the substrate in a process that is only limited by the reactive sites available on the surface, leading to a self-limited process [Knez, M., et al. 2011, Knez, M., et al. 2009a]. Therefore, there is a finite

maximum amount of material deposited after one ALD cycle, i.e., when a single exposure of the surface to all the precursors is completed, that is dependent solely on the interaction of the precursors with the surface. Thus, by varying the number of ALD cycles, it is possible to precisely achieve thin films with predetermined thicknesses, independently of the complexity and size of the substrate. A great variety of materials — including metals, organic compounds, hybrid metal organic species, and metal ceramics — may be successfully deposited using suitable precursors [Puurunen, R. L. 2005. George, S.M. 2009a]. The typical precursors used for ceramic coatings are volatile and thermally stable electrophilic metal species, e.g., metal salts, organometallic or metal-organic compounds, while the nonmetal precursors are typically covalent nucleophilic species like water, hydrogen peroxide, or ozone for oxygen; hydrides for chalcogens; ammonia, hydrazine, or amines for nitrogen; or hydrides for group V elements.

The intrinsic versatility of ALD is further enhanced by a series of methodologies derived from the same principles, including Molecular Layer Deposition (MLD) [George, S.M. 2009a], in which at least one of the precursors is an organic molecule; Vapour Phase Metalation (VPM) [Knez, M., et al. 2009b], which exposes the substrate solely to the metal precursor but for longer time periods; and multiple pulsed vapour-phase infiltration (MPI) [Knez, M., et al. 2009a], which uses longer exposures of the substrate to both types of ALD precursors to favour both metal infiltration and the formation of the metal oxide.

In this thesis, we describe a series of studies exploring the versatility of ALD and ALD-based processes to realize thin films of new functional materials. In this context, we have investigated the incorporation of metal species into a select group of systems of different natures and complexities via VPM, MPI, ALD and MLD. Specifically, we studied the growth of uniform M_xO_y thin films, the building of alucone thin films (AIO-T and AIO-A, T: terephthalate and A: adipate) and the functionalization of the soft molecules enterobactin and Fe-enterobactin, hybrid vanadium oxide nanostructures, $(NH_4)V_7O_{16}$ squares, and multi-walled nanotubes of $H_2Ti_3O_7$.

We begin by exploring the spectroscopic and electronic properties of enterobactin (H_6EB) by 1H , ^{13}C and 2D-HSQC nuclear magnetic resonance (NMR), infrared (IR), and UV-Vis spectra to create an IR and NMR standard set (supported by DFT calculations) that helps explain, at a molecular level, the experimental spectra of enterobactin systems, including those from the matrix-assisted laser desorption/ionization time of the flight mass spectrometry (MALDI-TOF MS) of H_6EB and FeH_3EB . Here, two exchange-correlation (xc) functionals (PBE including the long-range corrections –LC-

PBE- and mPW1), two basis sets (QZVP and 6-31G) and two grids (fine and ultrafine) were used for most of the enterobactin structures. Those results are shown in section 5.1.

Zn-metalation by VPM is used to functionalize ferric enterobactin (FeH_3EB) and enterobactin (H_6EB) by linking ZnOH fragments. These samples were characterized by ^1H , ^{13}C and 2D-HSQC nuclear magnetic resonance (NMR), infrared (IR) and UV-Vis spectra to obtain structural information and MALDI TOF-MS spectral analysis to obtain their maximum molecular weights. IR and NMR were correlated with DFT calculations to explain the effect of ZnOH fragments on FeH_3EB and H_6EB structures. We perform studies of FepA missing amino acid residues, molecular dynamics (MD), and molecular docking to minimize the system and calculate the affinity energy between ZnOH-modified siderophores and the FepA outer protein, as covered in section 5.2.

Section 5.3 shows the findings of more complex ALD study: the effect of Zn-metalation by VPM on the functionalization of $\text{M}_L\text{-(NH}_4\text{)V}_7\text{O}_{16}$ nanostructured squares. Samples were characterized by XRD to obtain their crystal structures and interlamellar spacings, which were corroborated by TEM/SAED. The morphology of the samples was explored by TEM and SEM and their qualitative composition by EDX. FIB-nanolab with ESEM-EDX was used to manipulate the square and obtain the Zn distribution throughout the layers. IR and Raman cross-section microscopy were used to determine the functional groups throughout the sample. XPS was used to obtain the valences and qualitative compositions of the samples. Additionally, VSM was performed to explore the magnetic applications of these products.

Growing in ALD complexity, chapter VI describes a study comparing the effect of Zn-metalation by VPM versus that by MPI in the functionalization of $\text{H}_2\text{Ti}_3\text{O}_7$ NTs. The products were characterized by XRD to reveal their crystal structures and the distances of their interlamellar spaces. TEM was used to characterize their morphologies, and IR and UV-Vis spectroscopies were used to identify their functional groups and band gaps (E_g), respectively. Additionally, photocatalytic and luminescent experiments were conducted to understand the effect of such modifications on the photochemical properties of the systems.

Additionally, the ALD growth of uniform M_xO_y thin films (where M stands for V, Mn, Sn or Zn) is undertaken in section 7.1. The preliminary results show the successful deposition of $\alpha\text{-MnO}_2$, $\alpha\text{-V}_2\text{O}_5$, Sn_xO_y and ZnO stoichiometric films uniformly over large areas, as characterized by XRR, XRD

and AFM measurements. Additionally, the magneto-optic Kerr effect (MOKE) is studied to explore the magnetic applications of these synthesized thin films.

Finally, the building of alucone thin films (AIO-T and AIO-A, T: terephthalate and A: adipate) by ALD and MLD are described in section 7.2. The stoichiometric thin films with a large-area uniformity are characterized by XRR, XRD and AFM. The effect of the use of bifunctional monomers (aromatic and aliphatic carboxylates) in the building of AIO-T and AIO-A thin films is explained. The structure of AIO-T is elucidated by optimizing four models and correlating experimental data with DFT calculations. The electronic band gap is analysed using frontier orbitals (HOMO-LUMO), and the hardness and softness of AIO-T nanomembrane are used to explain the uniform distribution of LiPF_6 through AIO-T, whose use as an anode and electrolyte nanomembrane is described.

Hypothesis.

ALD is a powerful tool to obtain the synthesis of hybrid layer by layer organic-inorganic and inorganic-inorganic nanocomposites as well as H-O and H-N specific bond functionalization for example, Zn-metalation of soft molecules and nanostructures.

General aim.

To contribute to the knowledge of ALD and MLD processes by the synthesis and functionalization of hybrid thin films and Zn-metalation (VPM and MPI) processes by the functionalization of Enterobactin (H_6EB), FeEnterobactin (FeH_3EB), $M_L-NH_4V_7O_{16}$, $M_w-H_2Ti_3O_7$ NTs.

Section 5.1. Specifics aims:

- 1) To explore the spectroscopic and electronic properties of H_6EB in order to create an IR and NMR standard set supported by DFT calculations using exchange-correlation (xc) functionals (PBE including long-range corrections –LC-PBE– and mPW1), 2 basis sets (QZVP and 6-31G) and 2 grids (fine and ultrafine) for most of the Enterobactin structures.
- 2) To characterize the MALDI TOF-MS spectra of H_6EB and FeH_3EB .

Section 5.2 Specifics aims:

- 1) To synthesize $H_6EBZnOH$ and $FeH_3EBZnOH$ by Zn-metalation using DEZn.
- 2) To characterize the Malditof-MS spectra of $H_6EBZnOH$ and $FeH_3EBZnOH$.
- 3) To characterize the NMR and IR spectra of $H_6EBZnOH$ and $FeH_3EBZnOH$.
- 4) To correlate the experimental NMR and IR spectra of $FeH_3EBZnOH$.
- 5) To explore the $H_6EBZnOH$ and $FeH_3EBZnOH$ affinity properties with FepA by molecular docking.

Section 5.3 Specifics aims:

- 1) To characterize $M_L-NH_4V_7O_{16}$ nanostructured square by XRD, TEM-ED, FESEM, ESEM-EDX, IR and XPS.
- 2) To characterize I_2 -doped $M_L-NH_4V_7O_{16}$ nanostructured square by XRD, TEM-ED, ESEM-EDX, IR, Raman and XPS.
- 3) To synthesize $(ZnO)V_7O_{16}$ nanostructured square by Zn-metalation using DEZn.
- 4) To characterize Zn- $M_L-NH_4V_7O_{16}$ nanostructured square by XRD, ESEM-EDX, FIB/SEM-EDX, IR, Raman and XPS.
- 5) To explore the magnetic properties of the products by VSM.

Chapter VI. Specific aims.

- 1) To synthesize $(\text{ZnO})\text{Ti}_3\text{O}_7$ NTs by Zn-metalation using DEZn and DEZn/ H_2O .
- 2) To characterize the products by XRD, TEM, IR and UV-vis spectra.
- 3) To explore the band gap of energy “Eg” of the products using diffuse reflectance spectra (Kubelka-Munk).
- 4) To explore the photocatalytic properties of the products.

Section 7.1 Specific aims.

- 1) To synthesize $\alpha\text{-V}_2\text{O}_5$, Mn_xO_y and SnO_2 thin films.
- 2) To determine the ALD-window of $\alpha\text{-V}_2\text{O}_5$, Mn_xO_y and SnO_2 thin films.
- 3) To characterize the thin films obtained in (1) by XRR, XRD, AFM and ESEM-EDX.

Section 7.2 Specific aims.

- 1) To study the effect of the kind of bifunctional monomer (aromatic and aliphatic carboxylate) over the AIO-A and AIO-T thin films structure.
- 2) To synthesize AIO-A and AIO-T thin films using an alternate ALD/MLD processes.
- 3) To determine the ALD-window of AIO-A and AIO-T thin films.
- 4) To characterize the thin films by TEM, SEM-EDX, XRD, XRR, IR and UV-Vis.
- 5) To correlate the IR and UV-Vis of AIO-T thin film by DFT.
- 6) To functionalize AIO-T thin film with LiPF_6/PC and characterize the product by ESEM-EDX-map, AFM and IR microscopy.

Note: The properties here explored have not described in depth, they only have been included in order to provide an extension of the possible applications of the materials here studied.

CHAPTER II.

ALD

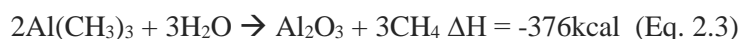
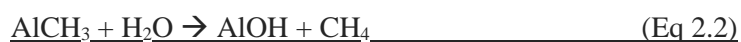
2.1 Historical Background of ALD.

The concept of the ALD process was first developed and published under the name “Molecular Layering” (ML) by V.B. Aleskovskii and S.I. Kol'tsov the LTI in 1952. The ALD as a technology for thin film deposition with encouraging use perspectives at industrial level was developed by Suntola T. et al. [Suntola T., et al. 1977], Finland, in mid-1970s [Puurunen, R.L. 2005]. After starting with element as S_2 (g) and Zn(s) precursors (hence the name ‘atomic’) to obtain ZnS(s), they were forced to consider to molecular precursors like TaCl₅ and H₂O to grow Ta₂O₅, the Zn(Mn)Cl₂ and H₂S to grow Zn(Mn)S, and the AlCl₃/H₂O process to grow Al₂O₃, to expand the materials selection [Puurunen, R.L. 2005]. Thus, ALD was popularly introduced as atomic layer epitaxy (ALE) by Suntola and Antson in 1977, depositing ZnS into an industrial level in the manufacturing of thin film electroluminescent (TFEL) flat-panel displays [Jhonson, R.W., et al 2014]. These displays served as the original motivation for developing the ALD technology as they require high quality dielectric and luminescent films on large-area substrates, something that was not available at the time. TFEL display manufacturing was started in the mid-1980s, being for a long time this the unique industrial application of ALD. Interest in ALD has increased in steps in the mid-1990s and the 2000s, with the interest mainly focused on silicon-based microelectronics [Puurunen, R.L. 2005]. In 2004, the European SEMI award was given to Dr. Suntola for inventing the ALD technology and introducing it worldwide. Another Pioneer of ALD equipment design is Sven Lindfors, his contribution has been in the development of R&D ALD tools since 1975, and likewise Suntola, he allows at directory member of Picosun`s board since 2004. Other popular researchers in ALD field are Roy Gordon from Harvard University, Markku Leskela from Helsinki University of Technology (Finland) and Steven M. George from Colorado University their principal researches activities include thin films and other nanostructured materials made by various chemical methods (Atomic Layer Deposition, electrodeposition and Successive Ionic Layer Adsorption and Reaction) for various applications in micro- and optoelectronics [Puurunen, R.L. 2005]. Their studies include all stages in film growth from precursor synthesis to applications [Van Bui, H., et al. 2017].

2.2 Principle of ALD.

The chemistry involved in the ALD process is similar to that of the CVD, but breaking the CVD reaction into two half-processes separated in the time. Thus, for instance the ALD process for the synthesis of aluminium oxide on a given substrate from the reaction of trimethyl aluminium (TMA, precursor 1) with water (H₂O, precursor 2) can be described by the following chemical equations [Puurunen R. L. 2005], occurring both on the surface of the substrate,

Primary Reactions on the Surface:



These two reactions which occur sequentially on the surface of the substrate, either pristine or modified by the precursor, respectively, by a way that both precursors never are simultaneously present in the reactor chamber. Figure 2.1 illustrates a diagram of a typical ALD cycle used for realizing such a kind of depositions. The classical ALD process essentially considers following steps: 1. The pulse-wise injection of the precursor 1 (e.g., TMA) into the ALD chamber during a given time (the pulse time); 2. The chemisorption of precursor on the active sites on the surface (e.g., Si-wafer), during a period (“exposition time”) long enough for all the available active sites on the substrate surface be loaded, so leading to a monolayer of the first precursor; i.e. a self-termination process, 3. Purge of the excess of precursor 1 and by-products (e.g., CH₄) with an inert gas (Ar or N₂). 4. Pulse injection of the precursor 2 (e.g., H₂O) for generating a monolayer of the final product (e.g., Al₂O₃); 5. Period for the reaction of precursor 2 with the precursor 1 absorbed upon the substrate surface; and finally, 6. Purge with an inert gas to remove the excess of precursor 2 and eventual byproducts. Steps 1-3 constitute a half-cycle. If the thickness of the film formed by one cycle may be determined, the desired thickness of the film can be simply and precisely attained by cycle repetitions [Knez, M., et al. 2009a. Knez, M., et al. 2009b. Knez, M., et al. 2011], [Van Bui, H., et al. 2017], [Puurunen, R.L. 2005].

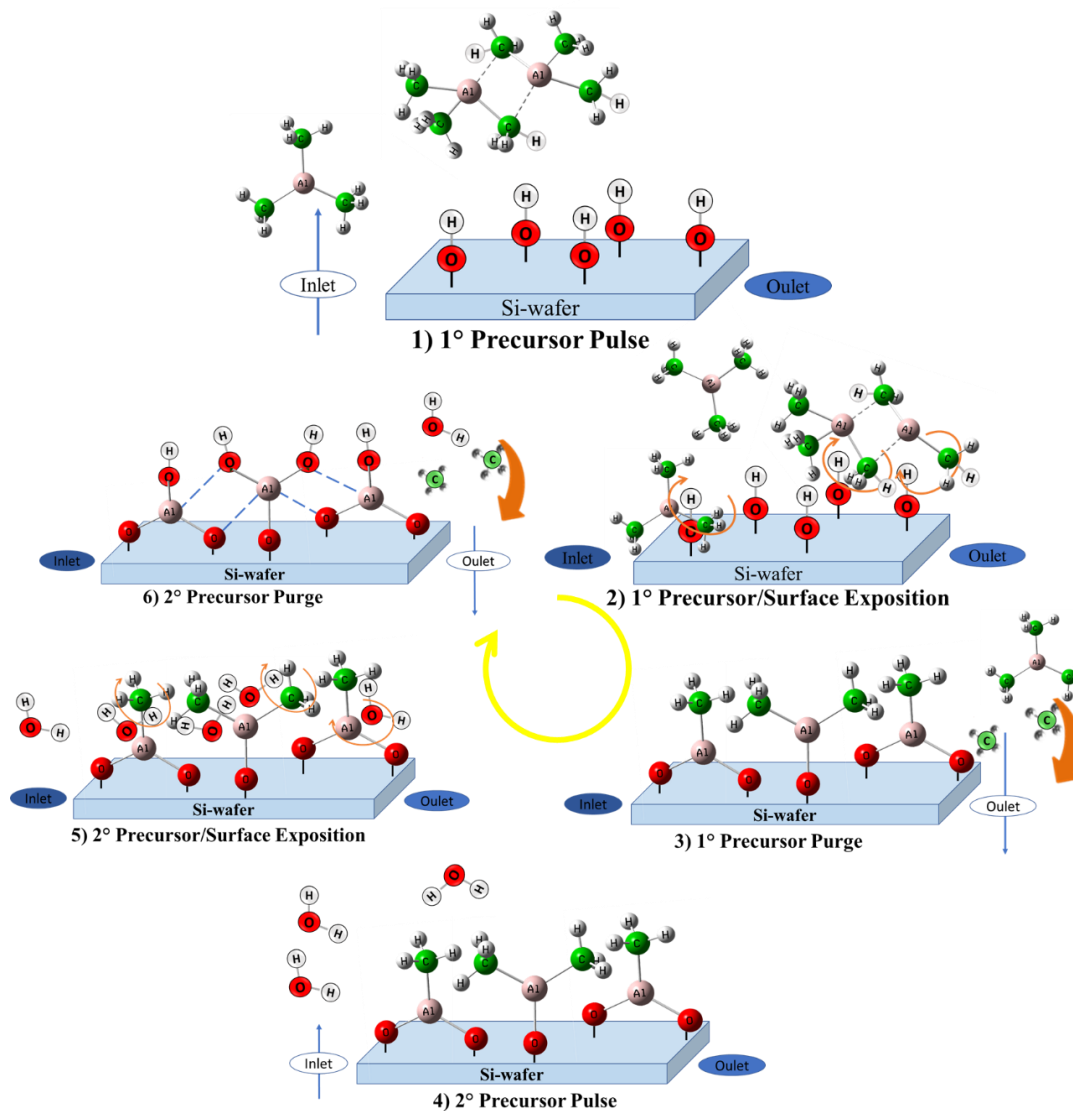


Figure 2.1 Scheme of the synthesis of aluminum oxide by ALD; (1) TMA pulse injection (2) Chemisorption of TMA upon Si-wafer surface (3) Purge of unreacted TMA and byproducts; (4) H₂O pulse-injection and (5) Reaction of water with absorbed TMA; (6) Purge of H₂O excess and byproducts.

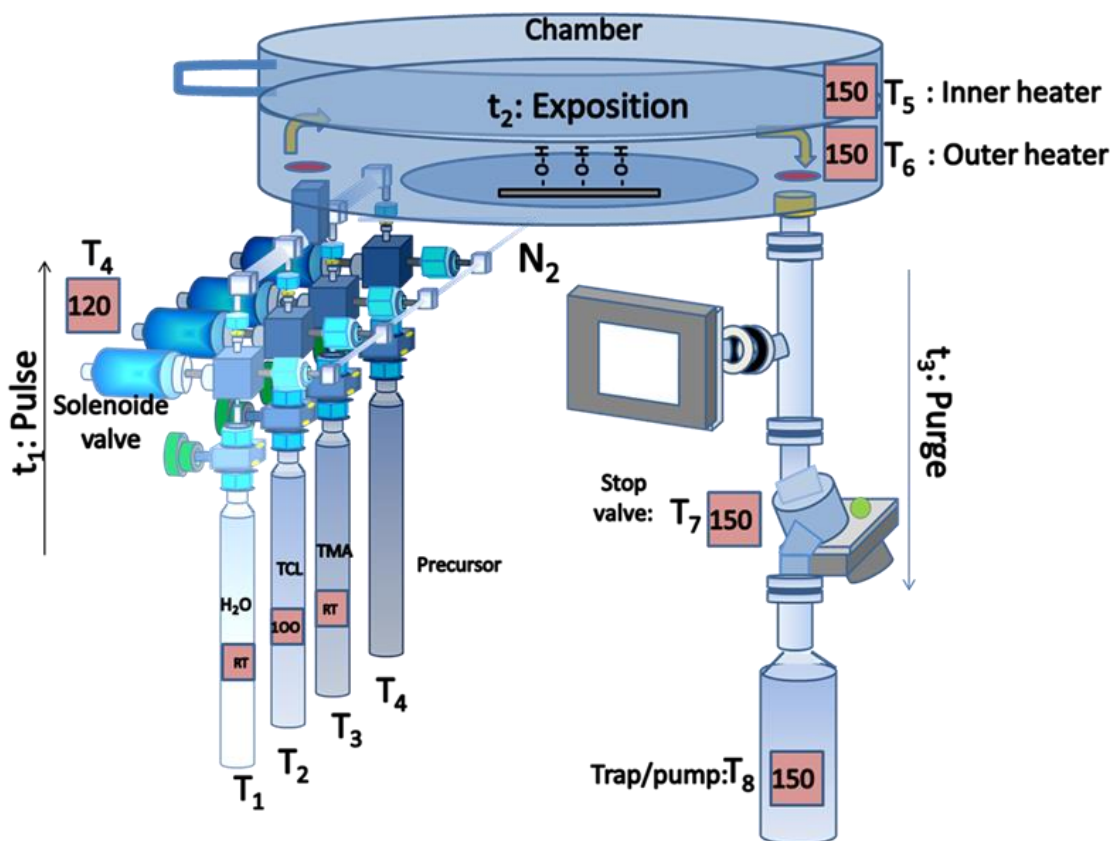


Figure 2.2 ALD reactor.

According to [Puurunen, R.L. 2005], there are five key parameters jointly determining the deposition features; 1) temperature of the substrate, 2) temperature of the precursor, 3) system pressure, 4) pulse, exposition and purge time, 5) activity and reactivity of the precursors involved

Temperature is another crucial factor for achieving ALD characteristics. As discussed, ALD occurs in a self-limiting manner, and therefore it requires the adsorption of precursors to be chemisorbed rather than physisorbed. Consequently, the lowest temperature allowable for ALD should minimize physisorbed ligands. On the other hand, a suitable ALD temperature should not decompose any of the precursors. Otherwise, the deposition will proceed in a CVD manner other than ALD. In contrast to CVD, ALD typically proceeds at much lower temperatures, even down to room temperature (RT) [Puurunen, R.L. 2005]. There are a range of temperatures in which the growth of ALD is almost constant, called the ALD window. In fact, identifying the process window for ALD is important in the optimization of the processing conditions and for understanding the deposition kinetics in detail. Figure 2.3 shows schematically a diagram of typical temperature effects on the ALD process, including the temperature window (W) where the characteristic self-limiting reaction mechanism of this technic and other processes (L and H) take place: Namely, L₁: condensation or exchange reactions

of a reactant; L_2 : self-limited process activation energy; W_1 : full monolayer saturation; W_2 : surface reconstruction during the deposition or steric hindrance between large precursor molecules; H_1 : formation of non-volatile decomposition products from of either reactant or a surface ligand; and H_2 : desorption of a monolayer formed or dissociation of a surface ligand.

Since the ALD growth rate is primarily determined by the surface adsorption of precursors, its dependence on the temperature should be minimal as long as the process is within the ALD regime. Thus, the ALD window is characterized exclusively by a constant growth rate region (W). [Puurunen, R.L. 2005. George, S. M. 2009a].

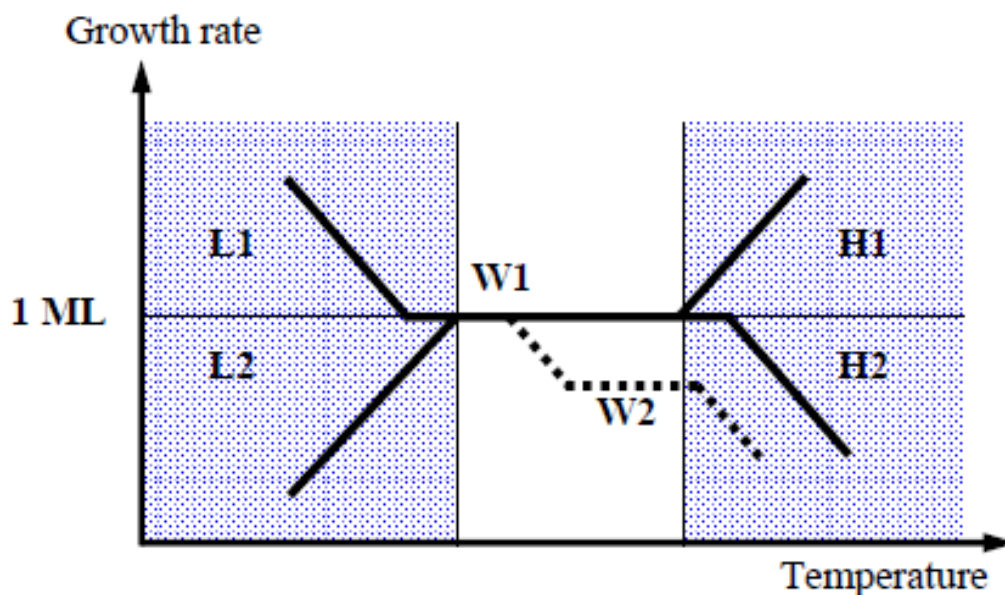


Figure 2.3 Growth rate as a function of temperature for a typical ALD process, ML; monolayer.

ALD process also depends on the protocol design for precursors delivery; the desorption of precursors and insufficient dosing and purging are the key factors in determining thickness uniformity [Puurunen, R.L. 2005] and gas flow. In contrast to the reactants requirements in the CVD processes, the optimal reactants in ALD should react aggressively with each other (low surface-reaction activation energy). That notwithstanding, the reactant in ALD should be stable at the processing temperature in order to avoid undesirable contaminations or incomplete surface reactions.

Precursors volatility and work temperature should be conjugated for getting the vapour amount enough for achieving a continuous monolayer coverage [Puurunen, R.L. 2005]. Initially, the fractional coverage increases linearly with the precursor partial pressure, but then levels off to 100%

once a threshold pressure is exceeded. This threshold must be determined experimentally from deposition rates and film quality. Usually chemisorption occurs on time scales of tens of milliseconds [Puurunen, R.L. 2005]. Incomplete purging of the precursors excess and generated byproducts is also detrimental for attaining continuous processes and accurate controlling the ALD growth per cycle (GPC). Hence, the purging flow rates must be sufficiently high to reduce volatiles in the reaction chamber until to a trace level before proceeding to the injection of a new precursor [Puurunen, R.L. 2005]. Table 2. 1. summarizes some advantages and limitations of a self-limiting film growth.

Table 2. 1. Some advantages and limitations of a self-limiting film growth in ALD [Puurunen R. L. 2005].

Advantages	Limitations
1) Stoichiometric films with large area uniformity and 3D conformality.	1) Limited number of materials that can be deposited, compared to MBE.
2) Precise thickness control.	2) Slower deposition rate than CVD
3) Possible low-temperature depositions	3) Incomplete reaction.
4) Gentle deposition process for sensitive substrates.	4) Slow rate of reaction
5) High control and accuracy of film thickness.	
6) High reproducibility	

2.3 Materials suitable for ALD.

A large range of materials have been deposited using ALD including metals, organic compounds, organic/metallic hybrids and metal ceramics such as oxides, nitrides, selenides, sulphides and tellurides [Puurunen, R.L. 2005. George, S. M. 2009a] (Figure 2.5). To ensure that the precursor properties —reactivity, thermal stability and volatility— are suitable at a given deposition temperature, the ligands surrounding the central atom can be altered. For more detailed information about ALD precursors see the reviews by R. Purunen [Puurunen, R. L. 2005].

Typical metal precursors used in ALD are halides, especially chlorides, alkyl compounds, and alkoxides. Organometallic compounds, such as cyclopentadienyl complexes and alkyl and silyl amides have gained more attention recently [Puurunen, R. L. 2005]. The nonmetal precursors the more frequently used are water, hydrogen peroxide, and ozone for oxygen; hydrides for chalcogens; ammonia, hydrazine, and amines for nitrogen; hydrides for group V elements. [Puurunen, R. L. 2005]

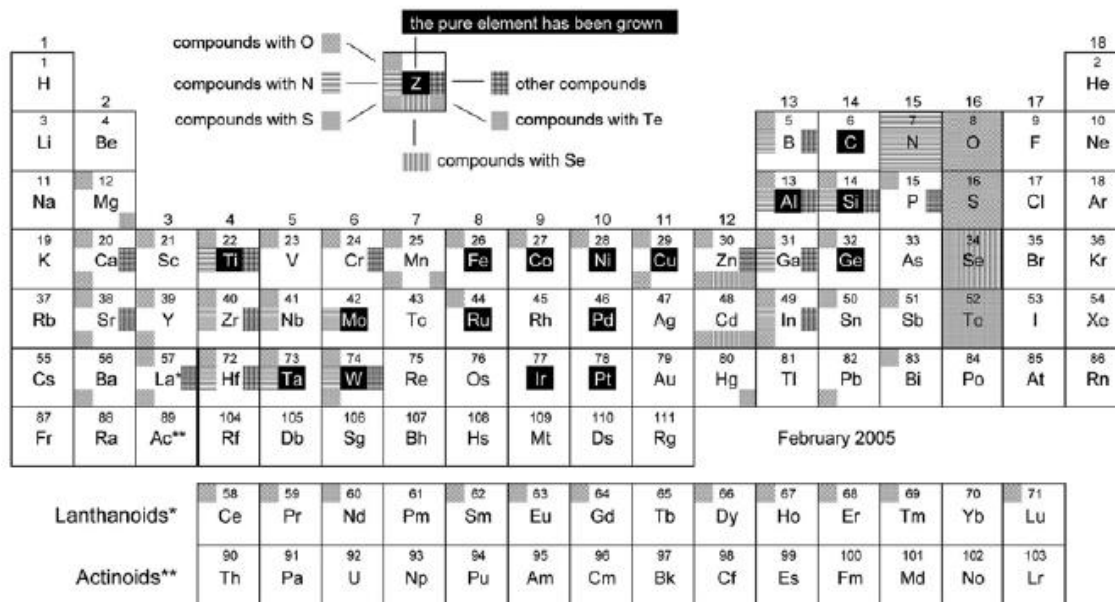


Figure 2.5 Periodic table displaying the different compounds that can be deposited using ALD.

[Puurunen, R. L. 2005].

2.4 Processes performed in an ALD reactor.

Much work has been performed to develop new precursors as well as new processes to increase the versatility of ALD. Much efforts have been invested in researching the interface chemistry associated to the deposition process with the aim to achieve better control over the deposition rate and the area selectivity of the deposition. The magnitude of advances attained in the technology and applications of ALD may be appreciated in a number of reviews recently published [Knez, M., et al. 2011], [Van Bui, H., et al. 2017], [Johnson, R.W., et al. 2014] [Kim, H., et al. 2009], [Karpinen, M., et al. 2014]. Here, we focus on the contribution of Knez, M. et al [Knez, M., et al. 2009a, Knez., M. et al. 2011], [Van Bui, H., et al. 2017], George S.M et al [George, S.M., et al 2009a], R. Purunen [Puurunen, R. L. 2005] and Karpiten, M et al [Karpinen, M. et al 2014].

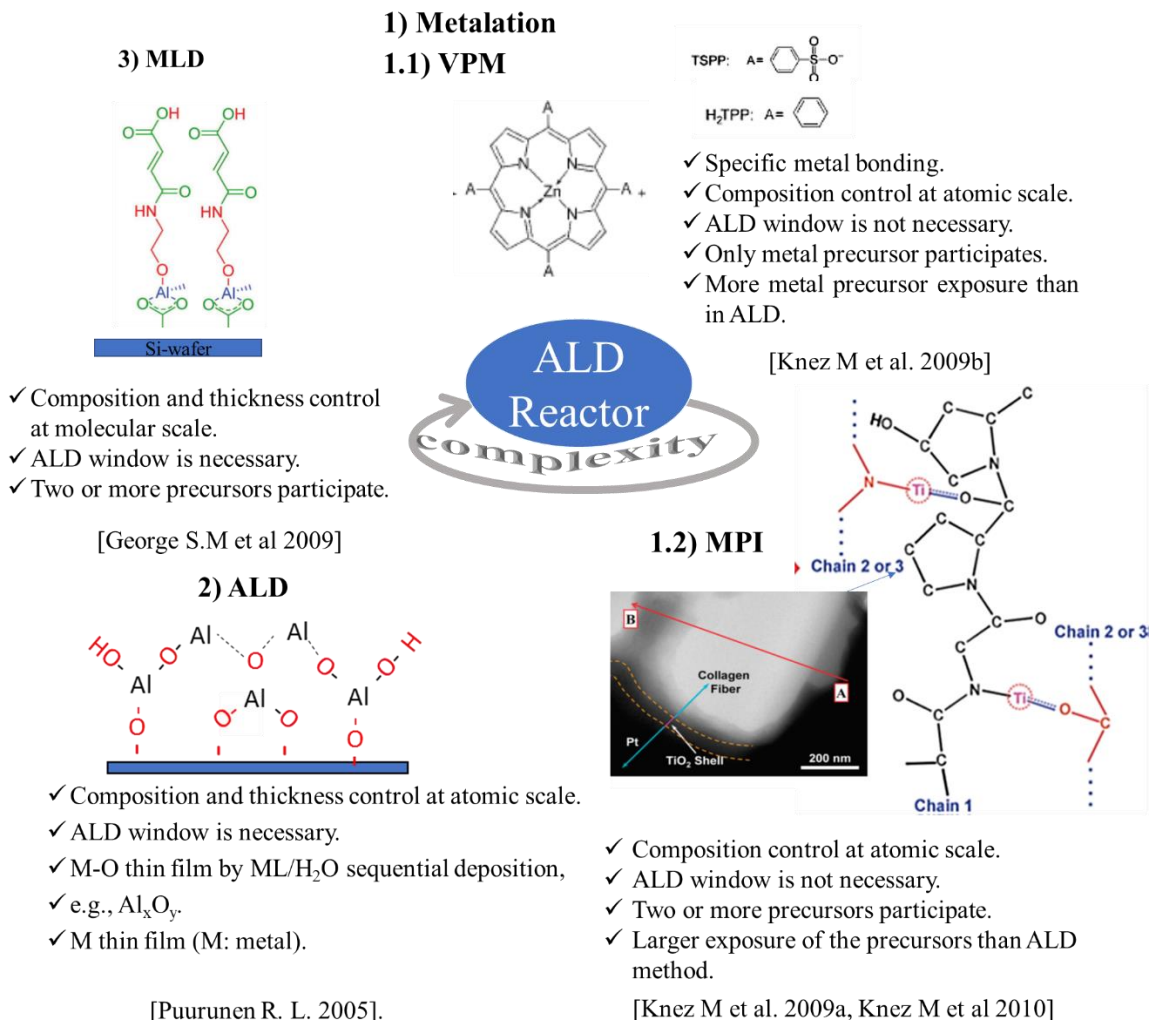


Figure 2.6. Examples of processes performed in an ALD reactor extracted from the references [Knez, M. et al. 2009a. Knez, M. et al. 2009b. Knez, M. et al. 2010. George, S.M., et al 2009a, Puurunen, R.L. 2005].

2.4.1 Metalation processes of soft molecules and nanostructures.

Vapour-phase metalation (VPM) is a half cycle of the standard MO-ALD (M: metal; e.g., ZnO from DEZn/H₂O sequential deposition) and results in the infiltration of the metal precursor into the material. It relies on the same technical principles that ALD, i.e., the sequential supply of vapourized precursors in a solvent free vacuum chamber but restringed only to the chemical reaction of the metal precursor with the substrate surface without the participation of any further precursor (see figure 2.1) Compared with the first half cycle in standar MO-ALD processes, in the VPM technique significantly longer exposure times are used. This in order to allow for diffusion of the metal species into the

material and the chemical modification of the substrate which in the case of organic surfaces often leads to the creation of hybrid organic/inorganic materials [Knez, M., et al. 2015]. A classic example of a VPM is the reaction between diethylzinc and meso-tetraphenylporphyrin (H_2TPP) as substrate reported by Knez M et al [Knez, M., et al. 2009b] (Fig. 2. 6 (1.1)) consisting in an ALD half-cycle performed using 100 pulses of diethylzinc. The pulsing, exposure and purging time were 0.3 s, 60 s and 60 s, respectively, for DEZn, in a 50°C ALD chamber. Purging was conducted with argon at a flow of 20 cm³/min. This procedure leads to the insertion of zinc(II) into the porphyrin cavity through the reaction of DEZn with the N-H group of the H_2TPP , resulting in a Zn-TPP complex and an ethane as byproduct (figure 2.7a). The formation of metalloporphyrins was confirmed by UV/Vis absorption and mass spectrometry.

Another interesting example to comment is the use of vapour-phase metalation in the functionalization of metal–organic frameworks (MOFs) [Mondloch, J.E., et al 2013], a class of hybrid materials comprising inorganic nodes and organic linkers like NU-1000; ($Zr_6(\mu_3-OH)_8(OH)_8-TBAPy)_2$), being H_4TBAPy ; 1,3,6,8-tetrakis(p-benzoicacid) pyrene. Specifically, the metalation of NU-1000 with Zn or Al by the reaction of DEZn or TMA with H-O groups (see figure 2. 7b), leading to the synthesis of Zn-MOFs or Al-MOFs, and ethane or methane as byproduct, respectively. The pulsing, exposure and purging time of 1 s, 120 s, 120 s for DEZn or 0.015 s, 1 s, 1 s for TMA, in a 140° or 110°C, respectively in an ALD chamber. VMP has also been demonstrated to be a successful tool for improving the mechanical properties of natural polymers. In 2015, Knez, M., et al [Knez, M., et al 2015] probed the Zn-metalation or Al-metalation of cellulose to improve its mechanical properties. The mechanical properties, as measured through uniaxial tensile testing, improved as a function of the total number of infiltration cycles and with the precursor used. For cellulose infiltrated with DEZn with only four infiltration cycles, the ultimate tensile strength nearly doubled that of the native cellulose, from ~160 to ~260 MPa. In contrast, cellulose infiltrated with TMA showed very little improvement in mechanical properties. The pulsing, exposure and purging times of 0.05 s, 30 s and 30 s, respectively for DEZn and TMA for 4, 10 and 50 half-cycles in a 100°C ALD chamber. The chemical changes in the cellulose structure were measured with Raman spectroscopy and a novel semi-in situ X-ray photoelectron spectroscopy experiment. The results of both spectroscopic techniques were used to propose the reaction scheme shown in figure 2.7c. The initial cycles of DEZn infiltration lead to dramatic increases in the mechanical properties, most likely due to a cross-linking of the backbone structure with Zn-O bonds.

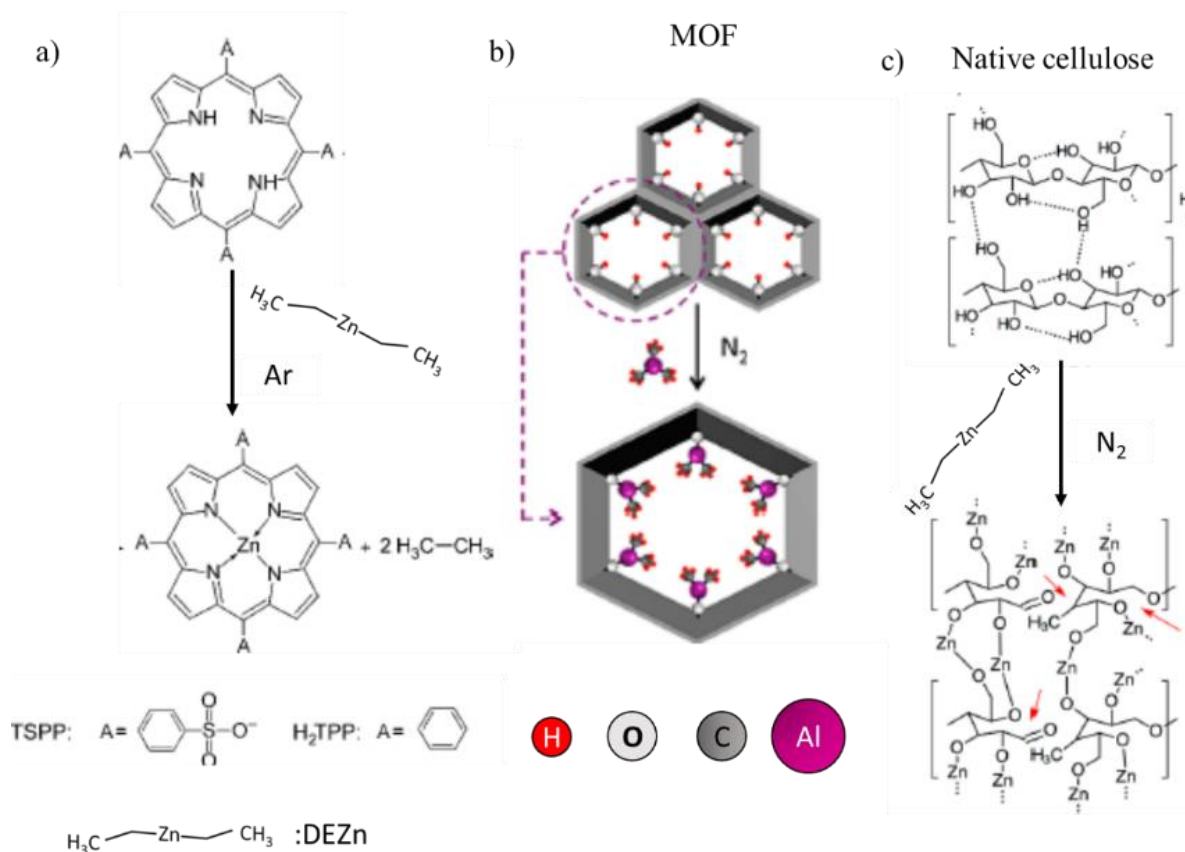


Figure 2.7. Examples of Metalation-VPM process; a) Zn-metalation of H_2TPP [Knez M et al 2009b], b) Al-metalation of MOFs [Mondloch, J.E., et al. 2013] and c) Zn-metalation of cellulose [Knez, M., et al. 2015].

The concept of a multiple pulsed vapour-phase infiltration (MPI) process was introduced by Knez M. in 2009 as a first approach to the VPM process in a study on the metalation of spider-silk and collagen-membranes with Zn, Ti or Al using DEZn/ H_2O , TIP/ H_2O and TMA/ H_2O respectively. Unlike with standard M-O ALD precursors (e.g., DEZn, TMA), in MPI the metal precursor exposure times is relatively longer than in the conventional ALD process, which favours metal infiltration.

Those findings showed the longer exposition times of the metal precursors used in the MPI process afford simultaneously both the M-O layer deposition over the material and the metal infiltration (see figure 2.8). They demonstrated that metals can be intentionally infiltrated into the inner protein structures of biomaterials through MPI performed with equipment conventionally used for ALD and observed greatly improved toughness of the resulting silks and collagen.

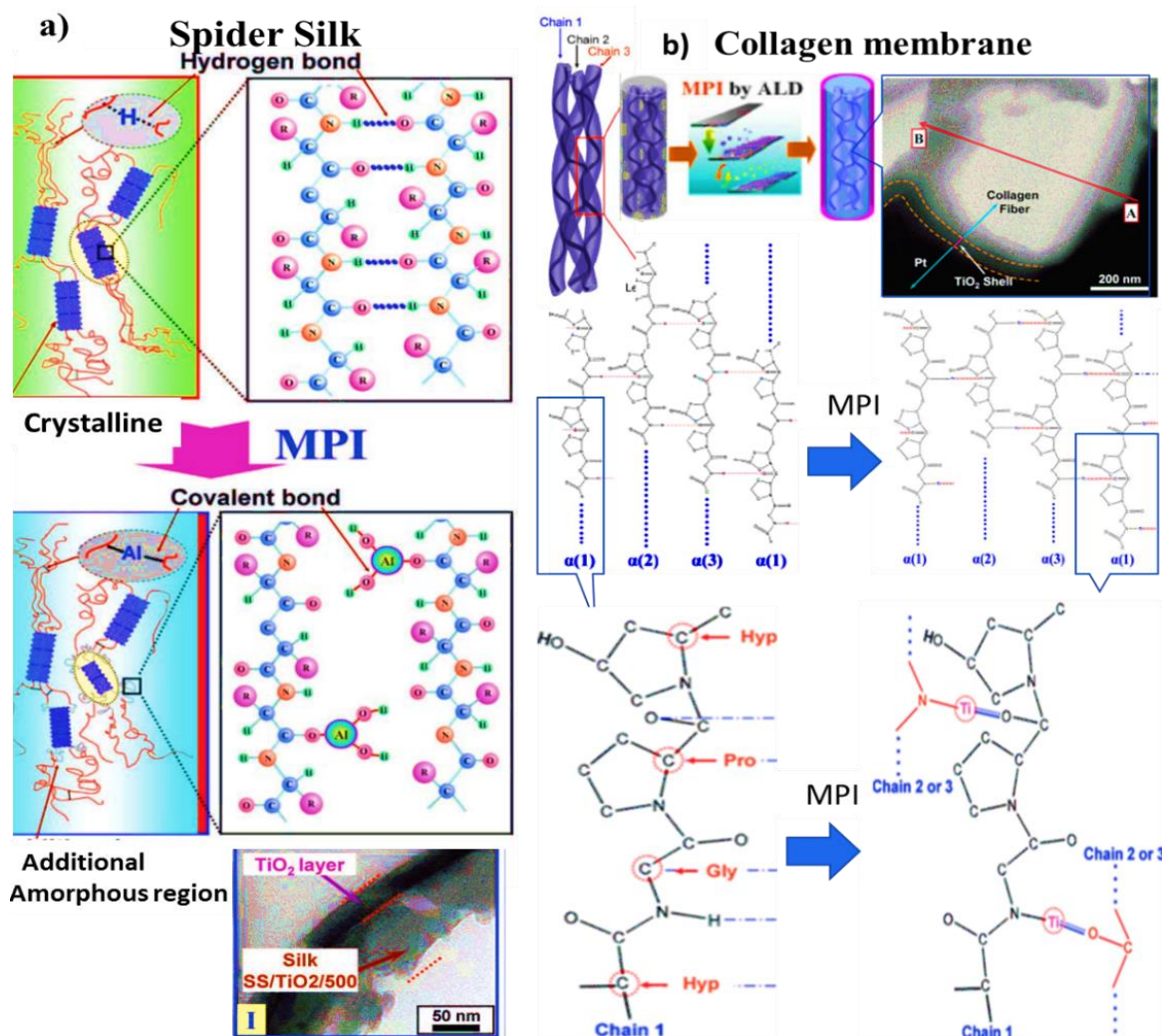


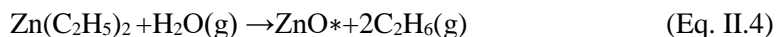
Figure 2.8. Examples of the Metalation-MPI process; a) Al-metalation of spider silk [Knez M. et al 2009a], and b) Ti-metalation of collagen [Knez, M., et al. 2010].

In summary, metal (Ti, Al, or Zn) infiltration into biomaterials via MPI induced crystallographic changes in collagen and spider-silk, likely related to interchain hydrogen bonds, and presumably increased the interfibrillar cross-linking density. This physical/chemical change by metal infiltration has led to the improved mechanical stability of collagen in a dried state. The presence of S-H, N-H and O-H groups in the biomaterials provides reactive sites to link metals such as Zn, Ti and Al from the precursors DEZn, TIP and TMA, respectively.

2.4.2 ALD process.

2.4.2-1 ZnO.

Zinc oxide is a wide band-gap semiconductor with a variety of useful properties that have made it a target of increasing attention in numerous fields of research. By far the most common Zn precursor used in ALD is DEZn which reacts readily with H₂O according to the chemical reaction,

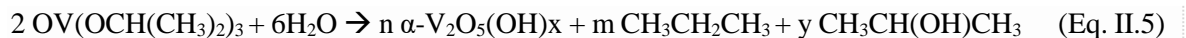


The reaction of DEZn with water is quite exothermic and can be used to deposit ZnO thin films at temperatures much lower than those needed for the ZnAc (Zn acetate)-based processes. Typical deposition temperatures for DEZn-based ZnO deposition processes are in the range of 100–200 °C. However, the DEZn has even been successfully used as precursor at room temperature and at temperatures as high as 600 °C [Tynel, T., et al 2014].

Density functional methods [Munk B. H et al 2006] showed that Zn(C₂H₅)₂ hydrolysis by a single molecule of water has a barrier of 19 kcal/mol, but a second molecule of water lowers this barrier to 4 kcal/mol. Further hydrolysis of Zn(C₂H₅)OH to Zn(OH)₂ is facile. Elimination of C₂H₆ or H₂O to form ZnO is very endothermic. Zn(C₂H₅)OH and Zn(OH)₂ form very stable dimers and tetramers. Elimination of C₂H₆ and H₂O from the dimers and tetramers is also endothermic and leads to ring opening.

2.4.2-2 α-V₂O₅.

ALD processes for α-V₂O₅ are attractive for energy storage nanostructures. Significant research has been done using the sequential deposition of vanadium triisopropoxide (VTOP) and H₂O to yield crystal films associated with α-V₂O₅. Badot et al [Badot J.C et al 2000] report the complete hydrolysis of VTOP (with the appropriate pressure, volume, and temperature) into solid α-V₂O₅(OH)_x and residual products like propane (b.p: -42.°C) and isopropanol (b.p: 80°C), as follows:

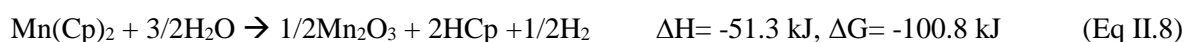
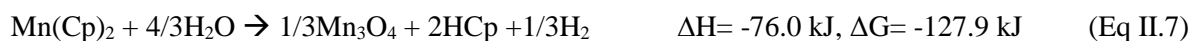
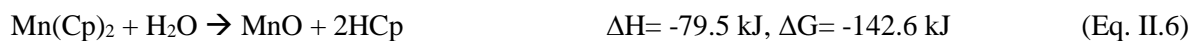


The GPC is similar in both cases (7.7 ng/cm²/cycle), indicating no effect of the length of the purging sequence, which is characteristic of a complete reaction between the precursors.

2.4.2-3 Mn_xO_y.

Manganese oxide can exist in a number of oxidation states, including MnO (Mn(II)), Mn₂O₃ (Mn(III)), and Mn₂O₄ (Mn(IV)). O. Nilsen et al [O. Nilsen et al. 2004] report the deposition of four different phases of MnO₂ — α -MnO (cryptomelane Q), β -MnO₂ (pyrolusite), mixtures of h-MnO₂ and α -MnO₂ and β' -MnO₂ (akhtenskite)— on a variety of substrates like (Si (100), NaCl(100), KCl(100), α -Al₂O₃(001), MgO(100) or KBr(100)) using Mn(thd)₃ (Hthd = 2,2,6,6-tetramethylheptane-3,5-dione) and ozone as precursors. The roughness was measured to be ca. 3.5 and 4.4 nm on the (001) and (012) oriented α -Al₂O₃ substrates, respectively. The GPC measured on Mg(100) was 18.0 pm/cycle (0.018 nm/cycle)

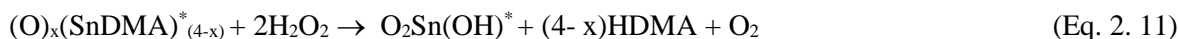
George S. M. et al [George. S. M et al 2009b] have reported thermochemical calculations of manganese oxide predicting MnO deposition using Mn(CpEt)₂ and H₂O as reagents, by means of the enthalpies of reaction (ΔH) and Gibbs free energy (ΔG) at 150 °C.



The results show that Mn(CpEt)₂ reacts successfully with –OH* surface species. The growth per cycle was investigated since 100 to 300°C. The largest MnO ALD growth per cycle was 1.2 Å/cycle at 100°C, and it decreased at higher temperatures. Nevertheless, the MnO deposition by ALD exhibits an incomplete reaction when H₂O is used as the oxygen source. Only 46% of the Mn(CpEt)₂ became MnO. In spite of this, crystallized MnO cubic structure was obtained. MnO in contact with O₂ from the environment easily becomes MnO₂, which is a relevant process for lithium-ion batteries.

2.4.2-4 Sn_xO_y.

Elam J. W. et al [Elam J. W. et al. 2008] describe the deposition of SnO₂ using TDMASn and H₂O₂ like precursors. They observed a high rate deposition of SnO₂ over 10 nm of Al₂O₃ on (001) Si-wafer, at broad range of temperature (50-200 °C). Scanning electron microscopy of the SnO₂ films deposited on Si (100) show that the SnO₂ films are smooth, conformal, and nearly featureless, while atomic force microscopy reports a surface roughness of only 0.84 nm for a film with a thickness of 92 nm.



SnO_2 thin films have been fabricated previously by ALD using the halogenated precursors SnCl_4 [Elam J. W. et al. 2008] and SnI_4 [Elam J. W. et al. 2008]. The disadvantages of these methods include relatively low growth rates, the need for high deposition temperatures, and the inconvenience of using halogenated precursors. Both byproducts, SnCl_4 and the HCl , are corrosive and can damage the deposition equipment. SnO_2 films have also been deposited previously using plasma-assisted ALD. However, this method suffers from the disadvantage that the plasma species are highly reactive and do not allow conformal coatings at very high aspect ratios. For more details of ALD precursors, we recommend Puurunen R. L.'s report [Puurunen R. L. 2005]

2.4.3 MLD process.

MLD is similar to ALD, but in MLD at least one precursor is an organic molecule. In MLD, similar self-limiting surface reactions can be employed for the growth of organic and hybrid polymers. These MLD growth processes have also been known as alternating vapour deposition polymerization (AVDP) and layer-by-layer (LbL) growth. The MLD process is an outgrowth of the earlier gas-phase polymer growth technique known as vapour deposition polymerization (VDP). We recommended the following reviews by Van Bui H. et al. [Van Bui H. et al. 2017], George S. M. et al [George S. M. et al 2009a], R. Purunen [Puurunen R. L. 2005] and Karpiten et al [Karppinen M. et al 2014]. Amplier information on polymer layer deposition may be found many in relatively recent reviews [Van Bui H. et al. 2017], George S.M et al [George S. M. et al 2009a], R. Purunen [Puurunen R. L. 2005] and Karpiten et al [Karppinen M. et al 2014].

2.4.3-1 Polymer MLD

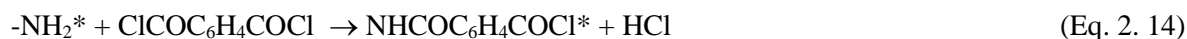
2.4.3-1.1 Organic Polymers.

MLD was initially developed for the growth of organic polymers such as polyamides and polyimides and was reported by [S. M. George et al. 2007, M. Putkonen et al. 2007]. The MLD of various polyamides using acyl chlorides and amines as the reactants has been studied using in situ FTIR spectroscopy. Figure 2.9a depicts a schematic representation of the synthesis of organic polymers using bifunctional monomers. Figure 2.9a shows the synthesis of a polyamide (Nylon-66) [George S. M. et al. 2007] by the reaction between the bifunctional monomers adipoyl chloride ($\text{ClOC}(\text{CH}_2)_4\text{COCl}$) (AC) and 1,6-hexanediamine ($\text{H}_2\text{N}(\text{CH}_2)_6\text{NH}_2$), and figure 2.9b shows the synthesis of poly(*p*-phenylene terephthalamide) (PPTA) [S. M. George et al. 2009a] by the reaction of terephthaloyl chloride ($\text{ClCOC}_6\text{H}_4\text{COCl}$) (TC) and *p*-phenylenediamine ($\text{NH}_2\text{C}_6\text{H}_4\text{NH}_2$) (PD). Both reactions produce HCl as a byproduct. Figure 2.9c depicts the synthesis of polyimide by the sequential reaction of PMDA (1,2,3,5-benzenetetracarboxylic anhydride) and EDA (ethylenediamine), releasing H_2O as byproduct [M. Putkonen et al. 2007].

Synthesis of Nylon 66:



Synthesis of poly(*p*-phenylene terephthalamide) (PPTA)



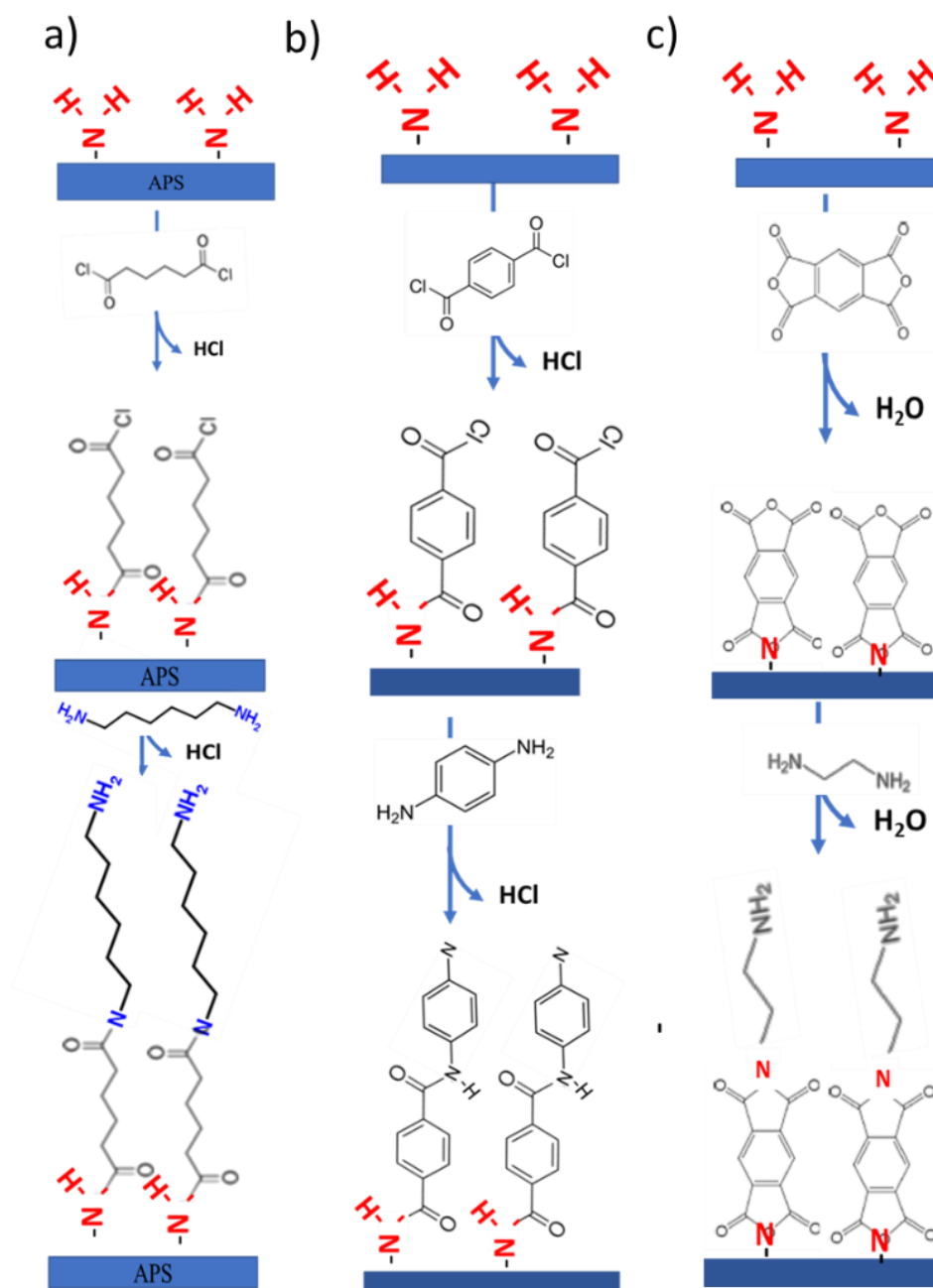


Figure 2.9 Polymer MLD of a) Nylon 66 (polyamide), b) PPTA and c) polyimide.

2.4.3-1.2 Hybrid Polymers; Metalcones.

MLD of Metalcones is also based on sequential, self-limiting surface reactions, but, unlike polymer MLD, the sequential deposition of an “inorganic precursor” (i.e., DEZn, TIP (i.e., Zn, Ti.)) and “molecular fragments” (such as ethylene glycol (EG), ethanolamine (EA), maleic anhydride (MA), glycidol and adipoyl chloride) conducted to obtain hybrid organic-inorganic polymer thin films such as zincone, alucone, titacone and zircone [Karppinen M. et al 2014]. Preparing metalcones by MLD is relatively new; since 2008, S. M. George et al [George S. M. et al. 2008] have explored the synthesis and characterization of several alucones grown using sequential exposures of TMA and EG, EA and MA, and glycidol, as shown in figure 2.10a, to synthesize alucone from TMA and EG [George. S. M. et al 2009a]. Dameron et al [Van Bui H. et al. 2017] report that the GPC is highly dependent on temperature between 0.4 nm per cycle at 85°C and 0.04 nm per cycle at 175°C.

These hybrid polymers result from using alkylaluminium precursors, such as TMA, and various organic diols, such as EG. While most MLD schemes form AB-type polymers (with the sequence A–B–A–B–...), an ABC-type was first proposed by Yoon et al [Van Bui H. et al. 2017]. (figure 2.10b). They used TMA, EA, and MA and obtained a higher GPC than with the AB-type (2.4 nm per cycle at 90°C compared with 0.4 nm per cycle at 170°C). The probable reason is that one of the major problems with AB binary reaction sequences is avoided: the “double” reaction between a homobifunctional reactant and two neighbouring surface species. The higher film growth rate could be caused by localized CVD. ABC-type schemes expand the number of possible organic reactants and provide the opportunity to incorporate particular functionalities into the film. Later, other metalcones such as zincone, titanicone, and zircone were made by MLD [Van Bui H. et al. 2017]. The surface reactions during alucone MLD can be written as depicted in Eq. 2. 16, where the metal alkyl molecule is MR_x and the diol is HOR'OH.



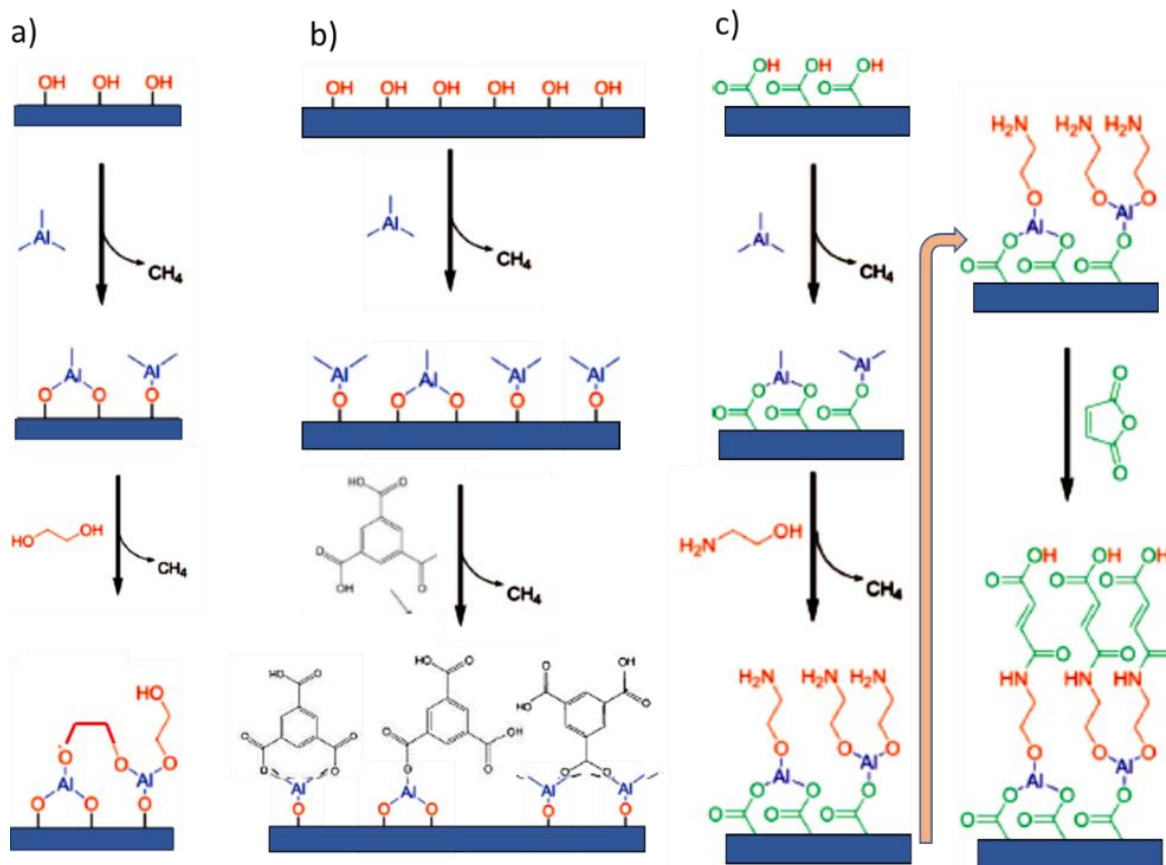


Figure 2.10. Illustration of surface chemistry for; a) two-step alucone MLD using TMA and EG as reactants, b and c) three-step alucone MLD with TMA, EA, and MA as reactants. [George S.M et al 2009a, K. Barnholt-Klepper et al. 2010]

The deposition of organic-inorganic hybrid MLD using TMA and several aromatic carboxylic acids such as; benzoic acid, 1,2-benzene dicarboxylic acid, 1,3-benzene dicarboxylic acid, 1, 1,3,5-benzene tricarboxylic acid, 1,2,4,5-benzene tetracarboxylic acid, were reported by Barnholt-Klepper K. et al. [Barnholt-Klepper K. et al. 2010]. The GPCs of such thin films prepared from TMA are variable, from 0.3nm/cycle to 1.1 nm/cycle at 200 and 300 °C respectively. For 1,3,5-benzene tricarboxylic acid, the roughness varies with the temperature from 0.5 nm at 350°C to 1.35 nm at 250°C (lower temperature). The deposition of 1,4 benzene dicarboxylic acid (Terephthalic acid; TA) was also performed with TMA getting a GPC of ~0.5nm/cycle, and roughness values of 0.25nm at broad range of temperature, since 150 to 350 °C. Aromatic acids are particularly appropriate for in growing such a kind of organic-inorganic hybrid materials since they are relatively easy to work with, stable in air, volatile when heated, thermally stable, and have a stiff backbone structure preventing multiple

reactions with the substrate. It is also very beneficial that the resulting films are relatively stable in air, amorphous and smooth, and they are useful and desirable for the scope of this thesis since they are the counterion of many Lithium salt. Figure 2.10b illustrates the synthesis of alucone MLD from the sequential deposition of 1, 1,3,5-benzene tricarboxylic acid and TMA.

In 2013, S.M. George et al [George S.M et al. 2013] discussed the synthesis of a lamellar arrangement of ZnO via ALD-MLD using the sequential deposition of DEZn-HQ-DEZn-H₂O-DEZn-H₂O (where HQ is hydroquinone). Three sets (figure 2.11) of hybrid organic-inorganic zincone thin films were prepared based on zinc precursors and organic diols on (100) Si wafers. A 1 nm alumina layer was deposited first by ALD at 150°C as the adhesion layer that promotes the initial ALD/MLD growth. DEZn can react with aliphatic organic diols such as ethylene glycol (EG) or aromatic organic diols such as hydroquinone (HQ) to form type A or type B MLD zincone films, respectively.

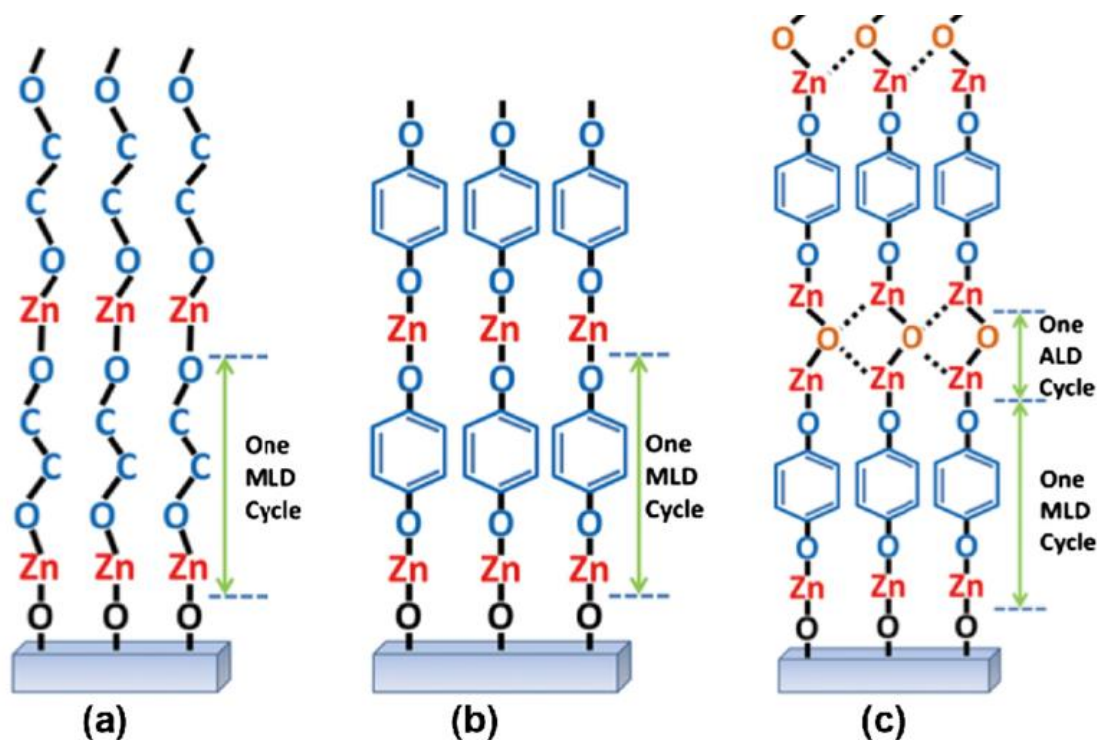


Figure 2.11. (a) Schematic drawing of the MLD cycles for preparing zincone film using DEZn and EG and (b) DEZn and HQ. (c) ALD-MLD of a zincone film deposited using DEZn/H₂O and DEZn/HQ in sequence [George S.M et al 2013].

Figures 2.11 a and b show the schematic drawing of type A and type B MLD zincone films, which are fabricated by the sequential deposition of DEZn/EG (1:1) and DEZn/HQ (1:1), respectively, in sequence. ZnO can be deposited using ALD with DEZn and H₂O as the reactants. By alternating ZnO ALD and zincone MLD, a type C ALD–MLD zincone film is fabricated with DEZn/H₂O (1:1) and DEZn/HQ (1:1), as shown in Figure 2.11c. XRD results show a crystalline phase for the type C MLD and an amorphous phase for types A and B. Therefore, **distinct phases** can arise from ALD-MLD processes.

CHAPTER III

THEORETICAL AND EXPERIMENTAL

METHODS

3.1.1 Essential aspects of DFT.

3.1.2-1 Calculation with density functional.

Density functional theory (DFT) is one of the most frequently used computational methodology in physics, chemistry and materials science to study the electronic structure of many-body systems. DFT determine the properties of such systems by using functional (functions of a function) that are dependent of the electron density.

DFT is based on the Hohenberg–Kohn theorems [Hohenberg, P. and Kohn, W. 1964] which shows that the ground state properties of a many-electron systems are uniquely determined by an electron density that depends on its spatial coordinates and this is calculated through the use of functionals. According to this, the energy functional of a system minimizes to its ground state. We use the Kohn–Sham DFT framework [Kohn and L.J. Sham.1965] to solve the Schrodinger equation of non-interacting particles with a density identical to the system with interacting particles. The non-interacting system moves in a local external potential (V_{xc}) which wavefunction is a single Slater determinant created from a set of Kohn-Sham orbitals that provide the lowest energy solution. Exc is the exact-exchange energy.

$$\sum_{s=1}^b C_{si} (h_{rs}^{ks} - \varepsilon_i^{ks} S_{rs}) = 0, \text{ with } r = 1, 2 \dots \text{ (Eq. 3.1) [Levine, I.N. 2004]}$$

These orbitals are used to achieve electron density. The calculation continues until there is not a difference in the density and the orbital ks , the interactions finish when the calculation converges. When both ρ and approximate functional E_{xc} are known, the energy can be calculated. This allows to calculate the properties of a system, e.g., molecules.

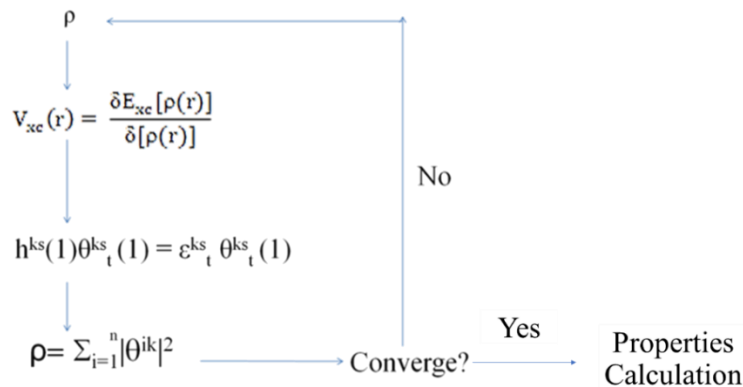


Figure 3.1 Diagram of DFT method.

DFT would lead to the obtaining approximate ground state energy and electron density if the exact exchange-correlation functional is known. In practice, this function is unknown and therefore one uses approximated functionals. The table 1.1 summarize the Ab-initio xc-functionals and their basis set performed in section 5.1.

Table 1.1. Summary of Ab-initio methods.

Short name	xc functional	Basis-set
PBE-1	LC-PBE	QZVP
mPW91-1a	mPW91	QZVP
mPW91-1b	mPW91	6-31G(d)
mPW91-1b1	mPW91	6-31G(d)
PBE-2	LC-PBE	QZVP
mPW91-2a	mPW91	QZVP
mPW91-2b	mPW91	6-31G(d)
mPW91-2b1	mPW91	6-31G(d)
PBE-3	LC-PBE	QZVP
PBE-4	LC-PBE	QZVP
PBE-5	LC-PBE	QZVP

3.1.2-2 Electronic chemical potential, μ , Hardness and Softness.

The electronic chemical potential, μ (Eq. 3.2) is defined as the sum of the potential ionization “I” (Eq. 3.3) and the electron affinity “A” of an atom [Mendizabal, F., et al 2011],

$$\mu = \left(\frac{\partial E}{\partial N} \right)_V \quad (\text{Eq. 3.2})$$

$$\mu \approx -\frac{1}{2} (I + A) \approx \frac{1}{2} (\varepsilon_L + \varepsilon_H) \quad (\text{Eq. 3.3})$$

Where ε_L and ε_H are the energies of molecular orbitals (HOMO and LUMO) highest occupied and lowest unoccupied respectively.

Hardness and Softness.

There are two principles of chemical reactivity associated to the hardness: the principle HSAB (hard soft - acid base) [Pearson, R.P. 1963] and the principle of maximum or global hardness [Pearson, R.P.

1993]. In many numerical applications “ η ” is calculated considering the ionization potential “ I ” and electron affinity “ A ” (eq. 3.7) [Mendizabal, F. et al 2011],

$$\eta \approx \frac{1}{2} (I - A) \approx \frac{1}{2} (\varepsilon_L - \varepsilon_H) \quad (\text{Eq. 3.4})$$

Where ε_L and ε_H are the energies of molecular orbitals (HOMO and LUMO) highest occupied and lowest unoccupied respectively. General Hardness and Softness [Torrent-Sucarrat, M. et al 2010] is an important chemical concept that allow understand, for instance the distribution and coordination of Li^+ in local groups such as: ester, ether, carboxylic acid, amides and alcohols inside of specific donor molecules arrangement. In this sense DFT allows describe the reactivity and activity of any acid-base reaction by local and global hardness and softness. The global hardness “ η ” given as the second derivate of the energy “ E ” with respect to the number of electrons “ N ” at constant external potential “ $v(\vec{r})$ ” captures the resistance of chemical species to changing its electronic number [Parr R. G. et al 1985].

$$\eta = S^{-1} = \left(\frac{\partial^2 E}{\partial N^2} \right)_{v(\vec{r})} = \left(\frac{\partial \mu}{\partial N} \right)_{v(\vec{r})} \quad (\text{Eq. 3.5})$$

Here S and μ denote the global softness and chemical potential, respectively. These indices are called global descriptors because they describe the properties of a molecule and their finite difference approximation leads to the two most popular operational equations of the global hardness and softness like show the Eq. 3.5

3.1.3 Nucleophilicity and Electrophilicity index.

Parr et al. [Yang, W. & Parr, R.G. 1985, Mendizabal et al 2011] defined the electrophilicity index “ ω ” as follows:

$$\omega = \mu^2/2\eta \quad (\text{Eq. 3.6})$$

where η is the chemical hardness of the system. Then the nucleophilicity index “ ω ” can be defined by:

$$\omega^{\cdot} = -I \approx \varepsilon_H \quad (\text{Eq. 3.7})$$

Where, I is the first vertical ionization potential, and ε_H is the one electron energy of the HOMO orbital.

Note: In this thesis, like preliminary results we use the equations 3.4, 3.5, 3.6, 3.8 and 3.9 to predict AIO-T properties in section 7.2.

3.2 Experimental Methods.

3.2.1 MALDI-TOF.

Matrix-assisted laser desorption-ionization (MALDI) spectrometry is an ionization method that can be used to obtain accurate molecular mass information about polar biopolymers ranging in molecular mass from a few thousand to several hundred thousand Da. In the MALDI technique, a low concentration of the analyte is uniformly dispersed in a solid or liquid matrix deposited on the end of a stainless-steel probe or placed on a metal plate. The plate is then placed in a vacuum chamber and a laser beam is focused onto the sample. The MALDI matrix must strongly absorb the laser radiation. The matrix and analyte are then desorbed and ionized, creating an ion plume. The most common type of mass analyzer used with MALDI is the time of flight (TOF) analyzer. A mass spectrum from a MALDI-TOF instrument is shown in figure 3.2.

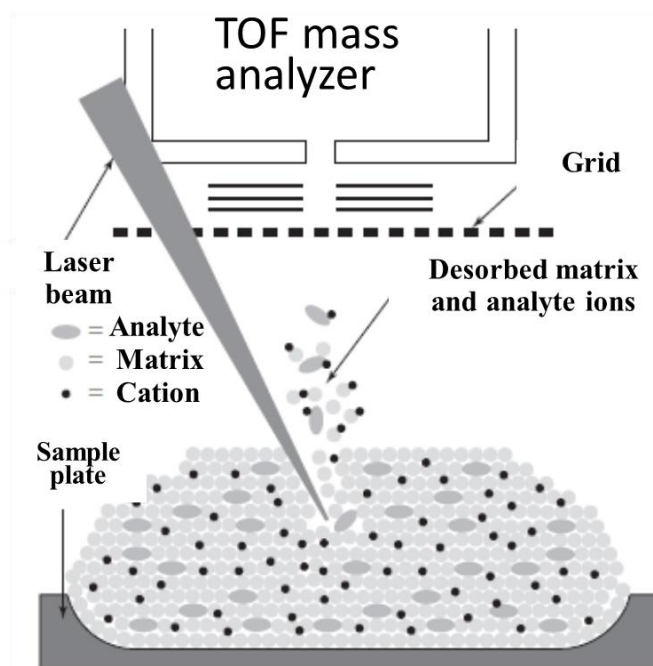


Figure 3.2. Diagram of the MALDI process. The analyte is uniformly dispersed in a matrix and placed on a metal sample plate. A pulsed laser beam strikes the sample causing desorption of a plume of matrix, analyte, and other ions. The analyte can be protonated, be deprotonated, or form adducts before entering the TOF analyser.

MALDI is referred to as a “soft” ionization technique, because the spectrum shows mostly intact, singly charged ions for the analyte molecules. However, sometimes and in some cases, MALDI causes minimal fragmentation so it is not as “soft” as ESI-MS (electrospray ionization mass spectrometry), depending on the characteristics of analytes and the conditions of laser used. Multiply charged ions are present as well as peaks for dimer and trimer species. The mechanism of the formation of the MALDI ion plume is not completely understood. However, it is thought to involve absorption of the laser beam by the matrix, followed by transfer of the energy from the matrix to the analyte. Desorption of the analyte and the matrix then occurs. The analyte is thought to desorb as neutral molecules and then to be ionized by proton-transfer reactions with protonated matrix ions in a dense phase over the surface containing the matrix. A series of photochemical reactions may produce the protonated matrix ions. In Table 3.1 are listed some materials used as matrix for biomolecules, along with the lasers and the wavelengths that have been employed. Lasers used include nitrogen (337 nm). Nd-YAG (266 and 355 nm), excimer (308 nm). Er- YAG (2.94 μm). and CO_2 (10.6 μm).

The most common sample-preparation method is the dried-droplet technique in which a droplet of the matrix containing the analyte is deposited on the metal plate and then dried. Typically, the ratio analyte to matrix is $1:10^3$ to $1:10^5$. Analyte concentrations are usually in the micromolar range [Skoog, D. A., et al.2007].

Table 3.1 Common matrices and stable for MALDI and usable Wavelengths.

Matrix	Wavelength, nm
2,5-Dihydroxybenzoicacid	266, 337, 355, 2940
2-(4-Hydroxyphenylazo) benzoic acid	266.377
a-Cyano-4-hydroxycinnamic acid (HCCA)	337

In this thesis HCCA matrix is used to obtain characterized Enterobactin, FeEnterobactin and their Zn-products; EnterobactinZnOH and FeEnterobactinZnOH.

3.2.2 Nuclear Magnetic Resonance (NMR).

NMR is an analytical chemistry technique that exploits the magnetic properties of certain atomic nuclei which allow elucidate the molecular structure where they are store. This type of spectroscopy determines the physical and chemical properties of atoms or the molecules in which they are contained [Baldwin, I.E., et al 1999]. Most NMR investigations will begin with the analysis of the proton spectrum of the sample of interest, with the usual analysis of the chemical shifts, coupling constants and relative signal intensities, either manually or with the assistance of the various sophisticated computer-based structure-spectrum data bases now available. Although there exist a huge number of pulse sequences, there are a relatively small number of what might be called core experiments, from which most others are derived by minor variations, of which only a rather small fraction ever find widespread use in the research laboratory.

To begin, it is perhaps instructive to realise that virtually all NMR methods exploit only three basic phenomena:

- Through-bond interactions: scalar (J) coupling via bonding electrons.

Through-space interactions: the nuclear Overhauser effect mediated through dipole coupling and spin relaxation.

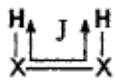

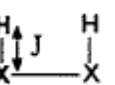
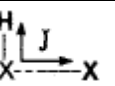
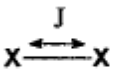
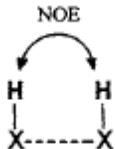
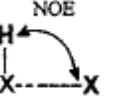

- Chemical exchange: the physical exchange of one spin for another at a specific location.

To analyse the structure of a molecule and/or its behaviour in solution by NMR spectroscopy, one must therefore consider how to exploit these phenomena to gain the desired information, and then select the appropriate technique(s).

To build up the structure of a molecule one typically first searches for evidence of scalar coupling between nuclei as this can be used to indicate the location of chemical bonds. When the location of all bonding relationships within the molecule have been established, the gross structure of the molecule is defined. Spatial proximities between nuclei, and between protons in particular, can be used to define stereochemical relationships within a molecule and thus address questions of configuration and conformation. The unique feature of NMR spectroscopy, and the principal reason for its superiority over any other solution-state technique for structure elucidation, is its ability to define relationships between *specific nuclei* within a molecule or even between molecules. Such detail is generally obtained by correlating one nucleus with another by exploiting the above phenomena. Despite the enormous power of NMR, there are, in fact, rather few types of correlation available to the chemist to employ for structural and conformational analysis. The principal spin interactions and

the main techniques used to map these, which are frequently two-dimensional methods, are summarised in Table 3.2.

Table 3.2. The principal correlations established through NMR techniques.

Correlation	Principal Technique	comments
	^1H - ^1H COSY	Proton J-coupling typically over 2 or 3 bonds.
	^1H - ^1H TOCSY	Relayed proton J-couplings within a coupled spin system. Remote protons may be correlated provided there is a continuous coupling network in between them.
	^1H -X HMC ^1H -X HSQC	One-bond heteronuclear couplings with proton observation
	^1H -X-HMBC	Long-range heteronuclear couplings with proton observation. Typically, over 2 or 3 bonds when X = ^{13}C .
	X-X COSY X-X Inadequate	COSY only used when X-spin natural abundance > 20%. Sensitivity problems when X has low natural abundance
	^1H - ^1H NOE difference 1/2D NOESY 1/2D ROESY	Through-space correlations. NOE difference only applicable to 'mid-sized' molecules with masses ca. 1-2 kDa.
	^1H -X NOE difference 2D HOESY	Sensitivity limited by X-spin observation. Care required to make NOEs specific in presence of proton decoupling.
	1D saturation or inversion transfer 2D EXSY	Interchange of spins at chemically distinct locations. Exchange must be slow on NMR timescale for separate resonances to be observed. Intermediate to fast exchange requires lineshape analysis

The correlated spins are shown in bold type for each correlation, with X indicating any spin-1/2 nucleus. The acronyms are explained in the glossary.

The homonuclear correlation experiment, COSY, identifies those nuclei that share a J-coupling, which, for protons, operate over two, three, and, less frequently, four bonds. This information can therefore be used to indicate the presence of a bonding pathway. The correlation of protons that exist within the same coupled network or chain of spins, but do not themselves share a J-coupling, can be made with the TOCSY experiment. This can be used to identify groups of nuclei that sit within the same isolated spin system, such as the amino acid residue of a peptide or the sugar ring of an oligosaccharide.

One-bond heteronuclear correlation methods (HMQC or HSQC) identify the heteroatoms to which the protons are directly attached and can, for example, provide carbon assignments from previously established proton assignments. Proton chemical shifts can also be dispersed according to the shift of the attached heteroatom, so aiding the assignment of the proton spectrum itself. Long-range heteronuclear correlations over typically two- or three-bonds (HMBC) provide a wealth of information on the skeleton of the molecule and can be used to infer the location of carbon-carbon or carbon-heteroatom bonds. These correlations can be particularly valuable when proton-proton correlations are absent. The inadequate experiment identifies connectivity between like nuclei of low-natural abundance, for which it is favoured over COSY. This can therefore correlate directly-connected carbon centres, but as this relies on the presence of neighbouring carbon-13 nuclei it suffers from appallingly low sensitivity and thus finds little use. Modern variants that use proton detection have greatly improved performance but are still likely to be less used than the heteronuclear correlation techniques.

3.2.3 Infrared and Raman Spectroscopy Fundamentals.

Molecular spectra result from the periodic motions (or vibrational modes) of atomic nuclei within their respective molecules. These nuclei move together or apart along a straight-line vector so they are rotating, vibrating, wagging and bending respect to their gravity centres rotate; they vibrate; they wag; and they bend relative to their centres of gravity. The vibration and ending of molecules exhibit vibrational spectroscopic activity that may be measured using any number of spectroscopic techniques, including infrared spectroscopy in different frequency ranges and Raman scattering. [Workman, J. L. 2007. pp 1].

3.2.4 Theory of Raman spectroscopy.

Raman spectra are acquired by irradiating a sample with a powerful laser source of visible or near-IR monochromatic radiation. During irradiation, the spectrum of the scattered radiation is measured at some angle (often 90") with a suitable spectrometer. To avoid fluorescence, the excitation wavelengths are usually well removed from an absorption band of the analyte [Skoog D. A et al 2007. pp 483].

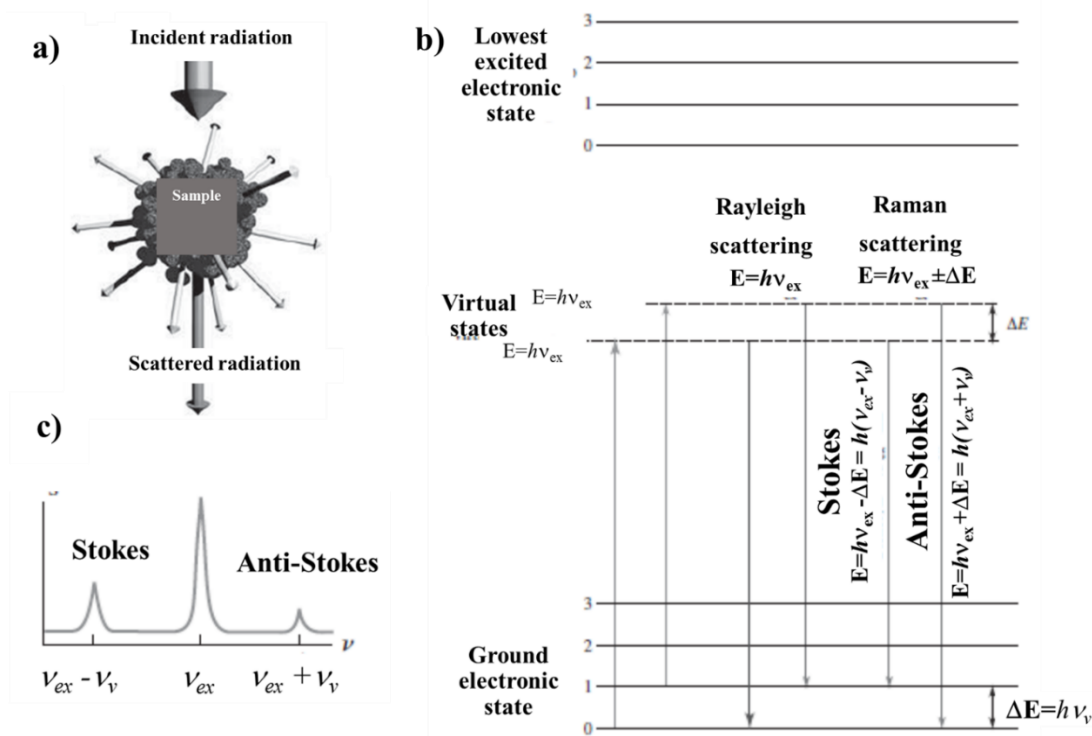


Figure 3.3. a) As Incident radiation of frequency “ ν_{ex} ”, b) Origins of Rayleigh and Raman scattering. (b)The spectrum resulting from the inelastically scattered radiation shows three peaks: one' at $\nu_{ex}-\nu_p$ (Stokes), a second intense peak at ν_{ex} for radiation that is scattered without a frequency change, and a third (anti-Stokes) at $\nu_{ex}+\nu_p$.

The sample is irradiated by a monochromatic beam of energy $h\nu_{ex}$ (II.5a). Because the excitation wavelength is well away from an absorption band, excitation can be considered to involve a *virtual state* of energy level j , indicated by the dashed line in the energy-level diagram of figure 3.3b, which provides a qualitative picture of the sources of Raman and Rayleigh scattering. The heavy arrow on the left depicts the energy change in the molecule when it interacts with a photon from the source. The increase in energy is equal to the energy of the photon $h\nu_{ex}$. It is important to appreciate that the process shown is *not quantized*: thus, depending on the frequency of the radiation from the source, the energy of the molecule can assume any of an infinite number of values, or *virtual states*, between the ground state and the lowest (first) electronic excited state shown in the upper part of the diagram. The second and narrower arrow on the left shows the type of change that would occur if the molecule encountered by the photon happened to be in the first vibrational level of the electronic ground state. At room temperature, the fraction of the molecules in this state is small. Thus, as indicated by the

width of the arrows, the probability of this process occurring is much smaller. The middle set of arrows depicts the changes that produce Rayleigh scattering. Again, the more probable change is shown by the wider arrow. No energy is lost in Rayleigh scattering. As a consequence, the collisions between the photon and the molecule are said to be *elastic*. Finally, the energy changes that produce Stokes and anti-Stokes emission are depicted on the right. The two differ from the Rayleigh radiation by frequencies corresponding to $\pm\Delta E$, the energy of the first vibrational level of the ground state, $h\nu$. If the bond were IR active, the energy of its absorption would also be ΔE . Thus, the Raman *frequency shift* and the *IR absorption frequency* are identical. The relative populations of the two upper energy states are such that Stokes emission is much favored over anti-Stokes. In addition, Rayleigh scattering has a considerably higher probability of occurring than Raman scattering because the most probable event is the energy transfer to molecules in the ground state and reemission by the return of these molecules to the ground state.

When the scattered radiation is of a lower frequency than the excitation radiation, it is called *Stokes scattering*. Molecules in a vibrationally excited state ($\nu = 1$) can also scatter radiation inelastically and produce a Raman signal of energy $h(\nu_{\text{ex}} + \nu_{\text{v}})$. Scattered radiation of a higher frequency than the source radiation is called *anti-Stokes scattering*. Elastic scattering can also occur with emission of a photon of the same energy as the excitation photon, $h\nu_{\text{ex}}$. Scattered radiation of the same frequency as the source is termed *Rayleigh scattering*. Note that the frequency shifts of the inelastically scattered radiation $(\nu_{\text{ex}} + \nu_{\text{v}}) - \nu_{\text{ex}} = \nu_{\text{v}}$, and $(\nu_{\text{ex}} - \nu_{\text{v}}) - \nu_{\text{ex}} = -\nu_{\text{v}}$, correspond to the vibrational frequency ν_{v} . Finally, it should be noted that the ratio of anti-Stokes to Stokes intensities increases with temperature because a larger fraction of the molecules is in the first vibrationally excited state under these circumstances. The intensities of the Stokes and anti-Stokes peaks give quantitative information, and the positions of the peaks give qualitative information about the sample molecule. Some common laser sources for Raman Spectroscopy are shown in the table 3.3

Table 3.3 Some common laser sources for Raman Spectroscopy.

Laser Type	Wavelength, nm
Argon ion	480.0 or 514.5
Krypton ion	530.9 or 647.1
Helium neon	632.8
Diode	785 or 830
Nd-YAG	1064

Note: Here. We use green laser of 532 nm

3.2.5 UV-visible spectra.

The solution of an optical reflectance theory by Kubelka and Munk (1931) and its subsequent simplification by Kubelka (1948) gave rise to the effect of size quantification which is observed through of a shift toward blue, in the maximum of absorption band of a crystal semiconductor of nanometric size generating an increase of the material's energy gap and, of the growing structuring of absorption band [Skoog D.A et al. 2007. pp 470]. The shift in energy gap fits the following relation:

$$\Delta E = E_g - E_g^{bulk} = E_b \left(\frac{\pi a_B}{R} \right)^2 \quad (\text{Eq. 3.10})$$

Where: ΔE : shift in energy gap; E_g : value of energy gap; $E_{g_{bulk}}$: value of energy gap expected for the volume of semiconductor bulk; E_b energy of exciton-bond, a_B ratio Bohr-exciton and R : particle ratio.

The energy of exciton-bond (E_b) is gives for:

$$E_b = \frac{\mu R_0}{m_e \varepsilon^2} \quad (\text{Eq. 3.11})$$

Where; μ : is the reduced mass of the exciton; R_0 : Rydberg constant; ε : material's dielectric constant; m_e : electron mass. Exciton of Bohr-ratio:

$$a_B = \frac{h^2 \varepsilon}{e^2} \left(\frac{1}{m^*_e} + \frac{1}{m^*_h} \right) \quad (\text{Eq. 3.12})$$

Where; m_e^* y m_h^* are the effective masses of the electron and hole respectively. These equations (Eq. 3.10-3.12) containing the base of the size quantization effect. Equation 3.10 shows a dependence of the inverse square of the radius of the particle with the displacement of the energy gap (ΔE). Thus, to decrease the size of the increased particle is generated in the energy gap of the semiconductor material. The diffuse reflectance spectrum become in an absorption spectrum using the Kubelka-Munk $F(R_\infty)$. This equation related the coefficient of absorption k and the diffusion coefficient S , the relation K/S implies that R_∞ if $K \neq 0$

$$F(R_\infty) = K/S = (R_\infty - 1)^2 / 2R_\infty \quad (1) \quad (\text{Eq. 3.13})$$

Where E_g can be obtained using next equation:

$$\alpha(\nu) = A (\hbar\nu - E_g)^{m/2} \quad (\text{Eq. 3.14})$$

Where; α is the absorption coefficient, being $m=1$ for one transition allowed. So, α is proportional to $F(R_\infty)$ and the intercept of energy in a graph $(F(R_\infty) \times h\nu)^2$ vs $h\nu$ gives the “ E_g ” values for a transition allows when the lineal region is extrapolated to zero in the ordered [Skoog D. A et al 2007. pp 470].

3.2.6 Luminescence Properties.

The main photophysical processes occurring in a compound semiconductor when excited by light are schematically illustrated in figure 3.4. Upon irradiation of a compound semiconductor with energy ($h\nu$) greater than or equal to its absorption energy (E_g) (I), electrons in the valence band (VB) are promoted to the conduction band (CB), with the simultaneous generation of holes in the band valence (VB). These photo-excited electrons in CB can easily return to the VB and recombine with holes via different routes. The recombination of photoinduced charges releases energy that is transformed into heat or light energy. The latter is dissipated as radiation, generating luminescent emission from the semiconductor material. The photoinduced electron can recombine with the hole in the VB, generating a photon energy equal to the energy gap ($E_g = E$) according to the excitonic recombination process (II). Alternatively, the photoinduced electron can decay into other states called surface states (distorted bonds, defects or trap sites), causing recombination at a lower photon energy than the energy gap ($E < E_g$). This process is called recombination due to surface defects or traps (III).

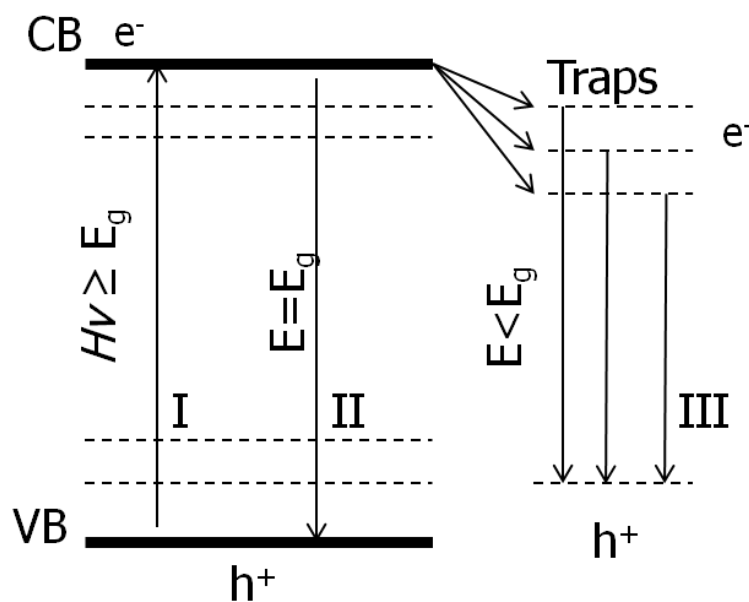


Figure 3.4 Main photophysical processes occurring in a compound semiconductor

3.2.7 X-Ray Photoelectron spectroscopy (XPS).

The phenomenon of XPS is based on the photoelectric effect i.e., the ejection of electrons from a surface due to the impinging of photons as outlined by Einstein in 1905 [Verma H. R. et al 2007]. The X-ray photons, whose absorption is very fast ($\sim 10^{-16}$ s), eject electrons from inner-shell orbitals of the atoms of the surface material and this technique is called electron spectroscopic technique. The kinetic energy, E_K , of these photoelectrons is determined by the energy of the X-ray, $h\nu$, and the electron binding energy, E_B (which represents strength of interaction between electron (n, l, m, s) and nuclear charge). The maximum kinetic energy (E_K) of the ejected electrons is given by:

$$E_K = h\nu - E_B \quad (\text{Eq. 3.15})$$

where h is the Planck constant (6.62×10^{-34} J s) and ' ν ' is the frequency (Hz) of the impinging radiation. The binding energy (E_B) is dependent on the chemical environment of the atom making XPS useful to identify the oxidation state and ligands of an atom. Since the binding energies (E_B) of energy levels in solids are conventionally measured with respect to the Fermi-level of the solid, rather than the vacuum level, this involves a small correction to the equation given above in order to account for the *work function* (E_W) of the solid (figure 3.5). The experimentally measured energies of the photoelectrons are thus given by

$$E_K = h\nu - E_B - E_W \quad (\text{Eq. 3.16})$$

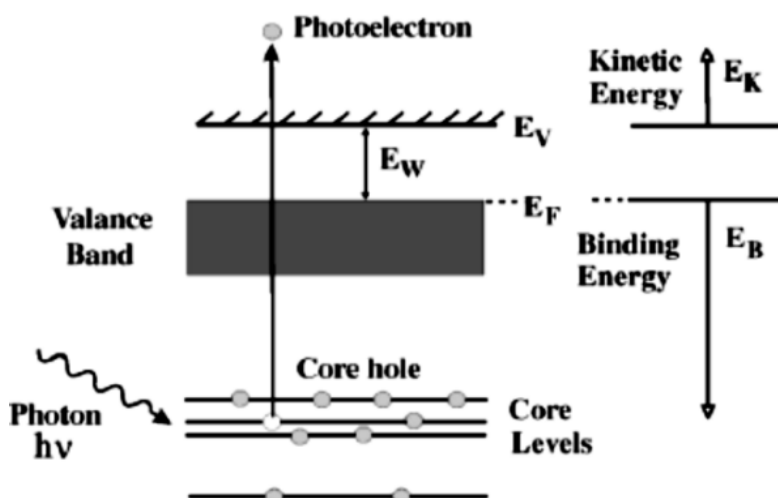


Figure 3.5. Atomic energy levels and the ejection of electrons due to photon-impact.

3.2.8 X-ray diffraction (XRD).

X-rays, Wilhelm Roentgen discovered in 1895, are an electromagnetic radiation whose wavelength (about 10-10m) is between UV and γ rays. The interaction between the electric vector of the X radiation and electrons of the matter that through result in a dispersion of themselves. When this happens in the ordered crystal environment, interference (both constructive and destructive) between scattered rays originate because the distance between the scattering centers are of the same order of magnitude as the wavelength of the radiation. The result is diffraction. Bragg's law [Waseda, Y et al. 2011] states that when an X-ray beam strikes the surface of a crystal at an angle θ , a portion of the beam is scattered by the layer of surface atoms. The unscattered portion of the beam penetrates the second layer of atoms which, again, is a fraction which is scattered and passes to the third layer and so on. Figure 3.6 shows the schematic representation of the derivation of Bragg's law. The cumulative effect of this scattering centers evenly spaced by crystal diffraction beam is, in the same way that the visible radiation is diffracted in a reflection grid.

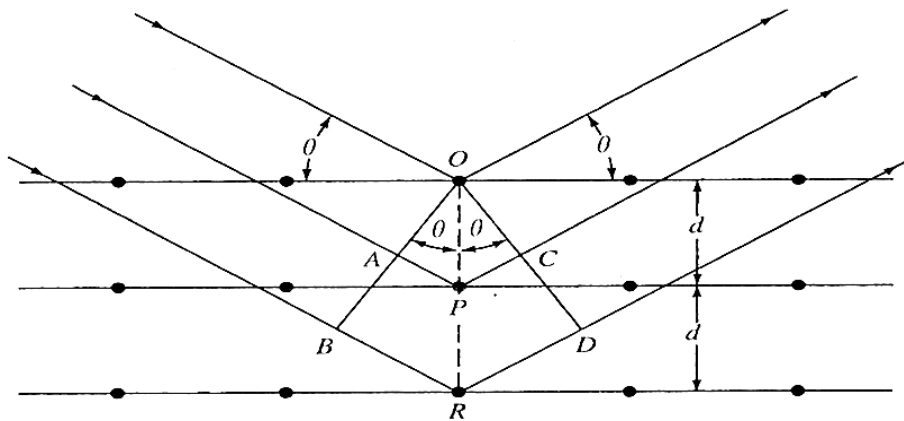


Figure 3.6. Deduction Act Bragg by optical path difference.

Diffraction patters and thickness of these thin films synthetized can be calculated using the Bragg equation (eq. 3.17):

$$n\lambda = 2d\sin\theta \quad \text{Eq. 3.17}$$

3.2.9 X-ray reflectivity (XRR).

This characterisation technique was used for determining the thickness of the deposited thin films. A X' Pert PRO x-Ray diffractometer from PANalytical was used in this work. We performed X-ray reflectivity measurements mainly for the thickness of ALD-MLD thickness. The technique basically consists on irradiating the sample with an X-ray beam at different incident angles and measuring the intensity of the reflected beam with a detector. As a result, we obtain a characteristic intensity profile as a function of the incident angle. This profile consists of the so-called Kiessig fringes, the periodicity and spacing of which depends on the film thickness (see figure 3.7). The film thickness is calculated based on Snell's Law ($\sin \theta_0 = n \cdot \sin \theta_1$) and Bragg's Law described before.

$$\text{Snell's Law: } \sin \theta_0 = n \cdot \sin \theta_1$$

$$\text{Eq. 3.18}$$

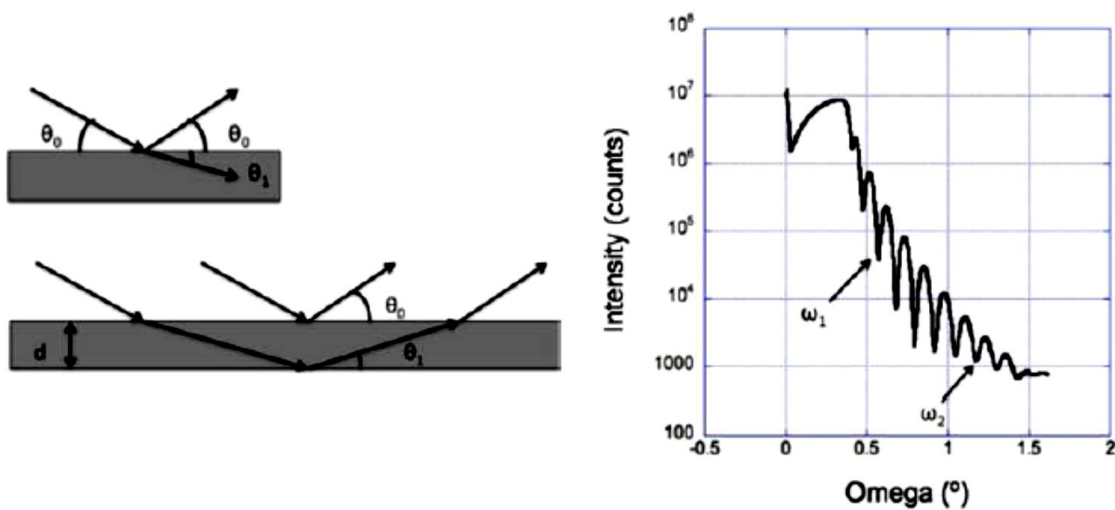


Figure 3.7. a) Schematic representation of Snell's law. The sketch on top represents the incident and reflected x-ray beams, with their corresponding angles. The one below, shows the reflection and penetration of the diffracted beam in a film of thickness "d", and a refraction index "n" (we have used the same notation in the corresponding equation). b) Kiessig fringes resulting from the measurement of the intensity of the reflected beam as a function of the incident angle. The instrument's software uses the incident angles (omega) corresponding to two fringes (for instance, ω_1 and ω_2 pointed with arrows) for calculating the thickness "d".

3.2.10 Transmission Electron Microscopy (TEM).

Electrons are one type of ionizing radiation, which is the general term given to radiation that can remove the tightly bound, inner-shell electrons from the attractive field of the nucleus by transferring some of its energy to individual atoms in the specimen. One of the advantages of using ionizing radiation is that it produces a wide range of secondary signals from the specimen and some of these are summarized in figure 3.8. Many of these signals are used in analytical electron microscopy (AEM), giving us chemical information and a lot of other details about the specimens. AEM uses X-ray energy-dispersive spectrometry (XEDS) (see figure 3.9) and electron energy-loss spectrometry (EELS) [Williams D. V et al 2010].

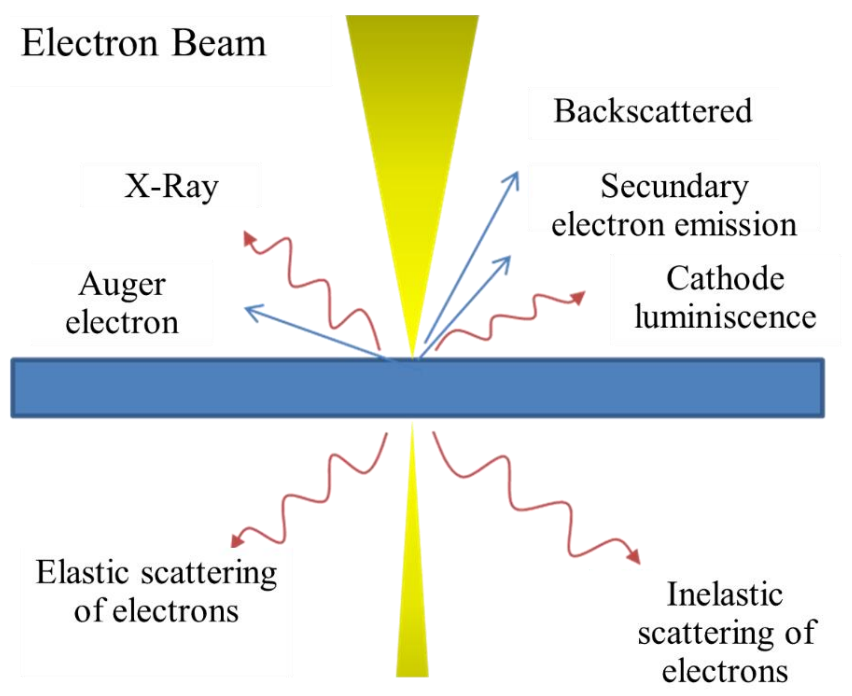


Figure 3.8. Signals generated when a high-energy beam of electrons interacts with a thin specimen.

Most of these signals can be detected in different types of TEM. The directions shown for each signal do not always represent the physical direction of the signal, but indicate, in a relative manner, where the signal is strongest or where it is detected.

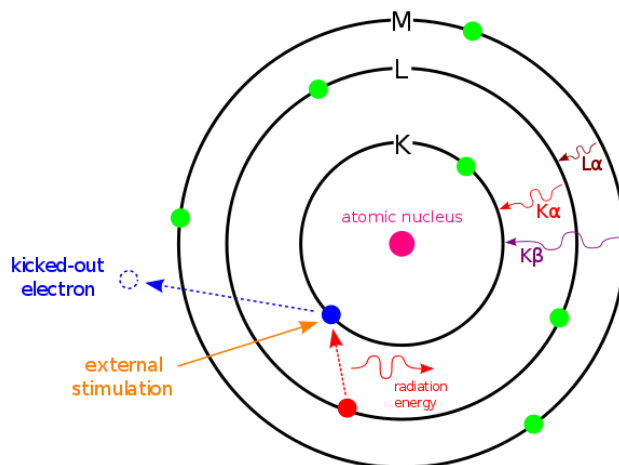


Figure 3.9. Principle of EDS.

3.2.11 Atomic Force Microscopy (AFM).

AFM is a basic technique and inevitable for all nanoscopic research. Like all other scanning probe microscopies (SPM), AFM works by scanning with a tip (or more general a probe) very close to the sample surface. It operates by measuring attractive or repulsive forces between the tip and the sample in constant height or constant force mode (see figure 3.10). Most spectacular are atomic resolutions and manipulation, but most practical applications deal with the (sub) micrometer x/y - and nano z -range [Skoog D. A et al 2007. pp 612].

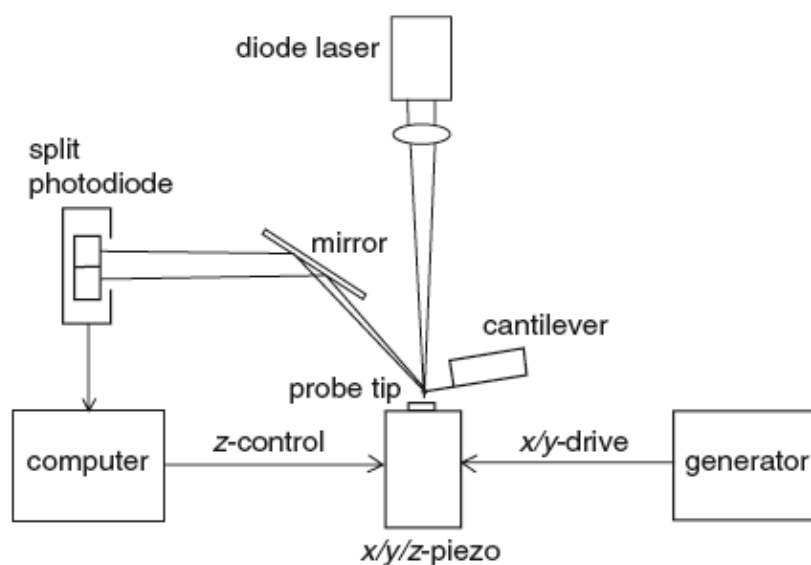


Figure 3.10. Block diagram of a laser deflection contact AFM.

The necessary parts are the x/y and z piezo that are separately actuated by x/y drive and z -control with extreme precision, so that atomic distances can be measured. The sample is mounted on the xyz piezo, close to a sharp tip under the inclined cantilever with its mount. The diode laser light is focused at the end of the cantilever, reflected via mirror to a split diode that provides the feedback signal (topologic information) for maintaining the force by z -piezo response. If the tip is scanned instead of the sample the instrument is called a *standalone microscope*. Data sampling is made at discrete steps by means of an analog-to-digital converter. A computer reconstructs the three-dimensional topological image or projections from the data matrix. Imaging software adds color, height contrast, and illumination from variable directions. Commercial instruments are supplied with all piezo calibration values, and various supply for different SPM techniques as well as instruction manuals and software for imaging. Different piezos are used for different xy scan ranges ($1\ \mu\text{m}\times 1\ \mu\text{m}$ up to $200\ \mu\text{m}\times 200\ \mu\text{m}$) and z ranges (up to $15\ \mu\text{m}$).

3.3 Nanofabrication Methods.

3.3.1 Focus Ion Beam (FIB).

3.3.1-1 FIB as a microtechnology inspection and metrology tool.

Among the most successful applications of FIB in semiconductor technology is failure analysis. In addition, for microsystems, a lot of information can be gained from careful inspection of processed structures. The cross-sectioning capability has proven to be very valuable for microsystems. The most remarkable merit of FIB for technology inspection and metrology is its flexibility. It is very easy to work on individual dies as well as on entire wafers. On the smaller machines the wafer size is limited to 75 mm, while on the larger machines wafers up to 200 mm can be treated. Furthermore, it is also possible to work on packaged devices. The flexibility of processing scale is a consequence of the inherent advantage of FIB: it always processes locally. This enables to (destructively) test or check dimensions on just one or a few dies on a wafer. The unaffected dies on the rest of the wafer can then continue the rest of the normal process. This enables intermediate inspection of, for example, process tolerances, whilst minimizing the loss of good dies.

Practically any material can be milled and visualized, including non-conducting materials (in ion mode). Nonconducting surfaces do not need a special pretreatment (metal coating) as is the case for scanning electron microscopy (SEM) inspection. In terms of deposition, the range of materials that is

commercially available is rather limited however. Standard machines have tungsten or platinum as metals (conductors) and silicon dioxide as an insulator material.

For the cross sectioning of samples, the use of FIB offers several advantages over other techniques. While cleaving or dicing and polishing for SEM investigations take several hours, FIB enables cross sections to be realized within a few minutes time. Furthermore, one is free to determine the precise location of the cross section, and an arbitrary number of subsequent cross section ‘slices’ can be taken on the same sample. The principle of the cross-sectioning technique is illustrated in figure 3.11. In a first step, adjacent to the location of interest, bulk material is removed with a rough and fast single-pass mill. This results in a steep sidewall on the side near the feature of interest. This sidewall is made perfectly vertical and is smoothly polished in the subsequent milling step(s), using each time a finer ion beam and milling regime (polish mill). Finally, the sample is tilted, and the polished side wall is visualized. For normal cross sections (depth of a few micrometres and width 10–15 μm), the whole procedure takes no more than 15 min.

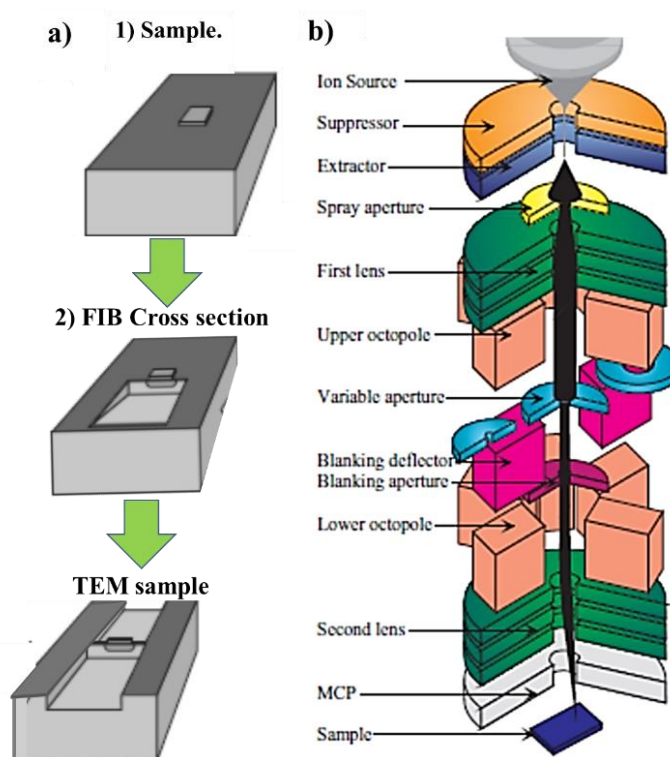


Figure 3.11. Sample with feature of interest can be (a) cross sectioned in the FIB. The section can be advanced until desired feature appears or it can be prepared for inspection in a TEM. (b) Schematic diagram of a FIB ion column [S. Reytjens et al. 2001].

A schematic diagram of a FIB ion column is shown in figure 3.12b. The structure of the column is similar to that of a scanning electron microscope, the major difference being the use of a gallium ion (Ga^+) beam instead of an electron beam. A vacuum of about 1×10^{-7} mbar is maintained inside the column. The ion beam is generated from a liquid-metal ion source (LMIS) by the application of a strong electric field. This electric field causes the emission of positively charged ions from a liquid gallium cone, which is formed on the tip of a tungsten needle. A typical extraction voltage is 7000 V. The extraction current under normal operating conditions is $2 \mu\text{A}$. After a first refinement through the spray aperture, the ion beam is condensed in the first electrostatic lens. The upper octopole then adjusts the beam stigmatism. The ion beam energy is typically between 10 and 50 keV, here we have used 30 keV, with beam currents varying between 1 pA and 10 nA (here we have used 10 pA). Using the variable aperture mechanism, the beam current can be varied over four decades, allowing both a fine beam for high-resolution imaging on sensitive samples and a heavy beam for fast and rough milling. Typically, seven values of beam current can be selected: for example, 1 pA, 5 pA, 32 pA, 99 pA, 672 pA, 1.5 nA and 8 nA (exact values depend on the machine type and the users' preferences). Blanking of the beam is accomplished by the blanking deflector and aperture, while the lower octopole is used for raster scanning the beam over the sample in a user-defined pattern. In the second electrostatic lens, the beam is focused to a fine spot, enabling a best resolution in the sub 10 nm ranges. The multichannel plate (MCP) is used to collect secondary particles for imaging [Reyntjens S. et al. 2001].

The samples that are treated by a FIB are mounted on a motorized five-axis stage, inside the work chamber. Under normal operating conditions, inside this stainless-steel chamber a vacuum in the low 10^{-7} mbar range is maintained. Loading and unloading of the samples is usually done through a load lock, in order to preserve the vacuum inside the work chamber as much as possible. It typically takes a few minutes to load or unload a sample. A gas cabinet containing all applicable gases is present outside the vacuum chamber. All operations such as loading and unloading of samples (partly), manipulating the stage, controlling valves for gas delivery, turning on and off pumps and manipulating the ion beam are carried out via software. Indeed, the complete user interface is realized by means of a computer workstation.

3.3.1-2 Principle of FIB imaging, milling and deposition.

When energetic ions hit the surface of a solid sample they lose energy to the electrons of the solid as well as to its atoms. The most important physical effects of incident ions on the substrate are: sputtering of neutral and ionized substrate atoms (this effect enables substrate milling), electron emission (this effect enables imaging, but may cause charging of the sample), displacement of atoms in the solid (induced damage) and emission of phonons (heating). Chemical interactions include the breaking of chemical bonds, thereby dissociating molecules (this effect is exploited during deposition). Inevitably, during FIB operations, a small amount of Ga^+ ions are implanted in the sample and large numbers of secondary electrons leave the sample [Reyntjens S. et al. 2001].

Here, Pt is deposited on S-4 (section v.3) and AIO-T and AIO-A thin films (section 7.2) to allow the exposition of sheets of S-4 and sample preparation for TEM-micrographs.

3.3.2 Optical lithography.

Optical lithography or UV lithography, also termed Photolithography is a process used in micro and nano fabrication to pattern parts of a thin film or the bulk of a substrate. It uses light to transfer a geometric pattern from a photomask to a light-sensitive chemical "photoresist", or simply "resist," on the substrate [Z. Cui. 2017]. A series of chemical treatments then either engraves the exposure pattern into, or enables deposition of a new material in the desired pattern upon, the material underneath the photo resist. General photolithography has five basic procedure; 1° **Cleaning:** wet chemical treatment (e.g., isopropanol/water solution) is used to remove organic or inorganic contamination; 2° **preparation:** The wafer is initially heated to a temperature sufficient to drive off any moisture that may be present on the wafer surface, 150 °C for ten minutes is sufficient; 3° **photoresist application,** the wafer is covered with photoresist by spin coating; 4° **exposure and developing:** After prebaking, the photoresist is exposed to a pattern of intense light. The exposure to light causes a chemical change that allows some of the photoresist to be removed by a special solution, called "developer", and 5° etching: In etching, a liquid ("wet") or plasma ("dry") chemical agent removes the uppermost layer of the substrate in the areas that are not protected by photoresist. Figure 3.12 exhibits a schematic representation of printing process [Cui. Z et al 2017].

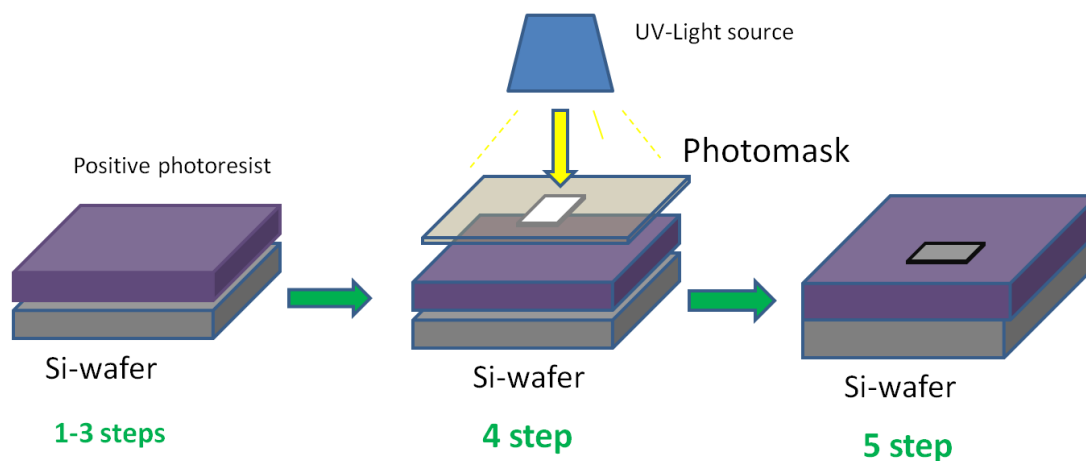


Figure 3.12 Schematic representation of photolithography's process.

Lithographic photomasks are typically transparent fused silica blanks covered with a pattern defined with a chrome metal-absorbing film. Photomasks are used at wavelengths of 380 nm, 365 nm, 248 nm, and 193 nm. Photomasks have also been developed for other forms of radiation such as 157 nm, 13.5 nm (EUV), X-ray, electrons, and ions; but these require entirely new materials for the substrate and the pattern film. The photomask used in this thesis has squares pattern shape with different sizes since 100 μm to 400 μm .

Photoresists are classified into two groups: positive resists and negative resists.

- 1) A **positive resist** is a type of photoresist in which the portion of the photoresist that is exposed to light becomes soluble to the photoresist developer. The portion of the photoresist that is unexposed remains insoluble to the photoresist developer.
- 2) A **negative resist** is a type of photoresist in which the portion of the photoresist that is exposed to light becomes insoluble to the photoresist developer. The unexposed portion of the photoresist is dissolved by the photoresist developer.

3.3.3 Electron Beam Lithography (EBL).

EBL is one of the most important techniques in nanofabrication, allowing not only the direct writing of structures down to sub-10 nm dimensions, but also enabling high volume nanoscale patterning technologies such as (DUV and EUV) optical lithography and nanoimprint lithography through the formation of masks and templates [M.A. Mohammad et al.2012]. In short, it involves the exposure by a highly-focused electron beam to dramatically modify the solubility of a resist material during a subsequent development step, see Figure 3.13.

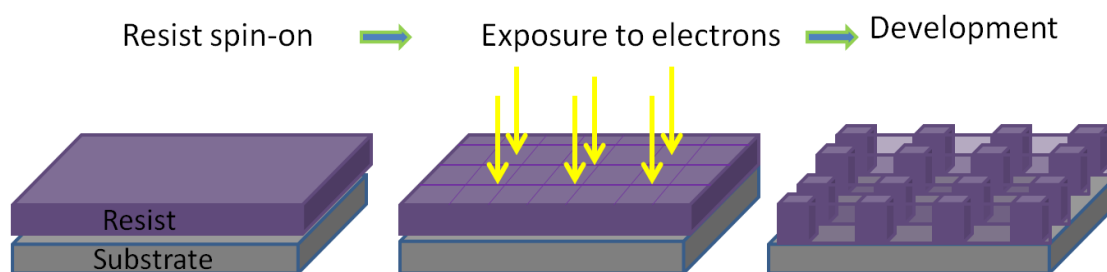


Figure 3.13. Outline of EBL process steps to form a nanoscale pattern in a positive-tone resist layer.

EBL was originally developed using scanning electron microscopes to which a pattern generator and beam blanker was added to control which areas of the viewing field are exposed (see Figure 3.14 for a schematic description of an EBL system). Modern EBL tools are fully dedicated patterning systems like e.g., Raith 150 TWO commercial EBL system (used here) that employ high brightness electron sources for faster throughput and high resolution mechanical stages to be able to expose step-by-step large substrates under the relatively narrow field of focus of the electron beam. These direct write systems have the advantage of extremely high resolution and the ability to create arbitrary patterns without a mask. The key objectives of EBL writing are to achieve arbitrary patterns in the resist with high resolution, high density, high sensitivity and high reliability [Mohammad M. A. et al.2012].

These characteristics are interrelated in a complex fashion. The key determinants will be the quality of the electron optics (e.g., the ability to create a finely focused spot), the choice of resist, substrate and developer, and the process conditions: electron beam energy and dose, and development time and temperature. Factors that complicate these objectives are delocalization of electrons due to forward and backscattering (proximity effects), collapse of the pattern due to swelling and capillarity forces, and fluctuations in the sizes of features (line edge roughness).

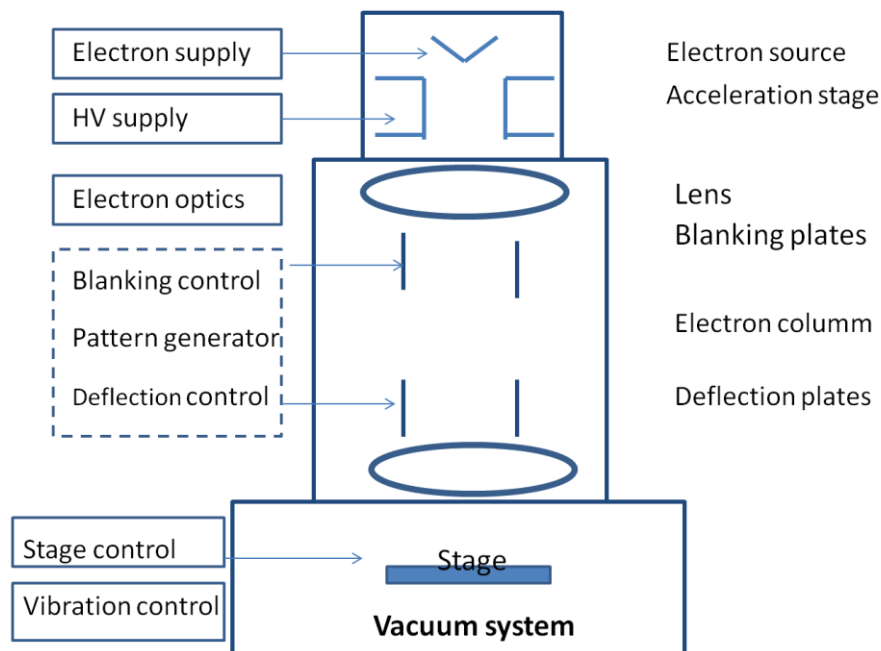


Figure 3.14. Electron beam exposures systems: (a) schematic diagram, (b) Raith 150TWO commercial EBL system [Mohammad M. A. et al.2012].

3.3.3-1 Electron Transport.

The first requirement for a high-quality beam is a stable, high brightness electron source, such as one employing thermal field emission. The quality of the spot is determined by the electron optics and degree of focus. It is necessary to have high positional accuracy with limited astigmatism and small spot size [Mohammad M. A. et al.2012]. The electron column is under vacuum to reduce gas scattering of the beam, but divergence of the beam does result from mutual electrostatic repulsion by the electrons. This effect is more pronounced at higher currents and lower energies. Notwithstanding this, commercial EBL systems can usually deliver a spot size of just a few nanometers. Unfortunately, other factors such as scattering will usually limit the final resist pattern to a larger size. As the electrons enter the resist, they begin a series of low energy elastic collisions, each of which will deflect the electron slightly. This forward scattering broadens the beam by an amount that increases with thickness, and this effect is more pronounced at low incident energies. In addition to forward scattering, there is also backscattering to consider.

Typically, most of the electrons pass entirely through the resist and penetrate deeply into the substrate. Some fraction of those electrons will eventually undergo enough large angle collisions to re-emerge into the resist at some distance from the point at which they left it. At higher energies, these

backscattered electrons may cause exposure microns away from where the beam entered. This leads to the so-called proximity effect where electrons writing a feature at one location increase the exposure at a nearby feature, causing pattern distortion and overexposure. The density of features becomes an important factor in determining necessary exposure levels. Backscattering can be minimized by exposing on a thin membrane substrate. Another electron transport consideration is secondary electrons. These are low energy (a few to a few tens of eV) electrons produced by ionizations resulting from inelastic collisions by the primary incident electrons. Because of their energy, secondary electrons have short range (several nanometers) but may ultimately limit the resolution possible with EBL.

A final transport issue is electrostatic charging, particularly if writing onto an insulating substrate. If there is no pathway for the absorbed electrons to dissipate charge will build up and defocus the electron beam. In such cases, a thin metal or conductive polymer layer is required above or below the resist. Inelastic collisions of electrons with the resist result in ionization (secondary electron generation), which is accompanied by physico-chemical changes in the resist. Just as with optical lithography, EBL can employ two classes of resist. Positive tone resists undergo a conversion from low to high solubility upon exposure to electrons. The classic example is PMMA (poly-methyl methacrylate) which is a long chain polymer (Figure 3.15a) that is broken into smaller, more soluble fragments by the electron beam (Figure 3.15b). Another common positive resist is ZEP 520 which also consists of a long chain polymer.

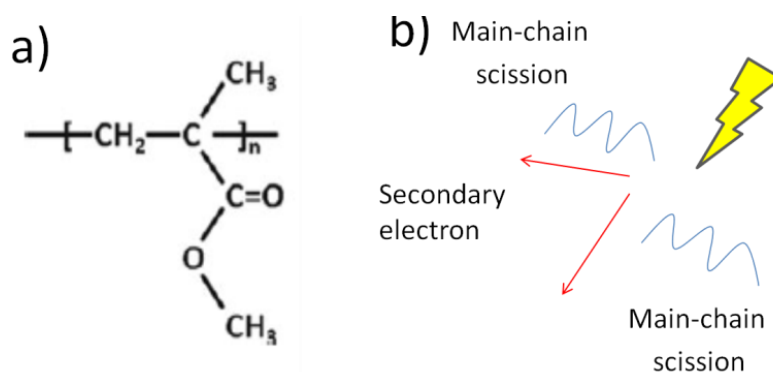


Figure 3.15. (a) Polymer subunit of poly (methyl methacrylate) and (b) scission of the polymer chain during EBL exposure.

In a negative tone resist, the electrons convert the material to low solubility. The prime example here would be HSQ (hydrogen silsesquioxane) which undergoes a cross-linking reaction to combine smaller polymers into larger, less soluble ones [Mohammad M. A. et al.2012]. Several other negative resists have been recently compared [Mohammad M. A. et al.2012]. The most common positive resist,

PMMA, consists of very long polymer chains with masses of 496 and 950 kDa being common. With such long chains, it takes many scission events before the resulting fragments become significantly soluble. Hence, the distribution of fragment sizes becomes an important factor in understanding the relationship between exposure dose and development behavior.

Note: here PMMA-495 kDa was utilized in section 7.1.

3.3.3-2 Resist Developing

After exposure, the resist is typically immersed in a liquid developer to dissolve the fragments (positive tone) or non-crosslinked molecules (negative tone). Thus, during development, the solvent penetrates into the polymer matrix and starts to surround the fragments. As the molecules start to interact, a gel is formed.

The thickness of the gel layer will depend on the amount of fragmentation and the strength of the solvent. Swelling of the polymer can also result. Once surrounded by solvent, the fragments detach from the matrix and diffuse into the solvent. Longer fragments are less mobile and more strongly bound to the matrix and take longer to dissolve. More powerful solvents will remove a longer fragment which is not always desirable if high resolution is required. Exposure and development are interrelated as short exposure with long or aggressive development can be equivalent to heavier exposure with short development. This can lead to some ambiguity between the terms underdeveloped and underexposed or overdeveloped and overexposed. As will be discussed further below, the kinetics of the dissolution process becomes quite important to the optimization of EBL necessitating understanding of these factors at a detailed level. Often a mix of solvents (such as 1:3 methyl isobutyl ketone with isopropyl alcohol for PMMA) is used to tailor dissolution behavior. An issue that arises if the resist is overdeveloped is the degradation of the resist substrate bond and the capillarity forces that result as the solvent is removed. These lead to the mechanical failure of the resist structure resulting in pattern collapse.

The developer used was a commercial mix of isopropyl alcohol and methyl isobutyl ketone (MIBK / IPA) to dissolve 495 PMMA resist.

3.3.3-3 Process Parameters

As has been implied above, there is a large number of parameters affecting the EBL process in a complex, interacting fashion, such as; exposure energy resolution, sensitivity, proximity, pattern density proximity, pattern quality, resist thickness sensitivity, resolution, pattern quality, Development temperature Sensitivity, resolution, exposure window, exposure dose pattern quality, resist material sensitivity, resolution, contrast, development time sensitivity, resolution, exposure window.

This excludes secondary factors such as resist polymer chain length which can impact sensitivity and contrast, or the use of techniques such as ultrasonic agitation to reduce development times and improve clearance, or the use of critical point drying [Mohammad M. A. et al.2012] to minimize pattern collapse. The objective of manipulating these parameters is to achieve a high resolution, high quality, high throughput result with large process windows to maximize yield and reproducibility.

CHAPTER IV

EXPERIMENTAL PROCEDURE

Sujeto a confidencialidad por la autora

CHAPTER V.

Zn METALATION-VPM AND SPECIFIC BOND FUNCTIONALIZATION: SOFT MOLECULES AND NANOSTRUCTURES.

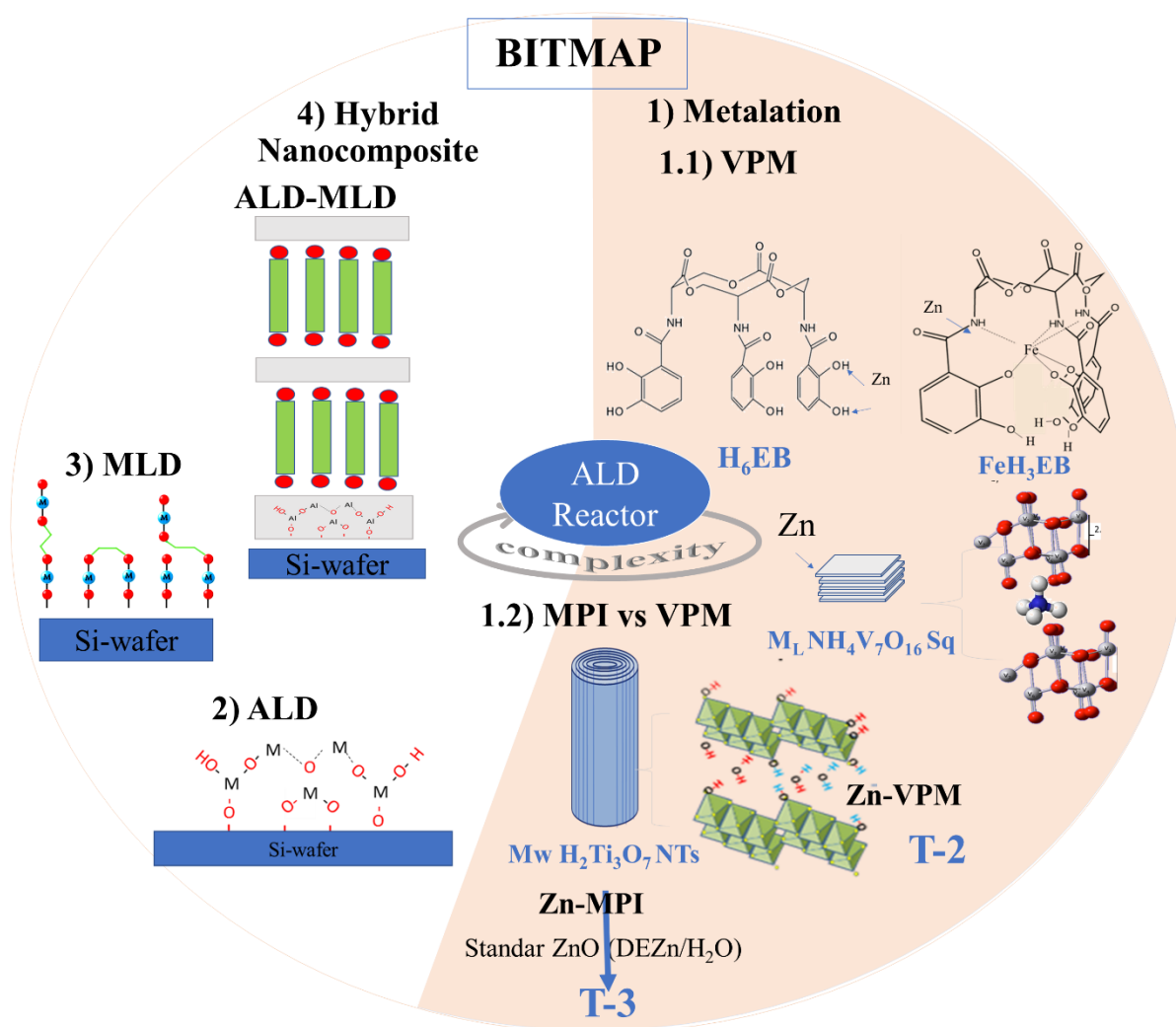
Sujeto a confidencialidad por la autora

CHAPTER VI.

**H-O and H-N SPECIFIC BOND
FUNCTIONALIZATION
ZnO NPs NUCLEATION BY
Zn-METALATION VPM vs MPI
OF Mw-H₂Ti₃O₇ NTs.**

Partes de este capítulo sujetos a confidencialidad por la autora

In this section, we continue the focus on the use of VPM process (only one precursor (here, DEZn) is utilized to functionalize) but we compare it with MPI process (two precursors, DEZn/H₂O, are utilized) to functionalize M_w-H₂@Ti₃O₇ NTs with Zn. This chapter explores the effect of Zn-metalation over the morphology and properties of M_w-H₂Ti₃O₇ NTs using TEM-EDX, UV-Vis, IR, luminescence and photo catalysis.



Note: The results here exposed were started in the Experimental department-II of MPI-Halle in 2011 under supervision of Dr. M. Knez (ALD-support) in collaboration with CEDENNA-Chile and continued in CIC-Nanogune, U. Chile and UTEM-Chile.

6.1 Zn-metalation of $M_W\text{-H}_2\text{Ti}_3\text{O}_7$ NTs by VPM and MPI processes.

Chapter 6. Specific aims.

- 1) Synthesize $(\text{ZnO})\text{Ti}_3\text{O}_7$ NTs by Zn-metalation using DEZn and DEZn/ H_2O .
- 2) Characterize the products by XRD, TEM, IR and UV-vis spectra.
- 3) Explore the band gap of energy "Eg" of the products using diffuse reflectance spectra (Kubelka-Munk).
- 4) Explore the photocatalytic properties of the products.

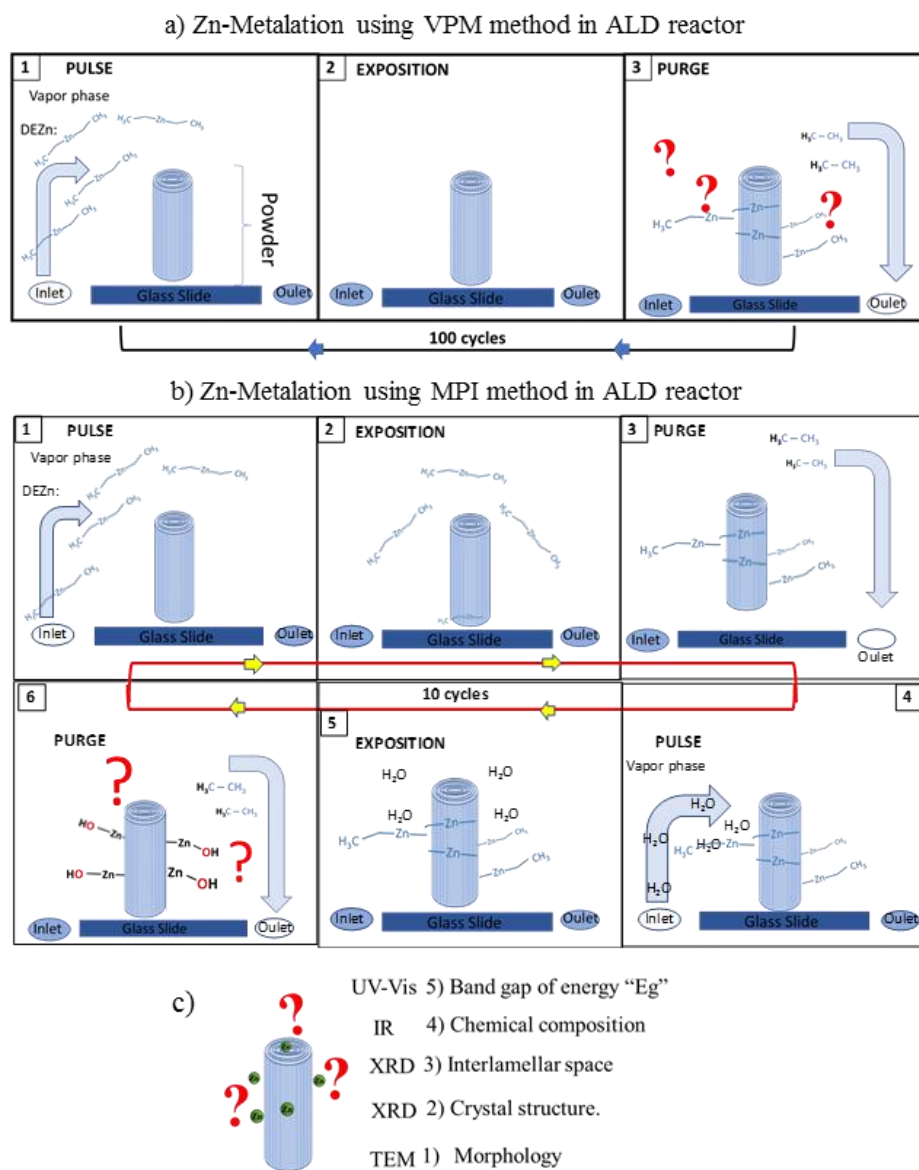


Figure 6.1 Chapter VI sequence of experiments and characterization; a) T-2 and b) T-3.

Tentative application: Biosensor, organic pollutants degradation, photonic crystals (PCs) and semiconductors.

“Motivation for Nanodevices”

Materials with high electron mobility for efficient electron transport (e.g., low E_g) are desirable for photoanodes of high energy conversion devices based in light harvesting, e.g., dye-sensitized solar cells (DSC) and sensors. TiO_2 exhibits an excellent sensor, battery and photocatalytic properties, and photovoltaic power conversion efficiencies (PCEs), however its electron mobility is low ($0.1\text{-}4\text{ cm}^2\text{ V s}^{-1}$), which affects the electron transport rate. A monocrystalline growth of semiconductor materials is of great interest in semiconductor technology, since monocrystalline films like w-ZnO usually have higher mobility of carriers [Williams, V.O. et al 2012, Hernández S. et al 2014]. On the other hand, the photonic crystals (PCs) [Garcia P. et al 2006] have turned out to be a promising tool to engineer at will, or even inhibit, the emission of light. In these systems, the refractive index is modulated periodically in one, two, or three dimensions. This fact provokes the appearance of energy intervals, called photonic bandgaps (PBG), for which the propagation of light is prevented. The combination of luminescent materials with PCs, i.e, opals, is one of the open challenges being addressed nowadays. The relatively high ZnO refractive index provides enough dielectric contrast in the inverted structure to open additional pseudogap (pGs) in the high-energy regime, which have recently been used for enabling laser emission. Its large range of transparency allows ZnO to host emitters in a broad spectral range from the IR to the UV with no hindrance derived from absorption. All these reasons make ZnO an appropriate template material where quantum dots (QD) can be conformally self-assembled.

According to Hernández et al [Hernández, S., et al 2014.] the efficient application of the (ZnO) TiO_2 has had a dual function: to enhance the photoactivity and to increase the photodegradation stability. There are reports about layer-by-layer deposition to obtain a rutile TiO_2 shell on the surface of ZnO NWs, but not about the synthesis of (ZnO) Ti_3O_7 single crystal arrays.

We postulate that structures such as single crystals arrays like $\text{H}_2\text{Ti}_3\text{O}_7$ NTs with high surface area could favour the growth of single crystal w-ZnO and opals arrays.

“Motivation for Biological-Chip”

Semiconductor metal oxide (SMO) materials such as SnO_2 , ZnO, TiO_2 , WO_3 , etc. are considered to be better materials for chemical sensors as compared to other gas sensing materials/techniques such as conducting polymers, electrochemical cell and optical fibers. Since wider band gap semiconductor improves the fluorescent quantum efficiency substantially, with resulting core-shell QDs, Q-Wells and Q-Wires having PL quantum yields comparable to those of organic dyes, the mobility of carriers

of the sensor is often damage [Patra, M.K., et al. 2008]. From here, arouse the question if Mw-TiO₂ NTs could improve its electron transfer by adding a ZnO monocrystals between and around of those TiO₂-walls without damage its fluorescent? Will it improve or damage the photocatalytic properties of such news materials?

Alkali metal titanates (A₂Ti_nO_{2n+1}) systems like H₂Ti₃O₇ are attractive due its high surface-to-volume ratio conferred for their layered open crystal structure, offering extremely large ion exchange capacity, fast ion diffusion and intercalation, and high surface charge density, where the negatively charged two-dimensional titanium containing sheets are separated to a large distance by exchangeable cations and molecules in the interlayer. H₂Ti₃O₇ has its own crystal structures of layered or tunnel type (see figure 6.2). It exhibits a monoclinic lattice with parallel corrugated layers of edge sharing TiO₆ octahedra stepped by every octahedral [Zhang, Y et al 2015, Feist T. P. 1992] synthesized by topotactic exchange of sodium for proton from the layered trititanate Na₂Ti₃O₇ [Zhang, Y et al 2015]. The open crystal structure of layered titanate permits easy and uniform doping of atoms or molecular assembly, which is hard to achieve if working directly with the more compact TiO₂ polymorphs [Zhang, Y et al 2015].

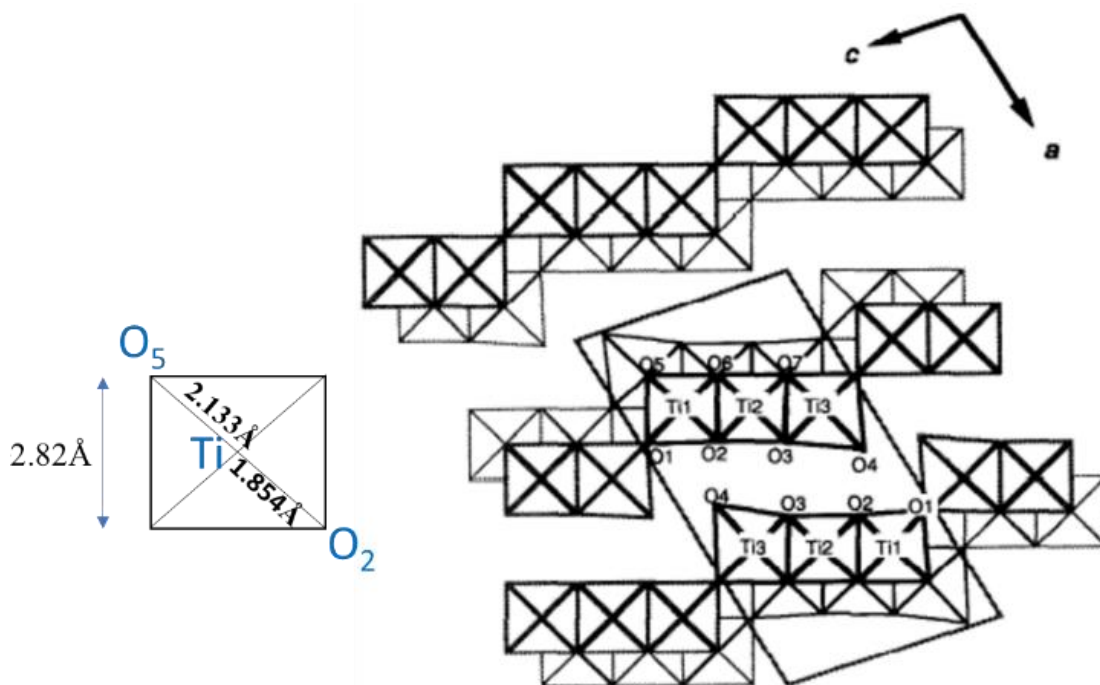


Figure 6.2 The framework structure of H₂Ti₃O₇ from 47-0561 JCPDS [Feist T. P. 1992].

CHAPTER VII.

ALD

&

MLD

PROCESSES.

CHAPTER VIII.

DISCUSSION

Hypothesis.

ALD is a powerful tool to obtain the synthesis of hybrid layer by layer organic-inorganic and inorganic-inorganic nanocomposites as well as H-O and H-N specific bond functionalization for example, Zn-metalation of soft molecules and nanostructures.

In this thesis, four ALD processes were explored at low temperature; vapor phase metalation (VPM), multiple pulsed vapor-phase infiltrations (MPI), ALD and molecular layer deposition (MLD). The implementation of VPM process, where only metal precursors participate; here DEZn, on soft molecules like Enterobactin and FeEnterobactin with free O-H and N-H bonds, leading to the development of new and innovative specific atomic functionalization of soft molecules; EnterobactinZnOH and FeEnterobactinZnOH, at room temperature and solvent free.

Instead, the effect of VPM process on soft-nanostructures with empty sites or/and vacancies, and interlamellar OH groups like in $M_L-(NH_4)V_7O_{16}$ nanostructured square and $M_w-H_2Ti_3O_7$ nanotubes drives to the metamorphosis of atomic crystal structure, as in $(NH_4)V_7O_{16}$ triclinic P-1 to $Zn_3V_3O_8$ cubic Fd-3m and $H_2Ti_3O_7$ monoclinic to zinc meta-titanate ($ZnTiO_3$) and zinc ortho-titanate (Zn_2TiO_4) cubic inverse spinel (in different rates) as well as the growth of monocrystals of w-ZnO between layers allowing single layer by layer arrangement, and inside and around of the nanostructures without affect their morphologies, but rather of its optical and magnetic properties. This also performed at low temperature ($\sim 100^\circ C$) and solvent-free.

In the case of MPI process, where two precursors participate separately; here DEZn and H_2O , on $M_w-H_2Ti_3O_7$ NTs leads to the nucleation of opals of nanoparticles of w-ZnO around the nanotube (cactus-like) affecting the morphology and surface properties. In addition to the growth of w-ZnO nanoparticles inside of the nanotubes and between layers, and the dislocation of some Ti_3O_7 layers together with typical peaks of zinc ortho-titanate (Zn_2TiO_4) and zinc meta-titanate ($ZnTiO_3$), suggest a metamorphosis of $H_2Ti_3O_7$ layers to zinc titanate in some regions of the layers also at low temperature ($120^\circ C$).

While control of the precursor release parameters can be neglected in VPM and MPI processes, this is a mandatory requirement in both; ALD and MLD processes, for the growth of stoichiometric films over wafer scale and high area uniformity. The ALD growth of uniform $MxOy$ thin films where M stands for V, Mn, Sn or Zn was successfully undertaken.

The preliminary results show successful deposition of α -MnO₂, α -V₂O₅, Sn_xO_y, and ZnO stoichiometric films, uniform over large areas as characterized by XRR, XRD, and AFM. The use of H₂O₂ is better than H₂O for the removal of organic ligand from organometallic precursor when low-temperature growth is required like it was showed for the case

of the deposition of α -MnO₂ and Sn_xO_y using (EtCp)₂Mn and (TDMA)Sn like the metal source in a temperature range since 100 to 200°C and 125 to 175°C, and since 75°C to 125°C for VTOP/H₂O. The low GPC of 0.2 nm/cycle and 0.1 nm/cycle for the deposition of α -MnO₂ and Sn_xO_y, were consistent with those reported for George S.M et al [George S.M et al 2009b] and Elam J. W. et al [Elam J. W. et al 2008] of 0.1 and 0.12 nm/cycle and characteristic for ALD process. Despite this ALD's limitation, the deposition of crystal structures of α -MnO₂ and α -V₂O₅ at low temperature (~100°C) were successful like showed their XRD patterns. The deposition of α -V₂O₅ and ZnO on AAO disc lead to the synthesis of nanotubes with a controlled diameter of 200nm and wall thickness of 20 and 90 nm, respectively. The deposition of α -V₂O₅ at low temperature over square patterns obtained from positive photoresist and PMMA 495A resist, with melting point ~100°C, leads to the synthesis of α -V₂O₅ perfect squares of varied sizes since 100 μ m to 500 nm. Those results, points towards the possible growth of these oxides which can be considered as energy materials which can form easily 1-D, 2-D and 3D nanostructures using patterns.

Finally, the growth of alucone thin films (AIO-T and AIO-A, T: terephthalate and A: adipate) by ALD and MLD permitted to obtain stoichiometric thin films with large area uniformity in both cases, as shown in XRR, XRD and AFM-microscopy data. The use of bifunctional monomers (aromatic and aliphatic carboxylate) in the growth of AIO-T and AIO-A thin films lead to a lamellar phase and to an amorphous one, respectively. The use of DFT allowed discerning which the predominant structure in the AIO-T thin film by the IR and UV-Vis spectroscopic correlation, for this case model 4 and terephthalate agreed with experimental results. According to with the values of frontier orbitals of those two structures, it was possible to predict their applications like electrolyte and anode for batteries. Low Eg of 0.05 eV of AIO-T thin film imposes that the cell voltage shall be $eV_{oc} < 0.05$ eV if AIO-T is considered like polymer electrolyte, instead if it is considering like anode this value turn to -0.3 eV similar to Lithium terephthalate of -1eV. This point forward to the potential applications of alucones thin film in carboxylates-based energy storage concepts.

In the aspect of applicability, this study permits to project to the use of functionalized Siderophores by VPM process like an innovative and powerful drug as a “Trojan horse” to face the antibiotic resistance reported for WHO reports in 2011 [WHO/RHR/11.14] and 2014 [WHO/HTM/TB/2014.0/] about the multi-resistance of some strain of tuberculosis (TBC) (second-most common cause of death from infectious disease, after those due to HIV/AIDS), Cholera, meningitis, Leptospirosis, E. Coli and sexual diseases like N. Gonorrhoea.

This manner, this thesis allows to point out to the materials here studied to the development of advanced nanodevices like nanobatteries, Nanosensors, memory-nanochip and lab-on-chip and control drug delivery system. This is supported by next patents; Bio lab-on-chip and method of fabricating and operating the same [WO 2009061017 A1], Nano-battery systems [US 6586133 B1] and Nano memory, light, energy, antenna and strand-based systems and methods [US 9117550 B2]

With respect to the methods of synthesis, via wet-chemistry is possible to synthesize analogues of Enterobactin such as SERSAM, TRECAM and TBA7, often with backbone changes that promote the binding antibiotic molecule to the siderophore (Trojan horse antibiotic strategies), leading in most cases to the damage of catechol reactivity to physiological pH and consequently frustrating FeSiderophore-Drug recognition for the FepA protein receptor. However, VPM process offer a suitable alternative of functionalization, at room temperature, solvent free, faster and environmentally friendly.

Using the way of wet-chemistry is also possible to obtain complex nanostructures like nanotubes and squares, nonetheless they can be obtained by the deposition of ALD-MLD thin films on models like AAO-disc and resist patterns, offering a new route of synthesis where their main characteristics are; solvent-free synthesis, low-temperature synthesis, and control of the deposition of the matter at the atomic level.

Concerning to the methods of characterization, broad characterization methods are available for a wide type of nanostructures and molecules. The materials explored in this thesis reveal that XRD, IR, RAMAN, NMR and MALDI-TOF techniques in conjunction with XPS and several techniques of microscopies such as; ATR, RAMAN, HRTEM, ESEM, SEM/FIB-nanolab and AFM are useful for providing information about Zn metallized materials by VPM and MPI processes and the growth of uniform thin films.

Although only DFT calculations were performed to correlate NMR, IR and UV-Visible spectra, the good correlation results allow confirming together with molecular dynamics and docking, the applicability of theoretical methods as well as the prediction of properties.

Regarding the type of samples for ALD reactor, since the chemical structure of Enterobactin and FeEnterobactin remains to the organometallic precursor; here diethylzinc (DEZn) performed at room temperature together with the broad list of ALD precursors in the market which can be performed at room temperature like DEZn and trimethylaluminium (TMA). The soft molecules used here permits to extend the applicability of ALD to pharmaceutical field.

Since nanostructures remain after to the reaction with organometallic precursors, the implementation of ALD processes at low temperature is a potential route to transform those nanostructures and molecules with poor properties in new and innovative multifunctional atomic structures, establishing to ALD processes like a forefront tool enable atomic level control.

In addition, the use of resist patterns and other templates like AAO or nanocomposites provides forefront platform for the build of novel devices. The extensive list of ALD precursors available in the market support the growth toward to the multifunctionality of nanodevices, only limited for the strategies of synthesis and design of the device.

Thus, in this thesis, we have shown the versatility of ALD processes to realize novel thin films and pursue various functionalization strategies with the control of the functionalization of molecule and crystal structures, and growth at the atomic level which leads to the development of multifunctional nanodevices with defined and transportable morphologies.

CHAPTER IX.

CONCLUSIONS

AND

FUTURE WORK.

IX.1 CONCLUSIONS

Zn metalation-VMP process of soft molecules leads to bond-specific functionalization becoming it a forefront tool for devices based on organic molecules and the pharmaceutical field. This in a solvent-free environment and room temperature.

Zn metalation-VPM process provides a way to functionalize soft nanostructured materials with empty sites, vacancies defects and interlamellar spaces by the growth of w-ZnO monocrystals between layers and their metamorphosis to zinc metalates which drives to change their crystal structure and thereby their optical and magnetic properties. This without changing their morphologies, in a solvent-free environment and low temperature.

Zn metalation-MPI process on Mw-H₂Ti³O₇ NTs promotes the nucleation of opals w-ZnO around of nanotubes, w-ZnO monocrystals between layers and inside of the nanotubes which drive to the synthesis of the layer by layer inorganic nanocomposites. Nanomaterials potentially useful as photoanodes for dye-sensitized solar cells (DSCs) and sensors.

The development of new and innovative atomic structures displaying multifunctional properties goes together with progress in advanced processes which enable atomic level control. One leading deposition technique is Atomic layer deposition (ALD), which has emerged as a powerful tool for bond-specific functionalization and the growth of stoichiometric films over wafer scale and high area uniformity.

Semiconductors based on metal oxide like α -V₂O₅ and α -MnO₂ lead to the growth of stoichiometric films over wafer scale and high area uniformity at low temperature facilitating the developed of multifunctional nanodevices based in resist patterns.

Multifunctional nanomembranes can be easily constructed by ALD-MLD processes performed at a low temperature extending the utility of those materials to the technologies based on the polymer electrolyte and carboxylates anodes.

DFT, MD and docking are the forefront computational tools for the calculation and prediction of the spectroscopic and electronic properties of atomic structures, in the pharmaceutical and energy storage field.

The development of new and innovative atomic structures displaying multifunctional properties can be gotten by Atomic layer deposition (ALD), vapor phase metalation (VPM), multiple pulsed vapor-phase infiltration (MPI), molecular layer deposition (MLD).

Thus, in this thesis, we have probed the versatility of ALD processes to realize novel thin films and pursue various functionalization strategies.

IX.2 FUTURE WORK.

To functionalize actual and new siderophores with organic fragments, predict their properties by implementing computational tools as DFT, MD and docking, and carried-out microbiological assays.

To get individual applications of the nanomaterials here studied by using the templates obtained by photolithography and nanolithography obtained in this thesis but not specified, like shows in figure 9.1.

To improve some properties if it will be necessary by means of their functionalization using VPM and MPI processes or synthesized new materials.

To get an integrated multifunctional nanodevice using the nanomaterials here investigated, we have special interest on integrated Lab-on-Chip & Control Drug delivery system, magnetic-memory nanochip. Figure 9.2 shows a scheme of the integrated multifunctional nanodevice desired.

Additionally, we have used Zn metalation-VPM to functionalize other siderophores like citrate, and other nanomaterials based on vanadium oxide as; urchins, bearings and nanotubes, and lamellar nanocomposites such as; (HAD)-(Li)MoS₂, (Na)Bentonite, (Carboxylicacid)ZnO, (DDA)TiO₂ with Zn and Ti and ZnO nanowires with Ti. We expect to complete those experiment in the future.

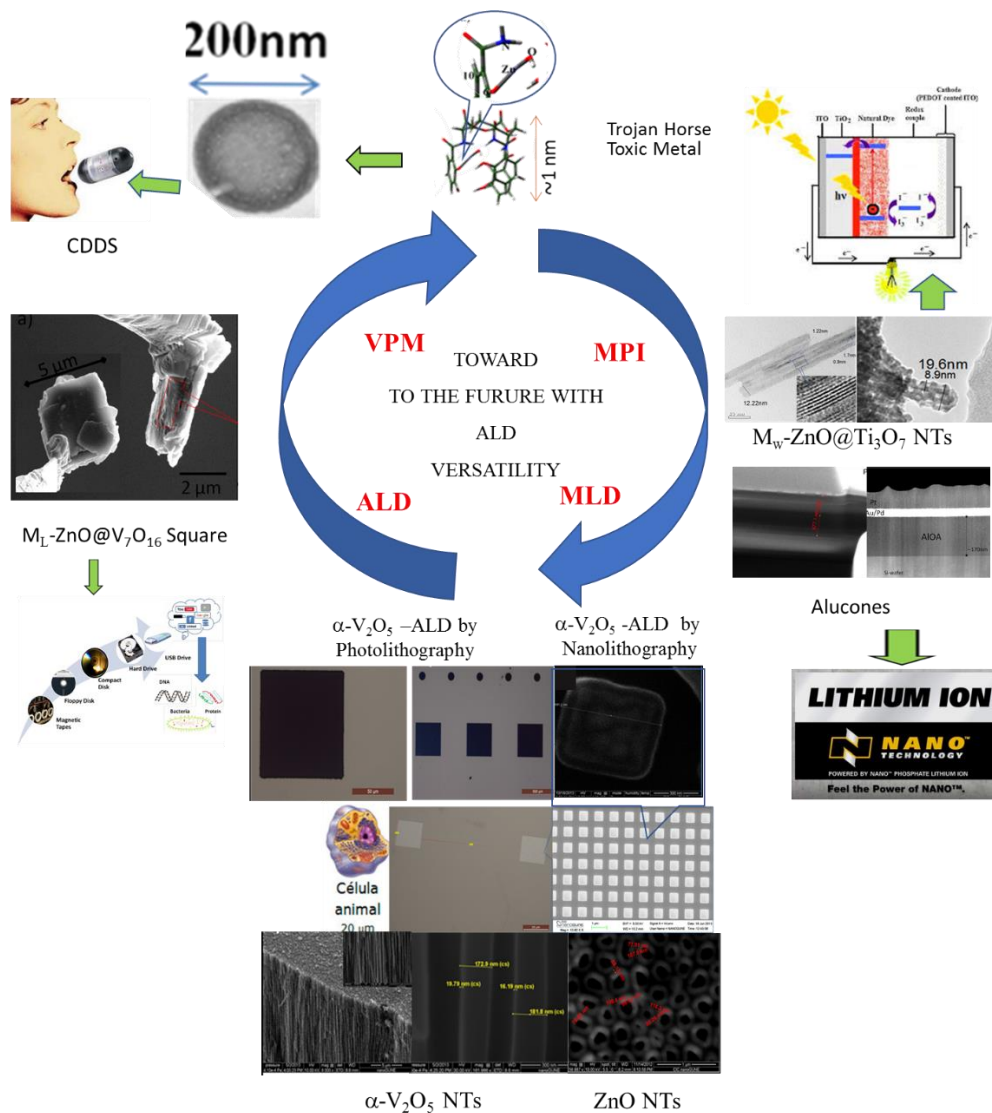
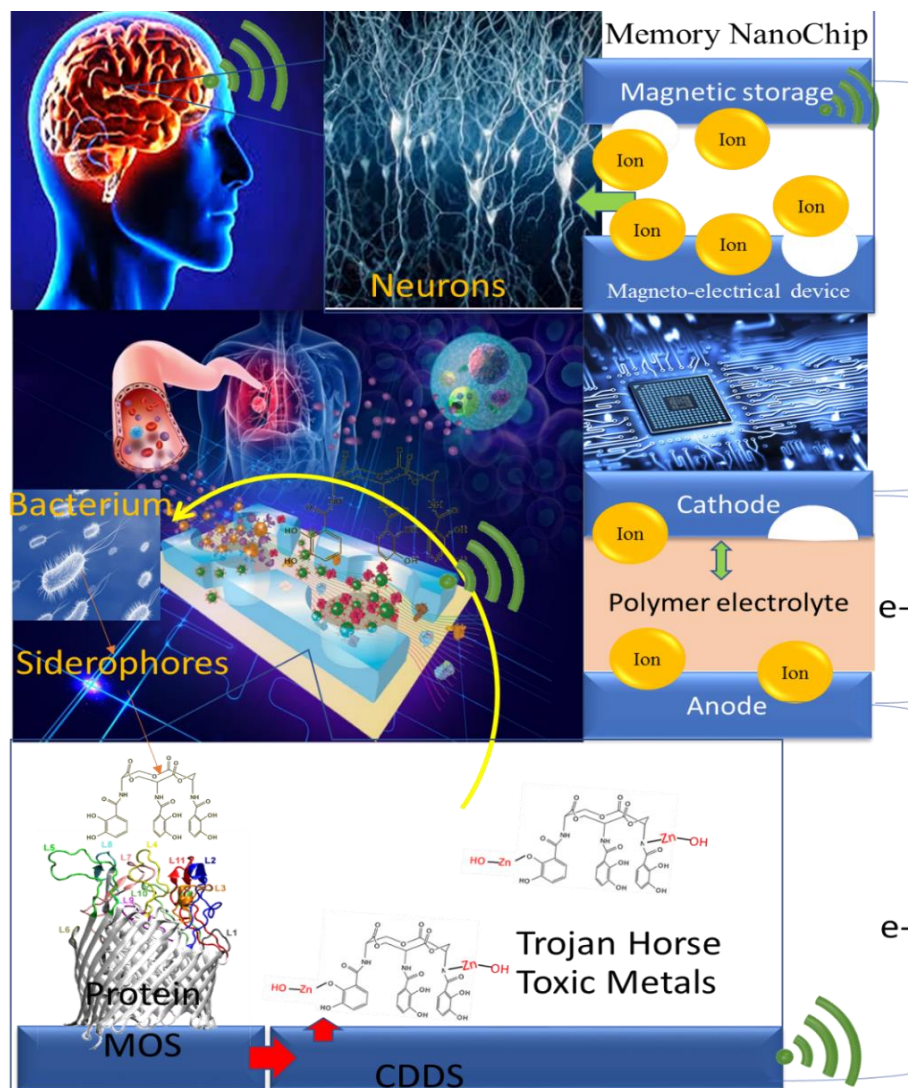


Figure 9.1. Future projections of the soft nanomaterials here modified and synthesized.



Lab-on-Chip & Control Drug Delivery

Figure 9.2. Prototype of Integrated Lab-on-Chip & Control Drug Delivery System (CCDS), the system includes; metal oxide semiconductor (MOS) like sensor, a nanobattery and memory nanochip, in addition integrated brain-memory devices with internet signal.

REFERENCES

- Alivisatos, A.P. 1996;** Alivisatos, A.P. 1996, "Semiconductor clusters, nanocrystals, and quantum dots", *Science*, vol. 271, no. 5251, pp. 933.
- Abergel, R.J., Warner, J.A., Shuh, D.K. & Raymond, K.N. 2006, "Enterobactin Protonation and Iron Release: Structural Characterization of the Salicylate Coordination Shift in Ferric Enterobactin1", *Journal of the American Chemical Society*, vol. 128, no. 27, pp. 8920-8931.
- Annamalai, R., Jin, B., Cao, Z., Newton, S.M. & Klebba, P.E. 2004, "Recognition of ferric catecholates by FepA", *Journal of Bacteriology*, vol. 186, no. 11, pp. 3578-3589.
- Badot, J., et al 2000;** Badot, J., Ribes, S., Yousfi, E., Vivier, V., Pereira-Ramos, J., Baffier, N. & Lincotb, D. 2000, "Atomic layer epitaxy of vanadium oxide thin films and electrochemical behavior in presence of lithium ions", *Electrochemical and Solid-State Letters*, vol. 3, no. 10, pp. 485-488.
- Bhatt, M.D. & O'Dwyer, C. 2015, "Recent progress in theoretical and computational investigations of Li-ion battery materials and electrolytes", *Physical Chemistry Chemical Physics*, vol. 17, no. 7, pp. 4799-4844.
- Bruce, P.G.,** Scrosati, B. & Tarascon, J. 2008, "Nanomaterials for rechargeable lithium batteries", *Angewandte Chemie International Edition*, vol. 47, no. 16, pp. 2930-2946.
- Buchanan, S.K.,** Smith, B.S., Venkatramani, L., Xia, D., Esser, L., Palnitkar, M., Chakraborty, R., van der Helm, D. & Deisenhofer, J. 1999, "Crystal structure of the outer membrane active transporter FepA from *Escherichia coli*", *Nature Structural & Molecular Biology*, vol. 6, no. 1, pp. 56-63.
- Carlino, S. 1997,** "The intercalation of carboxylic acids into layered double hydroxides: a critical evaluation and review of the different methods", *Solid State Ionics*, vol. 98, no. 1, pp. 73-84.

- Caretti, I et al 2012;** Caretti, I., Yuste, M., Torres, R., Sánchez, O., Jiménez, I. & Galindo, R.E. 2012, "Coordination chemistry of titanium and zinc in $Ti(1-x)Zn_{2x}O_2$ ($0 \leq x \leq 1$) ultrathin films grown by DC reactive magnetron sputtering", *RSC Advances*, vol. 2, no. 7, pp. 2696-2699.
- Cui, Z., et al 2017.** Nanofabrication Principles, Capabilities and Limits Second Edition, springer (ISBN 978-3-319-39359-9). Pp 11-30.
- Garcia-Garibay, M.A. 2007,** "Molecular Crystals on the Move: From Single-Crystal-to-Single-Crystal Photoreactions to Molecular Machinery", *Angewandte Chemie International Edition*, vol. 46, no. 47, pp. 8945-8947.
- Chakraborty, R.,** Lemke, E.A., Cao, Z., Klebba, P.E. & van der Helm, D. 2003, "Identification and mutational studies of conserved amino acids in the outer membrane receptor protein, FepA, which affect transport but not binding of ferric-enterobactin in *Escherichia coli*", *Biomaterials*, vol. 16, no. 4, pp. 507-518.
- Chandiran, A.K.,** Abdi-Jalebi, M., Nazeeruddin, M.K. & Grätzel, M. 2014, "Analysis of electron transfer properties of ZnO and TiO₂ photoanodes for dye-sensitized solar cells", *ACS nano*, vol. 8, no. 3, pp. 2261-2268.
- Chen, X.,** Sun, X. & Li, Y. 2002, "Self-assembling vanadium oxide nanotubes by organic molecular templates", *Inorganic chemistry*, vol. 41, no. 17, pp. 4524-4530.
- Chen X. et al 2007;** Chen, X. & Mao, S.S. 2007, "Titanium dioxide nanomaterials: synthesis, properties, modifications, and applications", *Chem.Rev*, vol. 107, no. 7, pp. 2891-2959.
- Dieing. T et al 2010,** Confocal Raman Microscopy, Springer. pp 11- 24.
- Donoso, D. & Mendizabal, F. 2011,** "Theoretical study of the interaction between Pt (0) and MPH₃ fragments in complexes of the $[Pt_3(\mu-CO)_3(PH_3)_3]-MPH_3$ (M= Cu , Au , Ag) type", *Theoretical Chemistry Accounts*, vol. 129, no. 3-5, pp. 381-387.
- Dorea, J.G.,** Marques, R.C. & Brandao, K.G. 2009, "Neonate exposure to thimerosal mercury from hepatitis B vaccines", *American Journal of Perinatology*, vol. 26, no. 7, pp. 523-527.
- Elam, J.W., et al 2008;** Elam, J.W., Baker, D.A., Hryn, A.J., Martinson, A.B., Pellin, M.J. & Hupp, J.T. 2008, "Atomic layer deposition of tin oxide films using tetrakis (dimethylamino)

- tin", *Journal of Vacuum Science & Technology A: Vacuum, Surfaces, and Films*, vol. 26, no. 2, pp. 244-252.
- Feist, T.P. & Davies, P.K.** 1992, "The soft chemical synthesis of TiO₂ (B) from layered titanates", *Journal of solid state chemistry*, vol. 101, no. 2, pp. 275-295.
- George S. M. et al 2007;** Du, Y. & George, S. 2007, "Molecular layer deposition of nylon 66 films examined using in situ FTIR spectroscopy", *The Journal of Physical Chemistry C*, vol. 111, no. 24, pp. 8509-8517.
- George, S.M et al 2008;** Dameron, A.A., Seghete, D., Burton, B., Davidson, S., Cavanagh, A., Bertrand, J. & George, S. 2008, "Molecular layer deposition of alucone polymer films using trimethylaluminum and ethylene glycol", *Chemistry of Materials*, vol. 20, no. 10, pp. 3315-3326
- George, S.M. 2009a;** George, S.M. 2009, "Atomic layer deposition: an overview", *Chemical reviews*, vol. 110, no. 1, pp. 111-131.
- George, S.M et al 2009b;** Burton, B., Fabreguette, F. & George, S. 2009, "Atomic layer deposition of MnO using Bis (ethylcyclopentadienyl) manganese and H₂O", *Thin Solid Films*, vol. 517, no. 19, pp. 5658-5665.
- George, S.M. 2009a;** George, S.M. 2009, "Atomic layer deposition: an overview", *Chemical reviews*, vol. 110, no. 1, pp. 111-131.
- George, S.M., et al 2013;** Liu, J., Yoon, B., Kuhlmann, E., Tian, M., Zhu, J., George, S.M., Lee, Y. & Yang, R. 2013, "Ultralow thermal conductivity of atomic/molecular layer-deposited hybrid organic-inorganic zinc oxide thin films", *Nano letters*, vol. 13, no. 11, pp. 5594-5599.
- Ghosh, M.K. & Choi, C.H.** 2006, "The initial mechanisms of Al₂O₃ atomic layer deposition on OH/Si (100)-2×1 surface by tri-methylaluminum and water", *Chemical physics letters*, vol. 426, no. 4, pp. 365-369.
- Garcia P. et al 2006;** García, P.D., Blanco, Á., Shavel, A., Gaponik, N., Eychmüller, A., Rodríguez-González, B., Liz-Marzán, L.M. & López, C. 2006, "Quantum dot thin layers templated on ZnO inverse opals", *Advanced Materials*, vol. 18, no. 20, pp. 2768-2772.

-
- Hohenberg, P. and Kohn, W. 1964.** Inhomogeneous Electron Gas. *Phys. Rev.* 136, B864.
- Iordanova R. et al 2011;** Iordanova, R., Bachvarova-Nedelcheva, A., Dimitriev, Y. & Iliev, T. 2011, "Mechanochemical synthesis and photocatalytic properties of zinc titanates", *Bulgarian Chemical Communications*, vol. 43, pp. 378-382.
- Jhonson R. W. et al 2014;** Johnson, R. W., Hultqvist, A. & Bent, S.F. 2014, "A brief review of atomic layer deposition: from fundamentals to applications", *Materials today*, vol. 17, no. 5, pp. 236-246.
- Jhonson R. W. et al 2014;** Johnson, R. W., Hultqvist, A. & Bent, S.F. 2014, "A brief review of atomic layer deposition: from fundamentals to applications", *Materials today*, vol. 17, no. 5, pp. 236-246.
- Harrington, M.J.,** Masic, A., Holten-Andersen, N., Waite, J.H. & Fratzl, P. 2010, "Iron-clad fibers: a metal-based biological strategy for hard flexible coatings", *Science (New York, N.Y.)*, vol. 328, no. 5975, pp. 216-220.
- Harris, W.R.,** Carrano, C.J., Cooper, S.R., Sofen, S.R., Avdeef, A.E., McArdle, J.V. & Raymond, K.N. 1979, "Coordination chemistry of microbial iron transport compounds. 19. Stability constants and electrochemical behavior of ferric enterobactin and model complexes", *Journal of the American Chemical Society*, vol. 101, no. 20, pp. 6097-6104.
- Hernández, S., Cauda, V.,** Chiodoni, A., Dallorto, S., Sacco, A., Hidalgo, D., Celasco, E. & Pirri, C.F. 2014, "Optimization of 1D ZnO@ TiO₂ core-shell nanostructures for enhanced photoelectrochemical water splitting under solar light illumination", *ACS applied materials & interfaces*, vol. 6, no. 15, pp. 12153-12167.
- Jones, R., Angell, C., Ito, T. & Smith, R. 1959, "The carbonyl stretching bands in the infrared spectra of unsaturated lactones", *Canadian Journal of Chemistry*, vol. 37, no. 12, pp. 2007-2022.
- Klabunde, T., Eicken, C., Sacchetti, J.C. & Krebs, B. 1998, "Crystal structure of a plant catechol oxidase containing a dicopper center", *Nature Structural & Molecular Biology*, vol. 5, no. 12, pp. 1084-1090.

- Korolik, E., Zhabankov, R., Ivanov, A., Il'ich, G., Insarova, N. & Leshchenko, V. 1998, "A study of the molecular structure of DL-serine with the method of low-temperature IR spectroscopy", *Journal of applied spectroscopy*, vol. 65, no. 6, pp. 906-910.
- Krusin-Elbaum, L., News, D., Zeng, H., Derycke, V., Sun, J. & Sandstrom, R. 2004, "Room-temperature ferromagnetic nanotubes controlled by electron or hole doping", *Nature*, vol. 431, no. 7009, pp. 672-676.
- Karppinen, M. 2014;** Tynell, T. & Karppinen, M. 2014, "Atomic layer deposition of ZnO: a review", *Semiconductor Science and Technology*, vol. 29, no. 4, pp. 043001.
- Knez, M. 2011;** Lee, S., Pippel, E. & Knez, M. 2011, "Metal infiltration into biomaterials by ALD and CVD: A comparative study", *ChemPhysChem*, vol. 12, no. 4, pp. 791-798.
- Knez, M. et al 2009a;** Lee, S.M., Pippel, E., Gosele, U., Dresbach, C., Qin, Y., Chandran, C.V., Brauniger, T., Hause, G. & Knez, M. 2009, "Greatly increased toughness of infiltrated spider silk", *Science (New York, N.Y.)*, vol. 324, no. 5926, pp. 488-492.
- Knez, M. et al 2009b;** Zhang, L., Patil, A.J., Li, L., Schierhorn, A., Mann, S., Gösele, U. & Knez, M. 2009, "Chemical infiltration during atomic layer deposition: metalation of porphyrins as model substrates", *Angewandte Chemie International Edition*, vol. 48, no. 27, pp. 4982-4985.
- Knez, M. et al 2010;** Lee, S., Pippel, E., Moutanabbir, O., Gunkel, I., Thurn-Albrecht, T. & Knez, M. 2010, "Improved mechanical stability of dried collagen membrane after metal infiltration", *ACS applied materials & interfaces*, vol. 2, no. 8, pp. 2436-2441.
- Knez, M. et al 2011;** Lee, S., Pippel, E. & Knez, M. 2011, "Metal infiltration into biomaterials by ALD and CVD: A comparative study", *ChemPhysChem*, vol. 12, no. 4, pp. 791-798.
- Knez, M., et al. 2015;** Gregorczyk, K.E., Pickup, D.F., Sanz, M.G., Irakulis, I.A., Rogero, C. & Knez, M. 2014, "Tuning the tensile strength of cellulose through vapor-phase metalation", *Chemistry of Materials*, vol. 27, no. 1, pp. 181-188.
- Karppinen M. et al 2014;** Sundberg, P. & Karppinen, M. 2014, "Organic and inorganic–organic thin film structures by molecular layer deposition: A review", *Beilstein journal of nanotechnology*, vol. 5, no. 1, pp. 1104-1136.

-
- Karppinen, M. 2014;** Tynell, T. & Karppinen, M. 2014, "Atomic layer deposition of ZnO: a review", *Semiconductor Science and Technology*, vol. 29, no. 4, pp. 043001.
- Kim, H., et al. 2009;** Kim, H. & Maeng, W. 2009, "Applications of atomic layer deposition to nanofabrication and emerging nanodevices", *Thin Solid Films*, vol. 517, no. 8, pp. 2563-2580.
- Klepper, K.B., et al 2010;** Klepper, K.B., Nilsen, O. & Fjellvåg, H. 2010, "Deposition of thin films of organic-inorganic hybrid materials based on aromatic carboxylic acids by atomic layer deposition", *Dalton Transactions*, vol. 39, no. 48, pp. 11628-11635.
- Kim, H. et al 2009;** Kim, H. & Maeng, W. 2009, "Applications of atomic layer deposition to nanofabrication and emerging nanodevices", *Thin Solid Films*, vol. 517, no. 8, pp. 2563-2580.
- Krusin-Elbaum, L. et al 2004;** Krusin-Elbaum, L., News, D., Zeng, H. & Derycke, V. 2004, "Room-temperature ferromagnetic nanotubes controlled by electron or hole doping", *Nature*, vol. 431, no. 7009, pp. 672.
- Kohn and L.J. Sham.1965.** Self-Consistent Equations Including Exchange and Correlation Effects, 1965, *Phys. Rev.* 140, A1133.
- Lavayen, V et al 2007:** Lavayen, V., Mirabal, N., O'Dwyer, C., Santa Ana, M.A., Benavente, E., Torres, C.S. & Gonzalez, G. 2007, "The formation of nanotubes and nanocoils of molybdenum disulphide", *Applied Surface Science*, vol. 253, no. 12, pp. 5185-5190.
- Le Bail et al 1992:** Le Bail, A. & Fourquet, J. 1992, "Crystal structure and thermal behaviour of H₂Ti₃O₇: A new defective ramsdellite form from Li H exchange on Li₂Ti₃O₇", *Materials Research Bulletin*, vol. 27, no. 1, pp. 75-85.
- López-Cabaña, Z. et al 2011;** López-Cabaña, Z., Torres, C.M.S. & González, G. 2011, "Semiconducting properties of layered cadmium sulphide-based hybrid nanocomposites", *Nanoscale research letters*, vol. 6, no. 1, pp. 523.

- Lavayen, V et al 2007; Lavayen, V.**, Mirabal, N., O'Dwyer, C., Santa Ana, M.A., Benavente, E., Torres, C.S. & Gonzalez, G. 2007, "The formation of nanotubes and nanocoils of molybdenum disulphide", *Applied Surface Science*, vol. 253, no. 12, pp. 5185-5190.
- Levine. I. 2004.** Quantum Chemistry, Prentice Hall, pp.583.
- Lane, N. & Martin, W.F.** 2012, "The origin of membrane bioenergetics", *Cell*, vol. 151, no. 7, pp. 1406-1416.
- Li, Y., Zhang, H. & Liu, Q.** 2012, "FT-IR spectroscopy and DFT calculation study on the solvent effects of benzaldehyde in organic solvents", *Spectrochimica Acta Part A: Molecular and Biomolecular Spectroscopy*, vol. 86, pp. 51-55.
- Liu, J., Li, X., Wang, Z., Guo, H., Peng, W., Zhang, Y. & Hu, Q.** 2010, "Preparation and characterization of lithium hexafluorophosphate for lithium-ion battery electrolyte", *Transactions of Nonferrous Metals Society of China*, vol. 20, no. 2, pp. 344-348.
- Llinas, M., Wilson, D. & Neilands, J.** 1973, "Effect of metal binding on the conformation of enterobactin. Proton and carbon-13 nuclear magnetic resonance study", *Biochemistry*, vol. 12, no. 20, pp. 3836-3843.
- Mondloch, J.E., et al 2013; Mondloch, J.E., Bury, W., Fairen-Jimenez, D., Kwon, S., DeMarco, E.J., Weston, M.H., Sarjeant, A.A., Nguyen, S.T., Stair, P.C. & Snurr, R.Q.** 2013, "Vapor-phase metalation by atomic layer deposition in a metal-organic framework", *Journal of the American Chemical Society*, vol. 135, no. 28, pp. 10294-10297.
- Moreno, M., Santa Ana, M.A., Gonzalez, G. & Benavente, E.** 2010, "Poly (acrylonitrile)-montmorillonite nanocomposites: effects of the intercalation of the filler on the conductivity of composite polymer electrolytes", *Electrochimica Acta*, vol. 55, no. 4, pp. 1323-1327.
- Moreno, M., Quijada, R., Santa Ana, M.A., Benavente, E., Gomez-Romero, P. & González, G.** 2011, "Electrical and mechanical properties of poly (ethylene oxide)/intercalated clay polymer electrolyte", *Electrochimica Acta*, vol. 58, pp. 112-118.
- Mohammad, M., et al 2012** Chapter 2. Fundamentals of Electron Beam Exposure and Development, Nanofabrication Techniques and Principles. Springer-Verlag/Wien. Pp 11-38.

- Munk, B.H.** & Schlegel, H.B. 2006, "Molecular orbital studies of zinc oxide chemical vapor deposition: Gas-phase radical reactions", *Chemistry of materials*, vol. 18, no. 7, pp. 1878-1884.
- Muth J. F. et al 1999**; Muth, J., Kolbas, R., Sharma, A., Oktyabrsky, S. & Narayan, J. 1999, "Excitonic structure and absorption coefficient measurements of ZnO single crystal epitaxial films deposited by pulsed laser deposition", *Journal of Applied Physics*, vol. 85, no. 11, pp. 7884-7887.
- Macek, B., Gnad, F., Soufi, B., Kumar, C., Olsen, J.V., Mijakovic, I. & Mann, M. 2008, "Phosphoproteome analysis of E. coli reveals evolutionary conservation of bacterial Ser/Thr/Tyr phosphorylation", *Molecular & cellular proteomics : MCP*, vol. 7, no. 2, pp. 299-307.
- Mariscal, A. et al 1995**; Mariscal, A., García, A., Carnero, M., Gómez, J., Pinedo, A. & Fernández-Crehuet, J. 1995, "Evaluation of the toxicity of several heavy metals by a fluorescent bacterial bioassay", *Journal of Applied Toxicology*, vol. 15, no. 2, pp. 103-107.
- Markova-Velichkova, M. et al 2011**: Dimitriev, Y., Iordanova, R. & Markova-Velichkova, M. 2011, "MECHANOCHEMICAL ACTIVATION OF COMPOSITIONS 95ZnO-5M", *Journal of the University of Chemical Technology and Metallurgy*, vol. 46, no. 3, pp. 249-254.
- Mendizabal, F., et al 2011**; Mendizabal, F., Donoso., D. 2011. Theoretical study of the interaction between Pt(0) and MPH₃ + fragments in complexes of the [Pt₃ (I-CO)₃(PH₃)₃]-MPH₃ + (M 5 Cu⁺, Au⁺, Ag⁺) type. *Theor Chem Acc.* 129:381–387
- Morris, Jr., J. W. "Defects in Crystals." Chapter 4 in *Materials Science and Engineering: An Introduction*. Wiley, 2013, pp. 76–107. ISBN: 9781118324578
- Nilsen, O.**, Foss, S., Fjellvåg, H. & Kjekshus, A. 2004, "Effect of substrate on the characteristics of manganese (IV) oxide thin films prepared by atomic layer deposition", *Thin Solid Films*, vol. 468, no. 1, pp. 65-74.
- Nisula, M.** & Karppinen, M. 2016, "Atomic/Molecular Layer Deposition of Lithium Terephthalate Thin Films as High Rate Capability Li-Ion Battery Anodes", *Nano letters*, vol. 16, no. 2, pp. 1276-1281.

- Nikam L. et al 2015;** Nikam, L., Panmand, R., Kadam, S., Naik, S. & Kale, B. 2015, "Enhanced hydrogen production under a visible light source and dye degradation under natural sunlight using nanostructured doped zinc orthotitanates", *New Journal of Chemistry*, vol. 39, no. 5, pp. 3821-3834.
- O'Sullivan, B., Doble, D.M., Thompson, M.K., Siering, C., Xu, J., Botta, M., Aime, S. & Raymond, K.N. 2003, "The effect of ligand scaffold size on the stability of tripodal hydroxypyridonate gadolinium complexes", *Inorganic chemistry*, vol. 42, no. 8, pp. 2577-2583.
- Pan, E.,** Zhang, X., Huang, Z., Krezel, A., Zhao, M., Tinberg, C.E., Lippard, S.J. & McNamara, J.O. 2011, "Vesicular zinc promotes presynaptic and inhibits postsynaptic long-term potentiation of mossy fiber-CA3 synapse", *Neuron*, vol. 71, no. 6, pp. 1116-1126.
- Patra, M.,** Manzoor, K., Manoth, M., Negi, S., Vadera, S. & Kumar, N. 2008, "Nanotechnology applications for chemical and biological sensors", *Defence Science Journal*, vol. 58, no. 5, pp. 636.
- Pankewitz, T.,** Lagutschenkov, A., Niedner-Schatteburg, G., Xantheas, S.S. & Lee, Y. 2007, "Infrared spectrum of NH₄ (H₂O): Evidence for mode specific fragmentation", *The Journal of chemical physics*, vol. 126, no. 7, pp. 074307.
- Phillips, J.C.,** Braun, R., Wang, W., Gumbart, J., Tajkhorshid, E., Villa, E., Chipot, C., Skeel, R.D., Kale, L. & Schulten, K. 2005, "Scalable molecular dynamics with NAMD", *Journal of computational chemistry*, vol. 26, no. 16, pp. 1781-1802.
- Pearson. R.P. 1963.** Hard and Soft Acids and Bases, *J. Am. Chem. Soc.*, Vol. 85, N°22, pp 3533–3539
- Putkonen, M.,** Harjuoja, J., Sajavaara, T. & Niinistö, L. 2007, "Atomic layer deposition of polyimide thin films", *Journal of Materials Chemistry*, vol. 17, no. 7, pp. 664-669.
- Puurunen, R.L. 2005:** Puurunen, R.L. 2005, "Surface chemistry of atomic layer deposition: A case study for the trimethylaluminum/water process", *Journal of Applied Physics*, vol. 97, no. 12, pp. 9.
- Tynell, T. &** Karppinen, M. 2014, "Atomic layer deposition of ZnO: a review", *Semiconductor Science and Technology*, vol. 29, no. 4, pp. 043001.

-
- Torrent-Sucarrat, M. et al 2010;** Torrent-Sucarrat, M., De Proft, F., Ayers, P. & Geerlings, P. 2010, "On the applicability of local softness and hardness", *Physical Chemistry Chemical Physics*, vol. 12, no. 5, pp. 1072-1080.
- Reyntjens, S. & Puers, R. 2001,** "A review of focused ion beam applications in microsystem technology", *Journal of Micromechanics and Microengineering*, vol. 11, no. 4, pp. 287.
- Raymond, K.N., et al. 2010;** Hocking, R.K., DeBeer George, S., Raymond, K.N., Hodgson, K.O., Hedman, B. & Solomon, E.I. 2010, "Fe L-edge x-ray absorption spectroscopy determination of differential orbital covalency of siderophore model compounds: electronic structure contributions to high stability constants", *Journal of the American Chemical Society*, vol. 132, no. 11, pp. 4006-4015.
- Rasmussen, R.S. & Brattain, R.R. 1949,** "Infrared spectra of some carboxylic acid derivatives", *Journal of the American Chemical Society*, vol. 71, no. 3, pp. 1073-1079.
- Raymond, K.N., Dertz, E.A. & Kim, S.S. 2003,** "Enterobactin: an archetype for microbial iron transport", *Proceedings of the National Academy of Sciences of the United States of America*, vol. 100, no. 7, pp. 3584-3588.
- Raveendra, RS et al 2014;** Raveendra, R., Prashanth, P., Krishna, R.H., Bhagya, N., Nagabhushana, B., Naika, H.R., Lingaraju, K., Nagabhushana, H. & Prasad, B.D. 2014, "Synthesis, structural characterization of nano ZnTiO₃ ceramic: An effective azo dye adsorbent and antibacterial agent", *Journal of Asian Ceramic Societies*, vol. 2, no. 4, pp. 357-365.
- Skoog, D. A. et al 2007.** Principles of Instrumental Analysis, Sixth Edition, Thomson-BrookScole. Pp,560, 470, 483, 613.
- Suntola T, et al. 1977;** Suntola, T. & Antson, J. 1977, *Method for producing compound thin films*, U.S. Patent No. 4,058,430. 5 November 1977
- Segovia, M., Lemus, K., Moreno, M., Santa Ana, M., Gonzalez, G., Ballesteros, B., Sotomayor, C. & Benavente, E. 2011,** "Zinc oxide/carboxylic acid lamellar structures", *Materials Research Bulletin*, vol. 46, no. 11, pp. 2191-2195.

-
- Samarth, N. 2007**, "Ferromagnetic semiconductors: Ruled by a magnetic-rich minority", *Nature materials*, vol. 6, no. 6, pp. 403-404.
- Schreckenbach, G., Ruiz-Morales, Y. & Ziegler, T. 1996, "The calculation of ^{77}Se chemical shifts using gauge including atomic orbitals and density functional theory", *The Journal of chemical physics*, vol. 104, no. 21, pp. 8605-8612.
- Seymour, J.P., Wu, F., Wise, K.D. & Yoon, E. 2017, "State-of-the-art MEMS and microsystem tools for brain research", *Microsystems & Nanoengineering*, vol. 3, pp. 16066.
- Shanzer, A.**, Libman, J., Lifson, S. & Felder, C.E. 1986, "Origin of the iron (III) binding and conformational properties of enterobactin", *Journal of the American Chemical Society*, vol. 108, no. 24, pp. 7609-7619.
- Śledź, M., Janczak, J. & Kubiak, R. 2001, "New crystalline modification of terephthalic acid", *Journal of Molecular Structure*, vol. 595, no. 1, pp. 77-82.
- Stephan, A.M. & Nahm, K. 2006**, "Review on composite polymer electrolytes for lithium batteries", *Polymer*, vol. 47, no. 16, pp. 5952-5964.
- Stephens, D.L., Choe, M.D. & Earhart, C.F. 1995**, "Escherichia coli periplasmic protein FepB binds ferrienterobactin", *Microbiology*, vol. 141, no. 7, pp. 1647-1654.
- Sipos, B.**, Duchamp, M., Magrez, A., Forró, L., Barišić, N., Kis, A., Seo, J.W., Bieri, F., Krumeich, F. & Nesper, R. 2009, "Mechanical and electronic properties of vanadium oxide nanotubes", *Journal of Applied Physics*, vol. 105, no. 7, pp. 074317.
- Schwarz, H.A. 1980**, "Gas phase infrared spectra of ammoniated ammonium ions", *The Journal of chemical physics*, vol. 72, no. 1, pp. 284-287.
- Song Xuchun et al 2007; Song, X.**, Yang, E. & Zheng, Y. 2007, "Synthesis of $\text{M}_x\text{H}_y\text{Ti}_3\text{O}_7$ nanotubes by simple ion-exchanged process and their adsorption property", *Chinese Science Bulletin*, vol. 52, no. 18, pp. 2491-2495.

-
- Chen, Q. et al 2002;** Chen, Q., Zhou, W., Du, G. & Peng, L. 2002, "Trititanate nanotubes made via a single alkali treatment", *Advanced Materials*, vol. 14, no. 17, pp. 1208-1211.
- Tasaki, K.,** Kanda, K., Nakamura, S. & Ue, M. 2003, "Decomposition of LiPF₆ and Stability of PF₅ in Li-Ion Battery Electrolytes Density Functional Theory and Molecular Dynamics Studies", *Journal of the Electrochemical Society*, vol. 150, no. 12, pp. A1628-A1636.
- Thomas, J. 2003,** "Lithium batteries: A spectacularly reactive cathode", *Nature materials*, vol. 2, no. 11, pp. 705-706.
- Tripathi, G. & Sheng, S. 1979,** "Solid-state vibrational spectra and structures of terephthalic acid and the terephthalate ion", *Journal of Molecular Structure*, vol. 57, pp. 21-34.
- Tynell, T. & Karppinen, M. 2014,** "Atomic layer deposition of ZnO: a review", *Semiconductor Science and Technology*, vol. 29, no. 4, pp. 043001.
- Ushakumari, L.,** Varghese, H.T., Panicker, C.Y., Ertan, T. & Yildiz, I. 2008, "Vibrational spectroscopic studies and DFT calculations of 4-fluoro-N-(2-hydroxy-4-nitrophenyl) benzamide", *Journal of Raman Spectroscopy*, vol. 39, no. 12, pp. 1832-1839.
- Verma. H. R. et al. 2007.** Atomic and Nuclear Analytical Methods: XRF, Mössbauer, XPS, NAA and Ion-Beam Spectroscopic Techniques. pp-214-217.
- Vance, M.E et al 2015;** Vance, M.E., Kuiken, T., Vejerano, E.P., McGinnis, S.P., Hochella Jr, M.F., Rejeski, D. & Hull, M.S. 2015, "Nanotechnology in the real world: Redeveloping the nanomaterial consumer products inventory", *Beilstein journal of nanotechnology*, vol. 6, no. 1, pp. 1769-1780.
- Van Bui, H., et al 2017;** Van Bui, H., Grillo, F. & van Ommen, J. 2017, "Atomic and molecular layer deposition: off the beaten track", *Chemical Communications*, vol. 53, no. 1, pp. 45-71
- Vasquez, J et al. 2009;** Vasquez, J., Lozano, H., Lavayen, V., Lira-Cantú, M., Gómez-Romero, P., Santa Ana, M.A., Benavente, E. & Gonzalez, G. 2009, "High-yield preparation of titanium

-
- dioxide nanostructures by hydrothermal conditions", *Journal of nanoscience and nanotechnology*, vol. 9, no. 2, pp. 1103-1107.
- Wang, X, et al 2015;** Wang, X. & Yushin, G. 2015, "Chemical vapor deposition and atomic layer deposition for advanced lithium ion batteries and supercapacitors", *Energy & Environmental Science*, vol. 8, no. 7, pp. 1889-1904.
- Wachnicki L et al 2010;** Krajewski, T., Łuka, G., Witkowski, B., Kowalski, B., Kopalko, K., Domagala, J., Guziewicz, M., Godlewski, M. & Guziewicz, E. 2010, "Monocrystalline zinc oxide films grown by atomic layer deposition", *Thin Solid Films*, vol. 518, no. 16, pp. 4556-4559.
- Wei. A 2012;** Wei. A 2012 EC-2012
- Williams. D. B. et al 2010.** Transmission Electron Microscopy: A Textbook for Materials Science. Springer. pp 7,56.
- Workman. J. et al 2007.** Practical guide to interpretive near-infrared spectroscopy. CRC press. pp 2-13.
- Waseda. Y. et al 2011,** X-Ray Diffraction Crystallography: Introduction, Examples and Solved Problems, Springer. pp.74
- Wang, X. & Yushin, G. 2015,** "Chemical vapor deposition and atomic layer deposition for advanced lithium ion batteries and supercapacitors", *Energy & Environmental Science*, vol. 8, no. 7, pp. 1889-1904.
- Weingarten, C.P., Doraiswamy, P.M. & Fisher, M.P. 2016,** "A New Spin on Neural Processing: Quantum Cognition", *Frontiers in human neuroscience*, vol. 10, pp. 541.
- Williams, V.O., Jeong, N.C., Prasittichai, C., Farha, O.K., Pellin, M.J. & Hupp, J.T. 2012,** "Fast transporting ZnO–TiO₂ coaxial photoanodes for dye-sensitized solar cells based on ALD-modified SiO₂ aerogel frameworks", *ACS nano*, vol. 6, no. 7, pp. 6185-6196.

-
- Wieser, M.E., Holden, N., Coplen, T.B., Böhlke, J.K., Berglund, M., Brand, W.A., De Bièvre, P., Gröning, M., Loss, R.D. & Meija, J.** 2013, "Atomic weights of the elements 2011 (IUPAC Technical Report)", *Pure and Applied Chemistry*, vol. 85, no. 5, pp. 1047-1078.
- Wilson, H.W.** 1974, "The vapor phase infrared spectra of hydroquinone, pyrocatechol, and resorcinol", *Spectrochimica Acta Part A: Molecular Spectroscopy*, vol. 30, no. 12, pp. 2141-2152.
- Workman Jr, J. & Weyer, L.** 2007, *Practical guide to interpretive near-infrared spectroscopy*, CRC press.
- Yang, W. & Parr, R.G.** 1985, "Hardness, softness, and the Fukui function in the electronic theory of metals and catalysis", *Proceedings of the National Academy of Sciences of the United States of America*, vol. 82, no. 20, pp. 6723-6726.
- Yu. Y. et al 2014;** Yu, Y., Yin, X., Kvit, A. & Wang, X. 2014, "Evolution of hollow TiO₂ nanostructures via the Kirkendall effect driven by cation exchange with enhanced photoelectrochemical performance", *Nano letters*, vol. 14, no. 5, pp. 2528-2535.
- Zhang, L., Patil, A.J., Li, L., Schierhorn, A., Mann, S., Gösele, U. & Knez, M. 2009, "Chemical infiltration during atomic layer deposition: metalation of porphyrins as model substrates", *Angewandte Chemie International Edition*, vol. 48, no. 27, pp. 4982-4985.
- Zhang, S.S.** 2006, "A review on electrolyte additives for lithium-ion batteries", *Journal of Power Sources*, vol. 162, no. 2, pp. 1379-1394.
- Zhang, Y et al 2015; Zhang, Y.,** Jiang, Z., Huang, J., Lim, L.Y., Li, W., Deng, J., Gong, D., Tang, Y., Lai, Y. & Chen, Z. 2015, "Titanate and titania nanostructured materials for environmental and energy applications: a review", *RSC Advances*, vol. 5, no. 97, pp. 79479-79510.

References classified by chapters and sections.**References of Chapter IV**

- Adamo C. et al. 1998. *J. Chem. Phys.*, 108, 664
Best R. B. et al. 2012. *J. Chem Theory Comput.* 8: 3257.
Buchanan, S. K. et al. 1999. *Nature Structural & Molecular Biology*, 6, 1, 56.
Ditchfield R. et al. 1971. *J. Chem. Phys.*, 54, 724.
Humphrey W. et al. 1996. VDM: Visual molecular dynamics. *J Mol Graph.* 14; 33.
Fiser A. et al 2001. A. Comparative protein structure modeling with Modeller: A practical approach, 1.
Frisch. M. J. et al.2010. Gaussian 09, Rev. C.01.
Gaussian 09, Rev. C.01, M. J. Frisch, et al., Wallingford CT, 2010.
Glide, version 5.8, Schrödinger, LLC, New York, NY, 2012
Philips J.C. et a. 2005. *J Comput Chem.* 26. 1781.
Perdew J. P. et al. 1992. *Phys. Rev. B*, 46, 6671.
Perdew J. P. et al. 1996. *Phys. Rev. Lett.* 77, 3865.
Perdew J. P. et al. 1997. *Phys. Rev. Lett.* 78, 1396.
Weigend F. et al. 2005. *Phys. Chem. Chem. Phys.* 7, 3297.
Svensson, P. H. et al. 2003. *Chemical Reviews.* 103, 5, 1651
John. F. M. et al. 1992. *Handbook of Photoelectron Spectroscopy* Perkin Elmer; Minnesota, 1992.
Vásquez, J. et al 2010, *Electrochim. Acta*, 55, 4, 1373

References of Section 5.1 and 5.2

- Adamo C. et al. 1998. *J. Chem. Phys.*, 108, 664
Best R. B. et al. 2012. *J. Chem Theory Comput.* 8: 3257.
Buchanan, S. K. et al. 1999. *Nature Structural & Molecular Biology*, 6, 1, 56.
Ditchfield R. et al. 1971. *J. Chem. Phys.*, 54, 724.
Humphrey W. et al. 1996. VDM: Visual molecular dynamics. *J Mol Graph.* 14; 33.
Fiser A. et al 2001. A. Comparative protein structure modeling with Modeller: A practical approach, 1.
Frisch. M. J. et al.2010. Gaussian 09, Rev. C.01.
Gaussian 09, Rev. C.01, M. J. Frisch, et al., Wallingford CT, 2010.
Glide, version 5.8, Schrödinger, LLC, New York, NY, 2012
Philips J.C. et a. 2005. *J Comput Chem.* 26. 1781.
Perdew J. P. et al. 1992. *Phys. Rev. B*, 46, 6671.
Perdew J. P. et al. 1996. *Phys. Rev. Lett.* 77, 3865.
Perdew J. P. et al. 1997. *Phys. Rev. Lett.* 78, 1396.
Weigend F. et al. 2005. *Phys. Chem. Chem. Phys.* 7, 3297.
Chakraborty R. et al. 2003. *Biometals* 16, 4, 507.
Harris W. R. et al, 1979. *J. Am. Chem. Soc* 101, 20, 6097.
Klabunde T. et al.1998. *Nature Structural & Molecular Biology* 5, 12, 1084.
Fratzl, P. et al. 2010. *Science* 328, 5975, 216.
Raymond K. N. et al. 2006. *J. Am. Chem. Soc.* 128, 8920.
Raymond K. N. et al 1983. *J. Am. Chem. Soc.* 105, 4623.
Raymond K. N. et al. 2003. *Inorg. Chem.* 42, 8, 2577-2583.
Raymond K. N. et al. 2003. *PNAS*, 100, 3584-3588.
Raymond K. N. et al. 2010. *J. Am. Chem. Soc.* 132, 11, 4006.
Annamalai R. et al. 2004. *J. Bacteriol.* 186, 11, 3578.

- Buchanan S.K. et al. 1999. *Nature Structural & Molecular Biology*, 6, 1, 56.
- Dorea. J.G. et al. 2009. *Am.J. Perinatol.* 26, 7, 523.
- Jones et al. R. N. 1959. *Canadian Journal of Chemistry* 37, 12, 2007.
- Korolik et al. E. V. 1998. *Journal of applied spectroscopy* 65, 6, 906.
- Llinás M. et al. 1973. *Biochemistry* 12, 3836-3843.
- Li, Y. et al. 2012. *Spectrochimica Acta Part A.* 86, 51-55.
- Mariscal. A. et al. 1995. *J. Applied Toxicology*, 15, 103.
- Macek B. et al. 2008. *Mol. Cell. Proteomics*, 7, 2, 299-307.
- Rasmussen R. S. et al. 1949. *J. Am. Chem. Soc.* 71, 3, 1073.
- Stephens D. L. et al. 1995. *Microbiology*, 141, 1647.
- Shanzer et al A. 1986. *J. Am. Chem. Soc.* 108, 24, 7609-7619.
- Ushakumari L. et al 2008. *J. Raman Spectrosc.* 39, 12, 1832-1839.
- Wilson H. W. et al. 1974. *Spectrochimica Acta. Part A*, 30A, 2141.
- Wikel P. A. et al. 1976. *Inorg. Chem* 15, 396.
- Workman J. et al. 2007. *Practical guide to interpretive near-infrared spectroscopy*, CRC press. (pp 71).
- Wieser M. E. et al. 2013. *Pure and Applied Chemistry* 85, 5, 1047.
- Abergel R. J. et al. 2006. *J. Am. Chem. Soc.* 128, 27, 8920.
- Philips J.C. et al. 2005. *J. Comput Chem.* 26. 1781.
- Schreckenbach G. et al. 1996. *J.Chem.Phys.* 104, 21, 8605.
- Schatzman. J.C et al. 1996. *Journal on Scientific Computing*, 17, 5, 1150-1166, (from <http://www.originlab.com/doc/Origin-Help/Deconv-Ref>).
- Schreckenbach G. et al. 1998. *Theoretical Chemistry Accounts*, 99, 2, 71.
- World Health Organization, Department of Reproductive Health and Research, 2011. WHO/RHR/11.14.
- World Health Organization, Department of Tuberculosis, Global tuberculosis report 2014. WHO/HTM/TB/2014.0

References of section 5.3

- Wachnicki. L et al 2010. *Thin Solid Films* 518, 4556.
- Morris, Jr., J. W. "Defects in Crystals." Chapter 4 in *Materials Science and Engineering: An Introduction*. Wiley, 2013, pp. 76–107. ISBN: 9781118324578.
- Nesper, R. et al 2002. *Z. anorg. Chem.* 628, 12, 2778.
- Zavalij, P. Y. et al 1999. *Acta Crystallographica Section B: Structural Science.* 55, 5, 627.
- Wang, X. et al 1998. *J. chem com.* 9, 1009.
- Nesper, R. et al 2002. *Z. anorg. Chem.* 628, 12, 2778.
- Schwarz, H. A. et al 1980. *J. Chem. Phys.* 1980, 72: 284.
- Pankewitz, T. et al 2007. *J. Chem. Phys.* 2007, 127, 074307.
- Chen, X. et al 2002. *Inorg. Chem.* 41, 4524.
- O'Dwyer, C. et al 2009. *Adv. Funct. Mater.* 2009, 19, 1.
- Cui, H-H. et al 2008. *Thin Solid Films.* 516, 1484.
- Raj, D. A. Curr. et al 2010. *Appl. Phys.* 10, 531.
- Souza-Filho. AG et al 2004. *Nano Letters.* 4, 11, 2099.
- Twu J et al. 1997. *Mater. Chem.* 7, 11, 2273.
- Zakharova, GS et al 2013. *Dalton Transactions.* 42, 14, 4897.
- Schwendt, P. et al. 1975. *Chem. Zvesti.* 29, 3, 381.
- Ni, S et al 2010. *J Alloys Compounds.* 491, 378.
- Decremps, F. et al 2001. *A. Phys. Rev B.* 65, 092101
- Markova-Velichkova, M et al 2009. *CR ACAD BULG SCI.* 62, 2, 203
- Knez M. et al 2007. *Nano Lett.*, 7, 4.

- Yu. Y. et al. 2014. Nano Lett., 14, 2528.
Balents, L. et al 2010. Nature. 464, 199.
Bose, I. et al 2005, arxiv preprint cond-mat/0502019
Chakrabarty, T. et al. 2014. J. phys: cond. matter. 26, 40, 405601.
Krusin-Elbaun, L. et al. 2010. Nature. 431, 672
Liu, H. et al. 2015. J.mater.sci. mater. electron., 26, 4, 2466
Ou, Y. et al 2010. Characterization of Room-Temperature Ferromagnetic Zn_{1-x}CoxO Nanowires
Intech Open Access Publisher.
Smart. S, J. et al 1955. AAPT. 23, 6, 356.

References of chapter VI.

- Feist et al. 1992. J. Solid State Chem. 101, 275-295
Hernández S. et al 2014. ACS Appl. Mater. Interfaces 6, 12153.
Patra M.K. et al 2008. DEF SCI J, 58, 5,636.
Garcia P. et al 2006. Adv. Mater. 2006, 18, 2768.
Song X. et al. 2007, Chinese Science Bulletin, 52, 18, 2491.
Chen Q. et al 2012. Adv Mater, 14, 17, 1208.
Zhang, Y et al 2015, RSC Adv., 5, 79479.
Le Bail et al 1992. Mat. Res. Bull., 27, 75.
Knez M. et al 2006. nature materials, 5.
Wachnicki L et al 2010. Thin Solid Films 518, 4556.
Jyh-Chiang Jiang et al 200. J. Am. Chem. Soc., 7, 1399.
Tynell et al 2014. Semicond. Sci. Technol. **29**, 043001
Iordanova et al 2011. Bulgarian Chemical Communications, 43, 3, 378
Markova-Velichkova, M et al 2009. CR ACAD BULG SCI. 62, 2, 203
Sirajudheen, J 2016. Material Sci Eng, 5:2
Thushara J. et al 2012. ACS Appl. Mater. Interfaces, 4, 6917.
Vasquez J. et al 2010. Electrochimica Acta 55, 1373.
Manthina et al 2012, J. Phys. Chem. C. 116, 23864.
Williams et al 2012. ACSNano, 6 ,7,6185.
Hernández S. et al 2014. ACS Appl. Mater. Interfaces, 6, 12153.
Knez M. et al 2006. nature materials, 5. 627.
Vásquez, J. et al 2010. Electrochim. Acta, 55, 4,
Segovia, M et al 2011, Mater.Res.Bull., 46, 11, 2191.
López-Cabaña Z. et al 2011, Nanoscale research letters, 6, 1, 1.
Muth J. F. et al 1999. J. Appl. Phys., 85, 11.
Garcia P. et al 2006. Adv. Mater. 18, 2768.
Song Xuchun et al 2007. Chinese Science Bulletin, 52, 18, 2491.
Chen X. et al 2007. Chem. Rev. 107, 2891.

Yu Y. Nano Lett. 2014, 14, 2528.
Iordanova R. et al 2011. *Bulgarian Chemical Communications*, 4, 3, pp. 378.
Knez M. et al 2006. nature materials, 5. 627
Caretta, I et al 2012. RSC Advances, 2, 7, 2696.
Raveendra, RS et al 2014. Journal of Asian Ceramic Societies, 2, 4, 357.
Nikam L. et al 2015. *New J. Chem.*, 2015, 39, 3821.
Clapp A.R et al 2004. J. AM. CHEM. SOC. 2004,
Budzikiewicz, H et al 2001, Current topics in medicinal chemistry, 1, 73.
Wheeler D. E. et al 1999. J. Phys. Chem. A, 103, 20, 4101
Williams, V.O. et al 2012, ACS nano, 6, 7, 6185.

References of Chapter VII.

- Bruce P. G. et al 2008. *Angew. Chem. Int. Ed.* 47, 2930.
Colm O'Dwyer et al 2015. *Phys. Chem. Chem. Phys.*, 17, 4799
Carlino S. et al 1997. *Solid State Ionics* 98, 73.
Drissi M et al 2015 *Molecules* 2015, 20
Flakus et al. H.T. *Spectrochimica Acta Part A*, 173, 65.
George S. M. et al 2007. *J. Phys. Chem. C*, 111, 8509.
George S.M. et al 2008. *Chem. Mater.* 20, 3315
George. S. M et al 2009. *Thin Solid Films* 517, 5658.
George S. M et al, 2009. *Chem. Rev.* 110, 111.
George S. M et al 2013. *Nano Lett.* 2013, 13, 5594
James Evans. R. et al 2008. *J. Phys. Chem. A* 2008, 112, 4125.
Karthikeyan N. et al 2015. *Spectrochimica Acta Part A* 139, 229.
Karppinen M. et al 2016. *Nano Lett.* 2016, 16, 1276.
LIU Jian-wen, et al 2010. *Trans. Nonferrous Met. Soc. China* 20, 344.
Moreno M. et al 2010. *Electrochimica Acta* 55. 1323.
Moreno M. et al 2011. *Electrochimica Acta* 58. 112
Manik Kumer Ghosh et al 2006. *Chemical Physics Letters* 426, 365.
Mendizabal F. and Donoso D 2011, *Theor Chem Acc*, 129, 381.
Nick Lane, and William F. Martin, 2012, *Cell* 151, 1406.
Puurunen RL. 2005. *J. Appl. Phys.* 97, 121301
Pan, E.; Zhang, X.; Huang, Z.; Krezel, A.; Zhao, M.; Tinberg, C.E.; Lippard, S.J.; McNamara, J.O. Seymour, J. P.; Wu, F.; Wise, K. D.; Yoo, E. *Microsystems & Nanoengineering.* 2017, 3, 16066.
Samarth, N. *Nature materials.* 2007, 6. 6, 403.
Stephan M et al 2006. 47, 16, 26, 5952.
Sledz M. et al et al 2001. *Journal of Molecular Structure.* 595, 77
Thomas, J. *Nature Mat.* 2003, 2, 705.
Tasaki K. et al. 2003. *Journal of The Electrochemical Society*, **150**, A1628.
Teñlez S Claudio A. et al 2001. *Spectrochimica Acta Part A* 57, 993.
Weingarten, C.P.; Doraiswamy, P.M. Fisher, M.P. *Frontiers in human neuroscience.* 2016, 10, 541.
Zhang S. S. Et al 2006. *Journal of Power Sources* 162, 1379.
Carlino S. / *Solid State Ionics* 98 (1997) 73 –84
Allwood D. A et al 2003. *J. Phys. Appl. Phys.* 36, 2175.
Badot J.C. et al 2000. *Electrochemical and Solid-State Letters*, 3, 10, 485.
Dai X. et al 2014 *Solid State Sciences* 27, 17.
Elam J. W. et al. 2008. *J. Vac. Sci. Technol.* 26, 2.
George. S. M et al 2009. *Thin Solid Films* 517, 5658.
Ponzoni A. et al 2017. *Sensors*, 17, 714.
Tynell T. et al. 2014. *Semicond. Sci. Technol.* 29. 043001

References of Annex

- Morris, Jr., J. W. "Defects in Crystals." Chapter 4 in *Materials Science and Engineering: An Introduction*. Wiley, 2013, pp. 76–107. ISBN: 9781118324578.
Nesper, R. et al 2002. *Z. anorg. Chem.* 628, 12, 2778.
Schwarz, H. A. et al 1980. *J. Chem. Phys.* 1980, 72: 284-287.
Pankewitz, T. et al 2007. *J. Chem. Phys.* 2007, 127, 074307.
Chen, X. et al 2002. *Inorg. Chem.* 41, 4524.
O'Dwyer, C. et al 2009. *Adv. Funct. Mater.* 2009, 19: 1-10.
Cui, H-H. et al 2008. *Thin Solid Films.* 516: 1484-1488.
Raj, D. A. Curr. et al 2010. *Appl. Phys.* 10: 531-537.

- Souza-Filho, A.G. et al 2004. *Nano Letters*. 4, 11, 2099.
- Twu J et al. 1997. *Mater. Chem.* 7, 11, 2273.
- Zakharova, G.S. et al 2013. *Dalton Transactions*. 42, 14, 4897.
- Schwendt, P. et al. 1975. *Chem. Zvesti.* 29, 3, 381.
- Ni, S et al 2010. *J Alloys Compounds*. 491, 378.
- Decremps, F. et al 2001. *A. Phys. Rev B*. 65, 092101
- Markova-Velichkova, M et al 2009. *CR ACAD BULG SCI*. 62, 2, 203
- Biesinge, M. et al 2010. *Appl. Surf. Sci.*, **257**, 887.
- Silversmit, G. J. et al 2004. *Electron Spectrosc. Relat. Phenom.* 135, 167.
- P. H. L. Notten et al. 2007. *Adv. Mater.* 19, 4564.
- Rubloff G.W. et al 2014. *Nature Nanotechnology*. 9, 1031.

ANNEXES

ANNEX-1

Table 1.1. Experimental and calculated Model 1 ^{13}C and ^1H chemical shifts (ppm) of H_6EBZnOH .

	Calculated $\text{H}_6\text{EB-ZnOH}$ (Model 1)				Exp. H_6EBZnOH			
	^1H		^{13}C		d ^1H m (J [Hz])		d ^{13}C	
10''	9.29	9.02	132.52	133.19	7.34	7.34* br d (8.3)	122.3	122.3*
10'	9.29		136.37		7.28		120.0	
10	8.49		130.69		7.25		120.0	
8''	8.21	8.36	131.72	129.82	6.92	6.87 *br d (7.6)	120.0	116.8*
8'	8.27		131.62		6.87		116.8	
8	8.61		126.13					
9''	8.07	8.02	129.36	125.55	6.70	6.35 *dd (8.3/7.6)	116.2	113.7*
9'	8.13		129.25		6.35		113.7	
9	7.88		118.04					
2	5.76	5.79	45.01	44.42	5.22	5.22 *m	53.9	53.9*
2''	6		41.42		5.04		53.9	
2''	5.62		46.83		4.97		53.9	
					4.68		56.5	
3A	6.94	6.19	58.27	57.66	5.38	5.38* m	66.02	66.02*
3A	6.27		56.25		4.70		66.02	
3A	5.35		58.45		4.60		66.02	
3B	4.28	4.89	58.27	57.66	3.98	3.98 *br d (11.0)	66.02	66.02*
3B	4.11		56.25		3.97		62.5	
3B	6.27		58.45		3.89		62.5	
4/4'/4''			187.69/172. 59/173.26	177.85			170,9	
5/5'/5''			121.12/129. 52/121.30	123.98			117,9	
6/6'/6''			161.60/146. 19/145.85	151.21			-----	
7/7'/7''			147.21/144. 97/150.85	149.34			147,5	
1/1'/1''			177.08/180. 15/176.54	177.92			-----	

(*) Average.

Table 1.2. Calculated ^{13}C and ^1H chemical shifts (ppm) of H_6EBZnOH of Model 2 and Model 1+2.

	Calculated $\text{H}_6\text{EB-ZnOH}$ (Model 2)			Calculated $\text{H}_6\text{EB-ZnOH}$ (Model 1+2)		
	^1H		^{13}C		^1H	^{13}C
10''	8.05	7.69	123.7	122.75	8.35	127.97
10'	8.1		128.01			
10	6.91		116.54			
8''	6.55	5.95	118.8	110.37	7.16	120.10
8'	6.47		121.91			
8	4.83		90.41			
9''	6.87	6.50	118.48	117.98	7.26	121.77
9'	6.47		116.02			
9	6.15		119.45			
2	3.70	4.23	38.4	36.67	5.01	40.54
2''	4.80		36.4			
2''	4.20		35.2			
3A	5.23	4.69	42.29	49.18	5.44	53.42
3A	4.97		52.88			
3A	3.87		52.36			
3B	3.16	4.04	42.29	49,18	4.46	53.42
3B	3.65		52.88			
3B	5.30		52.36			
4/4'/4''			166,93 165,62 135,61	156.03		166.95
5/5'/5''			113,42 112,19 101,52	109.04		116.51
6/6'/6''			143,06 141,11 128,62	137.60		144.41
7/7'/7''			135,96 133,05 127,16	132.06		140.7
1/1'/1''			189,1 174,92 178,1	180.7		179.32

Table 1.3. ^{13}C chemical shifts considered to obtain statistical data.

	Model 1	Model 2	Model 1+2	Experimental (Order 1)	Experimental (Order 2)	Experimental H ₆ EB	Calculated H ₆ EB
	^{13}C	^{13}C	^{13}C	^{13}C	^{13}C	^{13}C	^{13}C
10	133.19	122.75	127.97	122.3	116.8	119.7	126.8
8	129.82	110.37	120.10	116.8	113.7	119.8	125.1
9	125.55	117.98	121.77	113.7	122.3	119.6	126.5
2	44.42	36.67	40.54	53.9	53.9	53.7	45.6
3	57.66	49.18	53.42	66.02	66.02	65.8	55.2
4	177.85	156.05	166.95	170.9	170.9	170.7	177.0
5	123.98	109.07	116.51	117.9	117.9	116.8	125.0
7	149.34	132.06	140.7	147.5	147.5	147.2	149.3

Table 1.4. Calculated and experimental ^{13}C δ linear correlation results (statistical data).

Name	$y = m*X + b$	S.D	R ²
Model 1 vs Experimental order 1	$Y = 0.84X + 15.71$	5.72	0.98
Model 2 vs Experimental order 1	$Y = 0.91X + 18.7$	7.72	0.97
Model 1+2 vs Experimental order 1	$Y = 0.88X + 16.74$	6.52	0.98
Model 1 vs Experimental order 2	$Y = 0.835X + 15.591$	6.77	0.974
Model 2 vs Experimental order 2	$Y = 0.913X + 18.725$	7.77	0.9659
Model 1+2 vs Experimental order 2	$Y = 0.8738X + 16.935$	7.06	0.9718

Table 1.5. ^1H chemical shifts considered to obtain statistical data.

	Model 1	Model 2	Model 1+2	Experimental (Order 1)	Experimental (Order 2)	Experimental H ₆ EB	Calculated H ₆ EB
	^1H	^1H	^1H	^1H	^1H	^1H	^1H
10	9.02	7.69	8.35	7.34	6.87	7.24	8.47
8	8.36	5.95	7.16	6.87	6.35	6.94	8.04
9	8.02	6.50	7.26	6.35	7.34	6.69	7.76
2	5.79	4.23	5.01	5.22	5.22	5.04	5.33
3A	6.19	4.69	5.44	5.38	5.38	4.69	6.14
3B	4.89	4.04	4.46	3.98	3.98	4.61	4.63

Table 1.6. Calculated and experimental ^1H δ linear correlation results (statistical data).

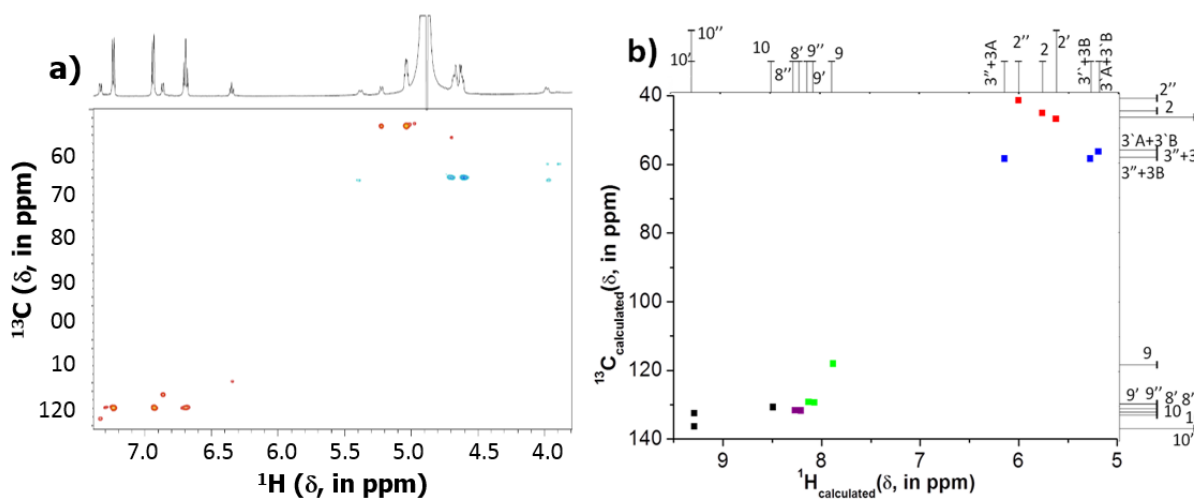
Name	$y = m*X + b$	S.D	R ²
Model 1 vs Experimental order 1	$Y = 0.74X + 0.65$	0.25	0.97
Model 2 vs Experimental order 1	$Y = 0.78X + 1.54$	0.56	0.83
Model 1+2 vs Experimental order 1	$Y = 0.79X + 0.97$	0.38	0.93
Model 1 vs Experimental order 2	$Y = 0.6908X + 0.99$	0.54	0.85
Model 2 vs Experimental order 2	$Y = 0.7559X + 1.6868$	0.65	0.78
Model 1+2 vs Experimental order 2	$Y = 0.7388X + 1.2162$	0.56	0.83

Table 1.7. Condition Established from experimental ^{13}C δ in CD_3OD of H_6EBZnOH and H_6EB .

Label	H_6EB in CD_3OD	H_6EBZnOH (Order 1) in CD_3OD	Condition Established in CD_3OD	H_6EB in CD_3OD	Condition Established in CD_3OD
10	119.7	122.3	<	119.7	>
8	119.8	116.8	>	119.8	>
9	119.6	113.7	>	119.6	<
3	65.8	66.02	<	65.8	<
2	53.7	53.9	<	53.7	<

Table 1.8. Evaluation of the condition established from experimental ^{13}C using theoretical ^{13}C δ of the H_6EB (see chapter 5.1), Model 1 and Model 2.

Label	H_6EB	Model 1	Condition Established. Does it apply?	H_6EB	Model 2	Condition Established Does it apply?
10	126.8	133.19	<	126.8	122.75	>
8	125.1	129.82	<	125.1	110.37	>
9	126.5	125.55	>	126.5	117.98	>
3	55.2	57.66	<	55.2	49.18	>
2	45.6	44.42	>	45.6	36.67	>

Figure 1.1. ^{13}C - ^1H 2D-NMR Spectra of (a) $\text{H}_6\text{EB}(\text{ZnOH})_2$ experimental result and (b) extended simulated $\text{H}_6\text{EB}(\text{ZnOH})_2$ (model 1).

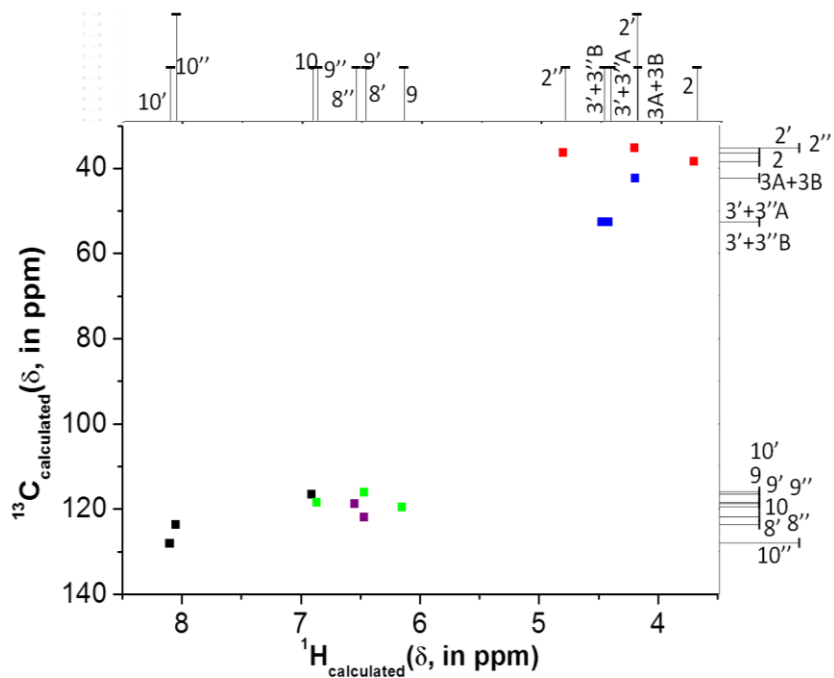


Figure 1.2. ^{13}C - ^1H 2D-NMR Spectra of the extended simulated $\text{H}_6\text{EB}(\text{ZnOH})_2$ (model 2).

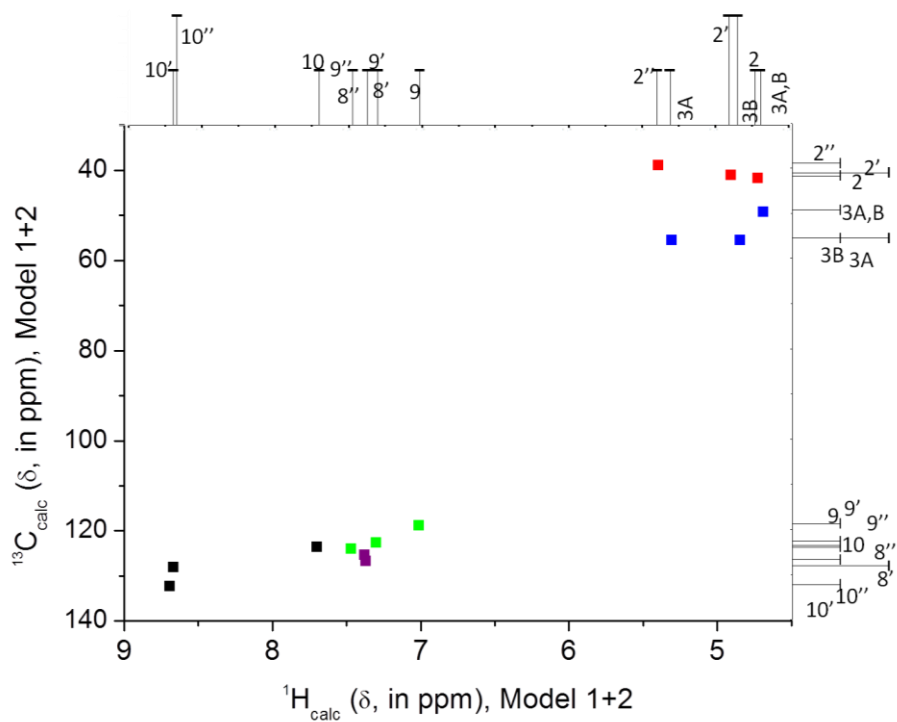


Figure 1.3. ^{13}C - ^1H 2D-NMR Spectra of the extended simulated $\text{H}_6\text{EB}(\text{ZnOH})_2$ (model 1+2).

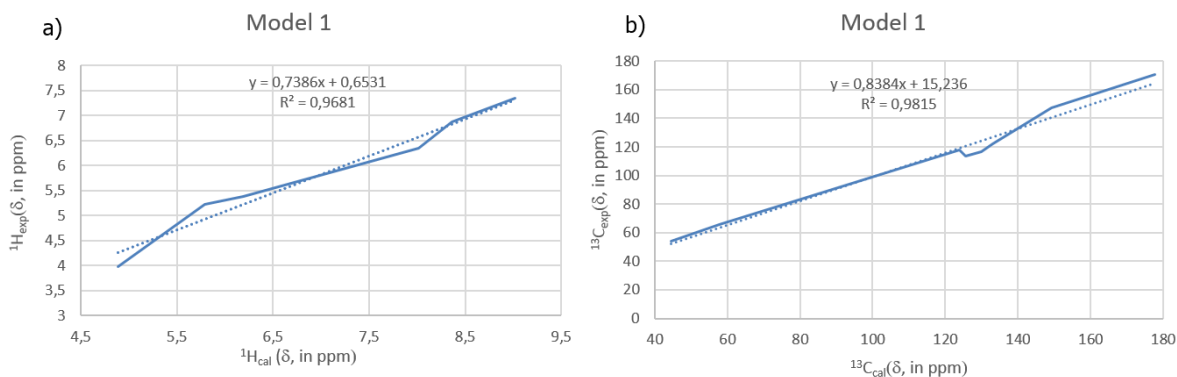


Figure 1. 4. $^{13}\text{C}, ^1\text{H}$ Model 1 linear correlation; a) $^1\text{H}_{\text{Experimental}}$ and $^1\text{H}_{\text{Calc}}$ linear correlation ($^1\text{H}_{\text{Experimental}}=0.7386 \ ^1\text{H}_{\text{Calc}} + 0.6531$), and (b) $^{13}\text{C}_{\text{Experimental}}$ and $^{13}\text{C}_{\text{Calc}}$ linear correlation ($^{13}\text{C}_{\text{Experimental}}=0.8384 \ ^{13}\text{C}_{\text{Calc}} + 15.236$).

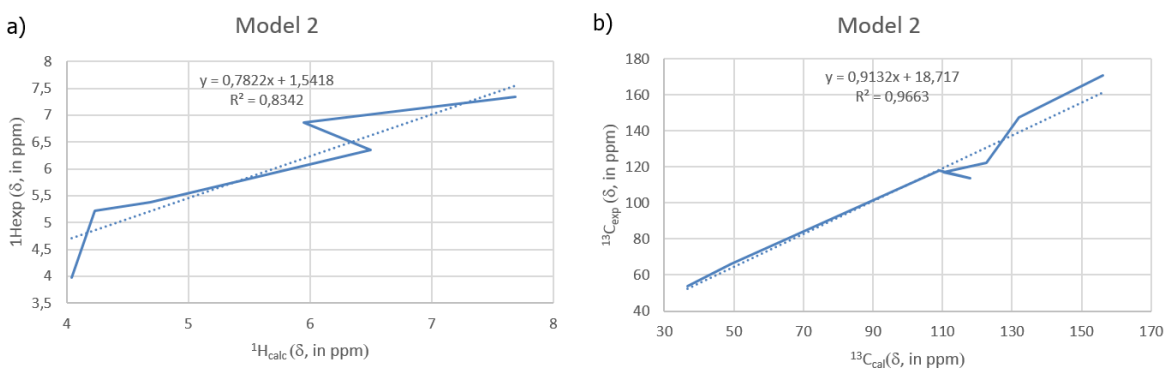


Figure 1. 5. $^{13}\text{C}, ^1\text{H}$ Model 2 linear correlation; a) $^1\text{H}_{\text{Experimental}}$ and $^1\text{H}_{\text{Calc}}$ linear correlation ($^1\text{H}_{\text{Experimental}}=0.7822 \ ^1\text{H}_{\text{Calc}} + 1.5418$), and (b) $^{13}\text{C}_{\text{Experimental}}$ and $^{13}\text{C}_{\text{Calc}}$ linear correlation ($^{13}\text{C}_{\text{Experimental}}=0.9132 \ ^{13}\text{C}_{\text{Calc}} + 18.717$).

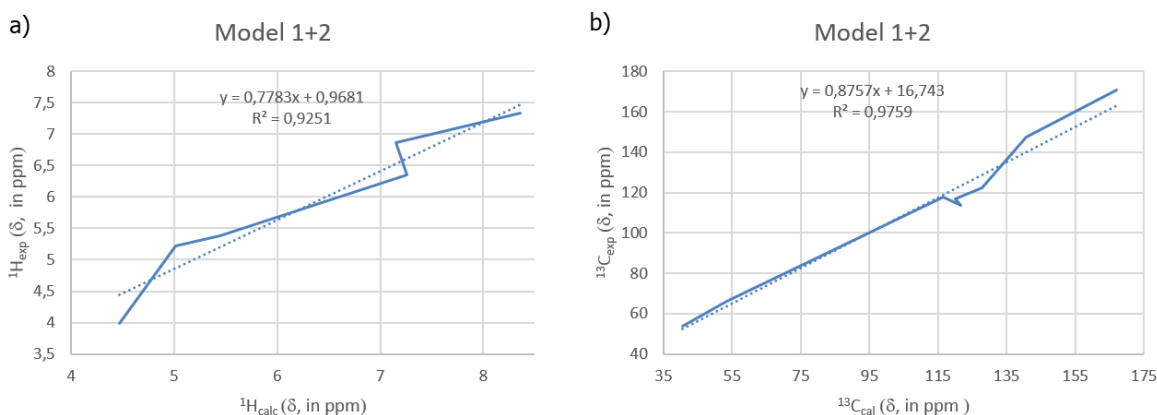


Figure 1. 6. $^{13}\text{C}, ^1\text{H}$ Model 1+2 linear correlation; a) $^1\text{H}_{\text{Experimental}}$ and $^1\text{H}_{\text{Calc}}$ linear correlation ($^1\text{H}_{\text{Experimental}}=0.7783 \ ^1\text{H}_{\text{Calc}} + 0.9681$), and (b) $^{13}\text{C}_{\text{Experimental}}$ and $^{13}\text{C}_{\text{Calc}}$ linear correlation ($^{13}\text{C}_{\text{Experimental}}=0.8757 \ ^{13}\text{C}_{\text{Calc}} + 16.743$).

ANNEX-II

2.1 S- 2 ESEM.

Figure 2.1 reveals that small squares growth from heterosupramolecular squares buildings. They arise from unassembled threads like exhibits in figure 2.1-1b (inset). Figure 2.1-1c shows the rolling beginning of squares packed revealing their individual lamellar morphology which could lead to the formation of nanotubes. Figure 2.1-1d shows the presence of rod morphology which arouse from squares buildings and concentric squares like show in figure 2.1-1e and 2.1-1f.

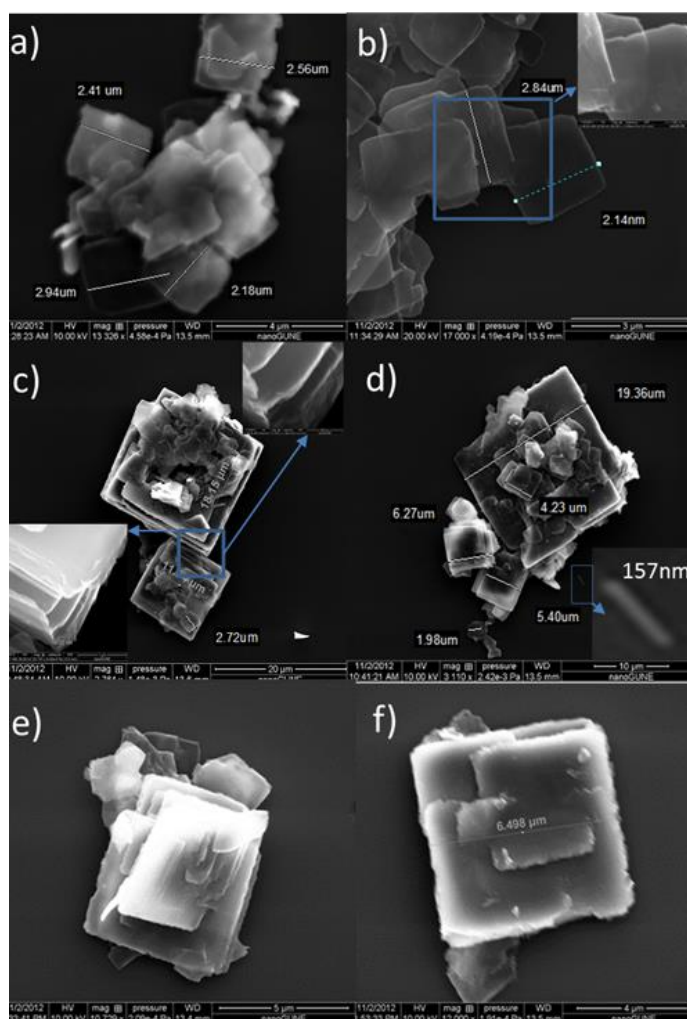


Figure 2.1 S- 2 ESEM micrographs at different scale bars revealing the squares growth.

2.2 S 2 HRTEM.

The structural study, including HRTEM together with SAED of S- 2 are showed in figure 2.2. It indicates that the structure of the $(\text{NH}_4)_2\text{V}_7\text{O}_{16}$ compound corresponds to a square network 2D with $a = b = 0.61 \text{ nm}$ and $\alpha = \beta = 90^\circ$ like reported Nesper et al [Nesper, R. et al 2002] with crystal cell parameters; $a: 6.161(2)\text{\AA}$, $b: 6.170(2)\text{\AA}$ and $c: 19.111(7)\text{\AA}$, and $\alpha: 96,13^\circ$, $\beta: 92.819$ and $\gamma: 90.067^\circ$, suggesting the existence of triclinic p^{-1} space group.

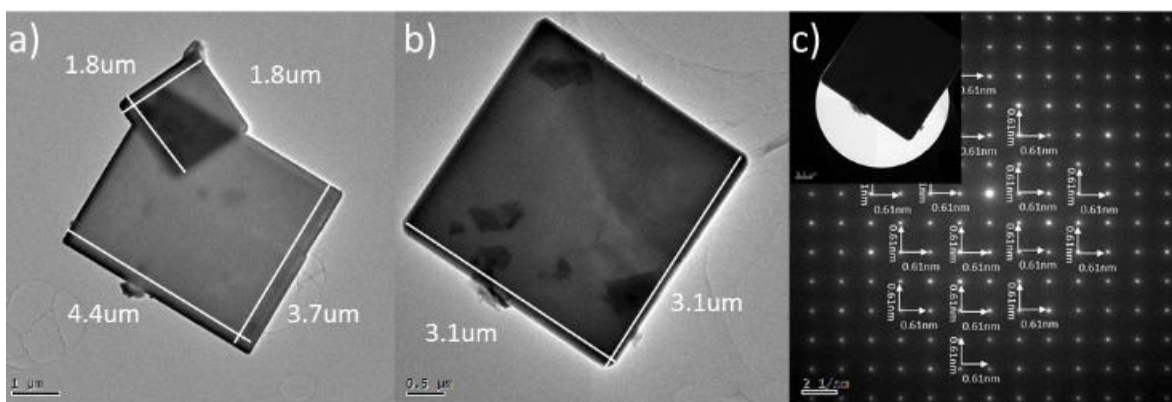


Figure 2.2 S- 2 HRTEM micrographs at different scale bars; a) $1 \mu\text{m}$ and b) $0.5 \mu\text{m}$ and c) SAED analysis.

2.3 S- 2 XPS.

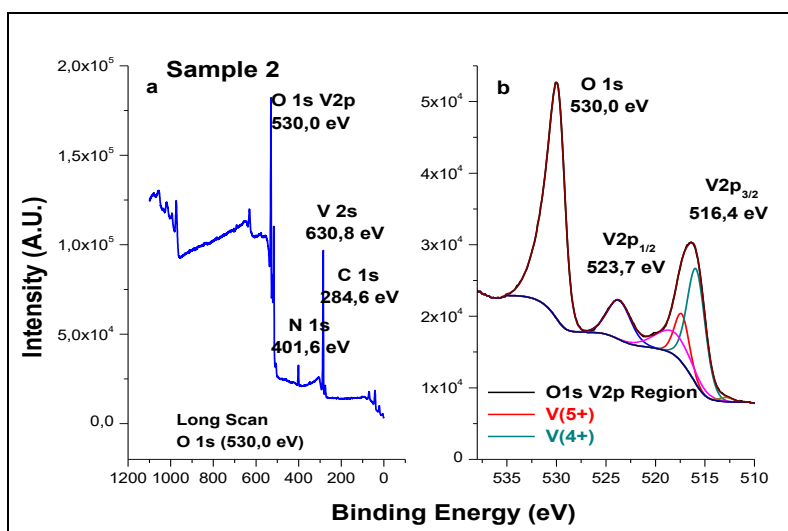


Figure 2.3 S 2 XPS result; a) XPS survey scan and b) detailed XPS data of the O 1s and V 2p regions.

2.4 S- 2 IR Spectra.

S-2 spectra of two characteristic zones is showed in figure 2.4 In the range 3800 - 1400 cm^{-1} , they show N-H bands attributable to the ammonium cation (NH_4^+). At lower energies, in the range 1100 - 450 cm^{-1} the typical vibrations of vanadium oxide are observed; among them, the vanadyl bond, $\text{V}=\text{O}$ has a special interest for this study. The tetrahedral ammonium ion has 4 normal vibrational modes; two N-H stretch vibrations, one symmetrical (ν_1) $\sim 3278 \text{ cm}^{-1}$ and other asymmetric (ν_3) $\sim 3367 \text{ cm}^{-1}$ respectively, one symmetric bend (ν_2) $\sim 1682 \text{ cm}^{-1}$, and one asymmetric bend $\sim 1439 \text{ cm}^{-1}$ (ν_4) [Pankewitz et al 2007]. Of these, only two are active in the infrared (ν_3 and ν_4). However, the ion symmetry can be reduced when there are interactions with either neighbouring, solvent counterions, or/and solid lattices, generating more complex spectra [Pankewitz et al 2007]. The latter appears to be the case for the ammonium ions present in the compound $(\text{NH}_4)_2\text{V}_7\text{O}_{16}$. In the higher-frequency region of the spectrum there is a set of absorptions that can be assigned to the stretching vibration modes of ammonium ion, both free and interacting with the matrix by hydrogen bridges. Broadband centered at 3440 cm^{-1} can thus correspond to the asymmetric (ν_3) and symmetric (ν_1) stretching modes of free N-H bonds.

The symmetric bend modes (ν_2) of the same N-H bonds appears in the range of 1515-1556 cm^{-1} , while those of asymmetric bend modes (ν_4) are in bands centred at 1396 and 1433 cm^{-1} . On the other hand, the bands centred at 3169 and 3198 cm^{-1} would correspond to the asymmetric stretching vibrations, while that at 2919 cm^{-1} can be assigned to the symmetrical stretching of the N-H bonds linked to the lattice. The symmetric bend modes “ ν_2 ” and asymmetric bend modes “ ν_4 ” in these types of bonds ($\text{N-H-O} = \text{V}$) would be those located at 1691-1714 cm^{-1} and 1617 and 1647 cm^{-1} , respectively. The band assignment in the spectrum of in figure 2.4 are compared with ammonium ion complexes in ammonia reported for Schwarz et al [Schwarz, H. A. et al 1980] and Pankewitz et al [Pankewitz, T. et al 2007.]. At low frequencies of the FT-IR spectrum, it corresponds to the vibrations of the vanadium oxide lattice, the absorptions that appear at 490, 573 and 786 cm^{-1} correspond to V-O-V vibrations, whereas that at 991 cm^{-1} is characteristic of $\text{V}=\text{O}$ bond asymmetric stretching mode. The absorptions at 490 and 573 cm^{-1} have been assigned to the modes of deformation of the V-O-V bond and the (V-O-V) symmetrical stretching respectively in V_2O_5 . FT-IR from nanotubes and nanourchin vanadium oxide reported by Chen, X., et al [Chen, X. et al 2002] and O'Dwyer, C., et al [O'Dwyer, C. et al 2009.]. The absorption band at 786 cm^{-1} is close to the (V-O-V) ν_{as} vibration reported by Cui, H-H., Y et al [Cui, H-H. et al 2008.]. The absorption detected as a shoulder at 936 cm^{-1} in the spectrum illustrated in figure 2.4 may correspond to a vibration observed by Raj, DA, et

al [Raj, D. A. Curr. et al 2010] at 836 cm^{-1} which correspond to the overlapping of the $(\text{V} = \text{O})_v$ stretching modes and $(\text{VOV})_v$, or impurities in the sample.

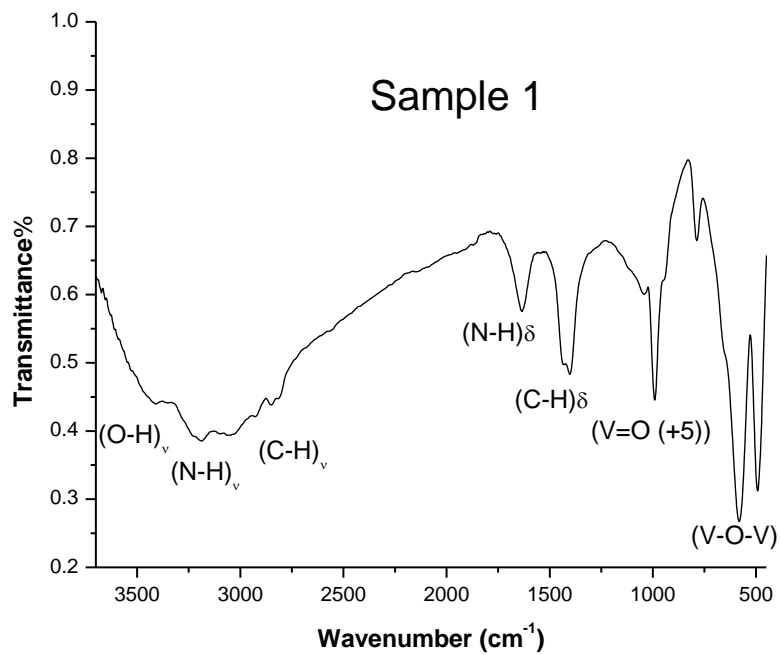


Figure 2.4 S 2 IR spectra.

2.5 S- 3 IR Spectra.

Table 2.1 S- 3 and 4 IR frequencies and bands assignment. Ref [Markova-Velichkova M. et al 2009, Ni. S. et al 2010]

S- 3	S- 4	Band Assignment
3936.18	3936.02	V-OH
3890.54	3892.75	V-OH
	3863.29	O-H from Zn-OH
3853.99	3851.57	O-H
		O-H
3826.52	3825.88	O-H
3811.16	3810.25	O-H
3744-3622	3741-3497	H-O-H ZnOH
3077.74	3190.26	NH ₄
2973.58		C-H
2940.49	2921.05	C-H
	2857.02	C-H
2869.24	2728.96	C-H
2828.16		
1698.57	1698.57	O-H
1643.73	1643.01	NH ₄
1501.94	1509.1	NH ₄
1470.14	1470.15	NH ₄
1291.69	1264.11	V=O
	1163.53	V=O
1035.69	1085.98	V=O
811.48	999.02	V=O
	853.75	ZnO ₆ , VO ₆ [Markova-Velichkova M. et al 2009]
	765.74	V-O-V
	688.19	ZnO ₆ , VO ₆ [Markova-Velichkova M. et al 2009]
596.69	587.60	ZnO ₆ , V-O-V [Markova-Velichkova M. et al 2009]
	537.31	ZnO ₆ , VO ₆ [Markova-Velichkova M. et al 2009]
	509.74	ZnO ₆ , VO ₆
	480.50	Zn-O [Ni S. et al 2010]
	465.20	Zn-O [Ni S. et al 2010]

2.6 S- 3 ESEM.

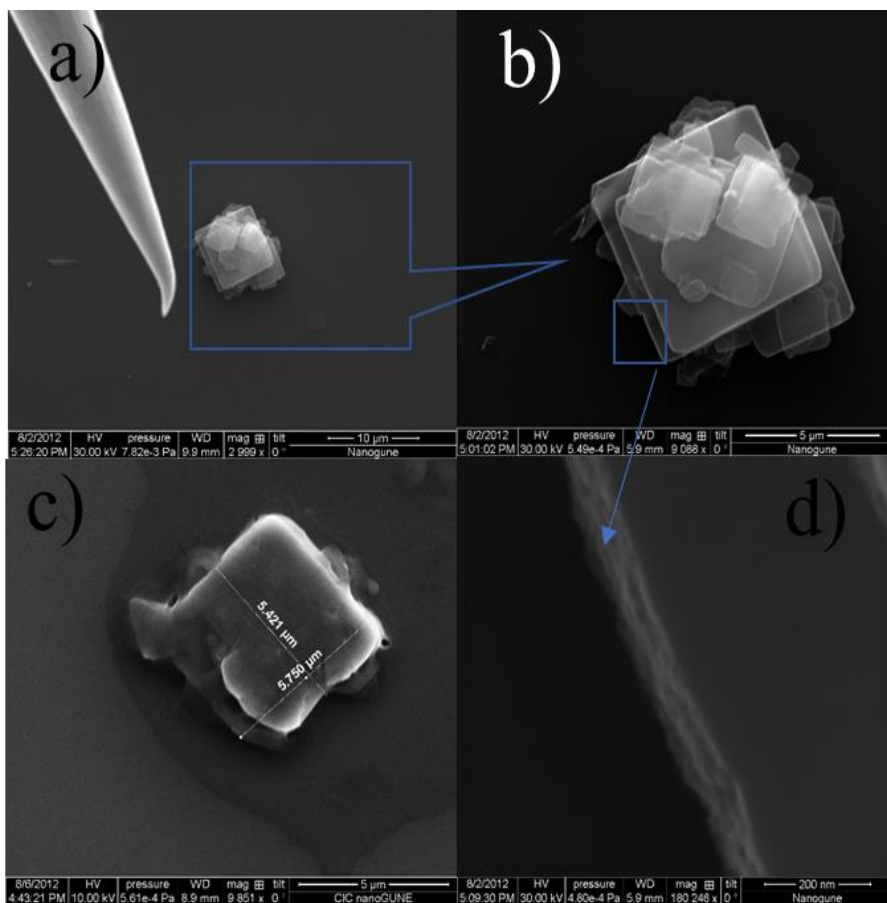
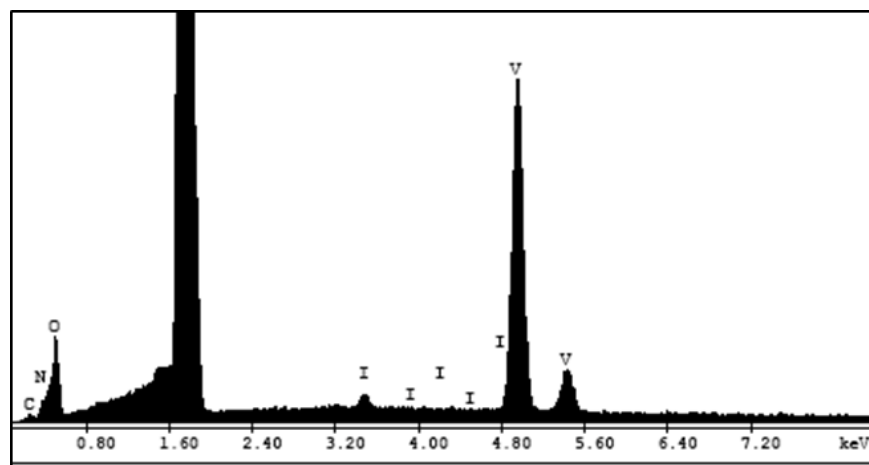
Figure 2.5S 3 ESEM images with different magnification; a) 10 μm , b) 5 μm , c) 5 μm and d) 200nm.

Figure 2.6 S- 3 EDX results.

Figure 2.7 shows branches-like arising from the surface, and fringes-like in both edges and corner

square which are frequently defects of the material. Indeed, crystals are invariably imperfect because the presence of defects up to a certain concentration leads to a reduction of free energy. Vacancy is a stoichiometry defect and often involves an atom displaced off its lattice site into an interstitial site that is normally empty like NaCl (schottky defect) and AgCl (Frenkel defect) type structure. So, vacancy point defect affects not only the direction of crystal growing (dimensionality), but also their electronic properties as charge carriers and mobility [Morris, J. W. et al 2013]. Vacancy point defect, dislocations and stacking faults are viewed in V_7O_{16} squares, and although they are like traces in the sample, fringes-like defects seem to be that at certain size become in nanotubes from a rolling edge of the square, being the dislocation defect their starting point.

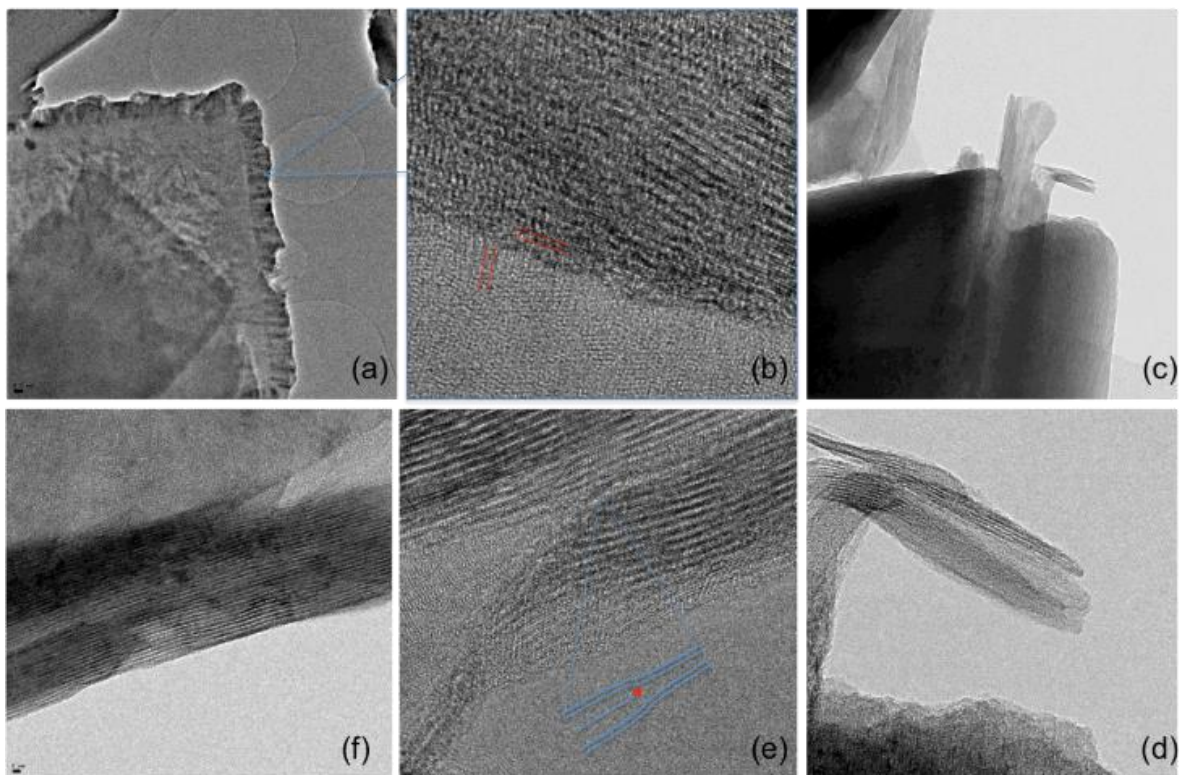


Figure 2.7 S- 3 TEM defects images (a,b) Fringe edges-stacking faults; (c,d) rolling tubes; (e,f) dislocation.

2.8 S- 3 XPS results.

Figure 2.8 depicted the survey scan which showed the presence of vanadium, oxygen, carbon and nitrogen. Although the sample was doped with iodine the amount taken up was below the detection limit of the XPS measurement. Deconvolution of the vanadium $2p_{3/2}$ peak, following literature procedures [Biesinge, M. et al 2010, Silversmit, G. J. et al 2004], showed the presence of two oxidation states, V^{5+} and V^{4+} . The V^{5+} component was found at 517.1eV whilst the $4+$ component was centred at 515.7eV. Further analysis showed a ratio of V^{5+} : V^{4+} of approximately 2.2: 1 (68.75% vs 31.25%).

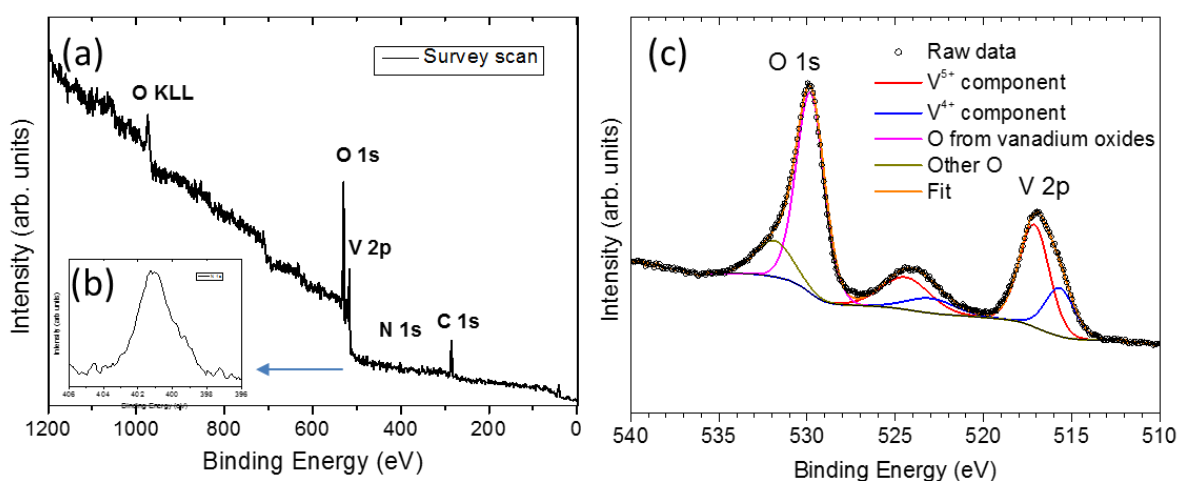


Figure 2.8 S- 3 XPS result; a) XPS survey scan b) N 1s region and c) detailed XPS data of the O 1s and V 2p regions.

The O 1s region shows the presence of at least two components as detailed above. The lower binding energy component (at 529.8eV) is assigned to vanadium oxide species (V^{5+} and V^{4+}) whilst the smaller, higher binding energy component is assigned to hydroxide species, water and oxygen content from the underlying carbon tape. Nitrogen was expected due the presence of an ammonium group in the complex (figure 2.8b). The C 1s signal was almost entirely assigned to the underlying carbon tape. Elemental composition results showed the following (taking into account only the O assigned to vanadium oxide): Overall: V (27%): O (65%): N (8%), V: O of 1: 2.4 (close to the theoretical V_7O_{16} of 1: 2.3), V: N 3.5 : 1, O : N 8.5 : 1.

2.8 S- 4 Raman cross-section.

Table 2. 2 S- 3, $\text{NH}_4\text{V}_3\text{O}_8$, NH_4VO_3 and V_2O_5 Raman frequencies and bands assignment.

S- 3	$\text{NH}_4\text{V}_3\text{O}_8$ [Souza-Filho. AG et al 2004]	NH_4VO_3 [Twu J et al. 1997]	V_2O_5 [Zakharova, GS et al 2013]	Band assignment
150.40 s	ND	ND	ND	$\delta\text{V-O}$; V-O-V ; N-H
278.45 s	265/297	260	286	$\delta\text{V-O}$; V-O-V ; N-H
350.27 s	370	329/378	303	$\delta\text{V-O}$; V-O-V ; N-H
483.52 s	428/442	495	406	$\nu\text{V-O-V}$
527.21s	514/555		514/555	$\nu\text{V-O-V}$
681.01s	675/810	645/895	675/810	$\nu\text{V-O-V}$
874				$\nu\text{V=O}$ in distorted Oh
993.57s	963	927	963/992	$\nu\text{V=O}$ in distorted Oh and SP.
1017				$\nu\text{V=O}$ in distorted Oh

ND: No data.

Table 4. S- 3 and 4 surface map Raman spectra.

S- 3	S- 4				$\text{Zn}_2\text{V}_2\text{O}_7$ [Schwe ndt, P. et al. 1975]	$\text{Zn}_3(\text{VO}_4)_3$ [Ni, S et al 2010]	ZnO Wurtzit a [Decre mps, F. et al 2001]	Band Assignment
Gray	Blue	Orange	Sky Blue	Black				
150.4					148	155		$\delta\text{V-O}$, $\delta\text{N-H}$
	168.35	168.35	168.40	172.03	161	178		$\delta\text{Zn-O}$
278.45	265.69	264.32	264.40	270.45	269	261		$\delta\text{V-O}$, $\delta\text{N-H}$
		309.82	309.82	310.04	303/ 325	317		$\delta\text{V-O}$ $\delta\text{N-H}$
	324.46						329	ZnO
350.27								$\delta\text{V-O}$ $\delta\text{N-H}$
	375.79	376.66	376.66	395.48	352		382	δZnO
	401.35	396.77	396.77	419.70	431	394/ 457	414/ 457	νZnO
	425.97						433	
483.52	493.9/ 509.25	503.63	517.04	505.2	514			$\nu\text{V-O-V}$
527.21								
	574.80	575.88	575.88				574/ 580	νZnO
	616.76	610.70	604.00	606.81				νZnO

681.01								vV-O-V
	688.57	684.25	687.07	689.66		691		vZn-O
	727.08	727.78		725.78	719			vV-O-V
	775.75			769.91	786	796		vV-O
	807.55	806.46	-	798.03 8	812	815		vV-O
874								
		850.16/ 868.98	850.16/ 862.27	844.75/ 867.46	858/ 863	860		vV=O distorted Oh, SP
	888.44	902.29	906.40	907.70	912			vV=O
993.57					964			vV=O
1017								vV=O

2.4.2 S- 4 FIB-SEM-EDX.

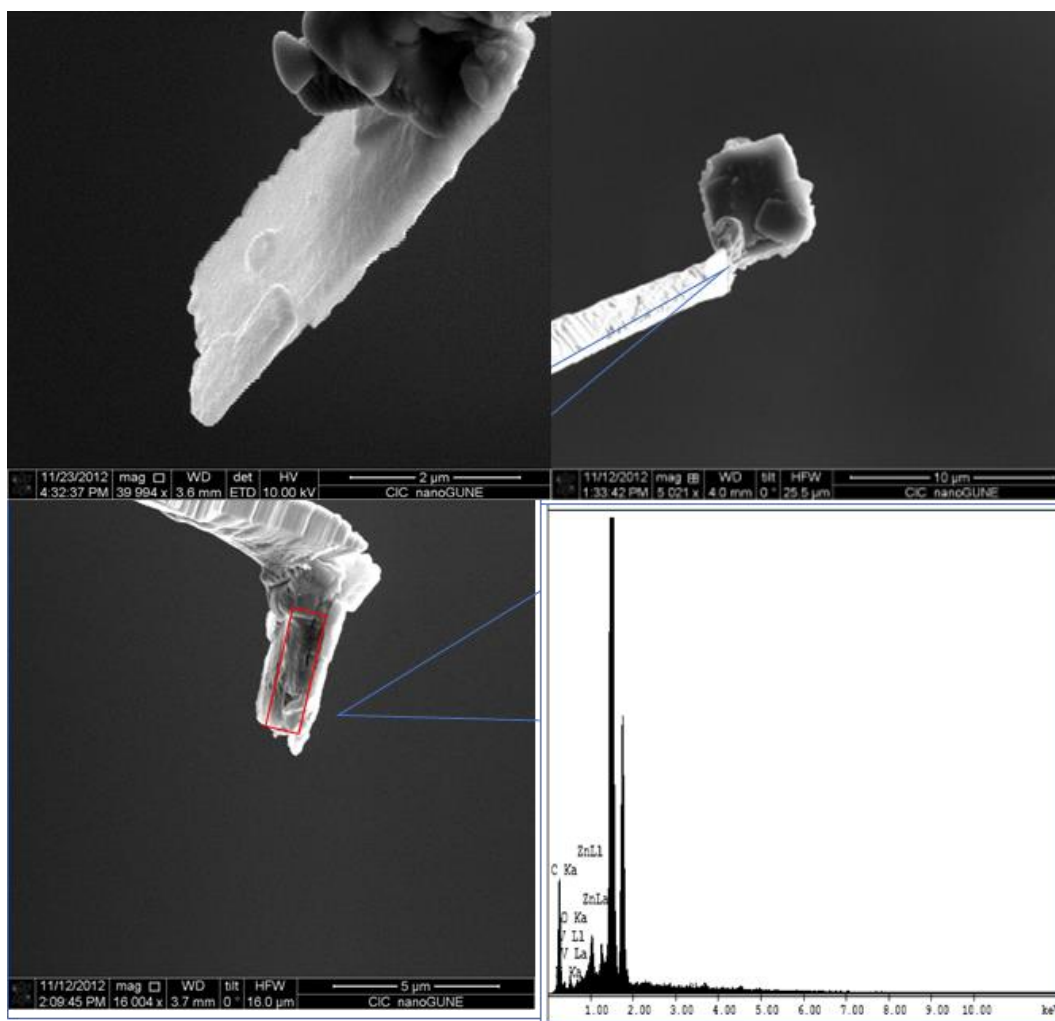


Figure 2.9 S- 4 FIB-SEM-ED micrographs.

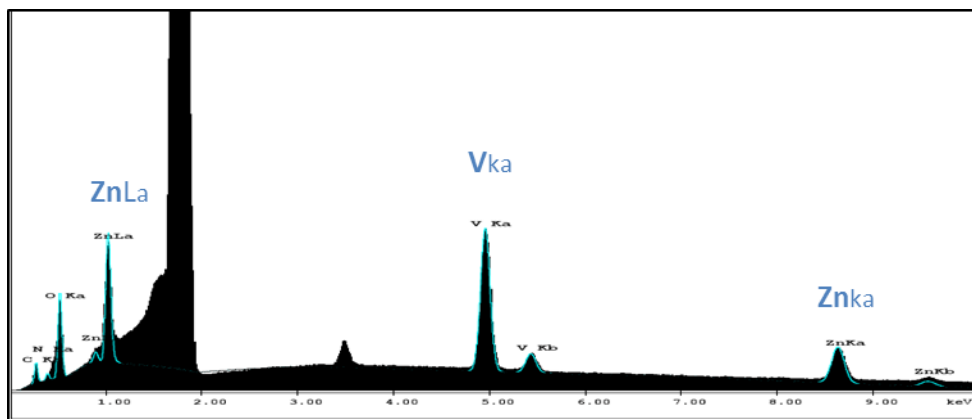
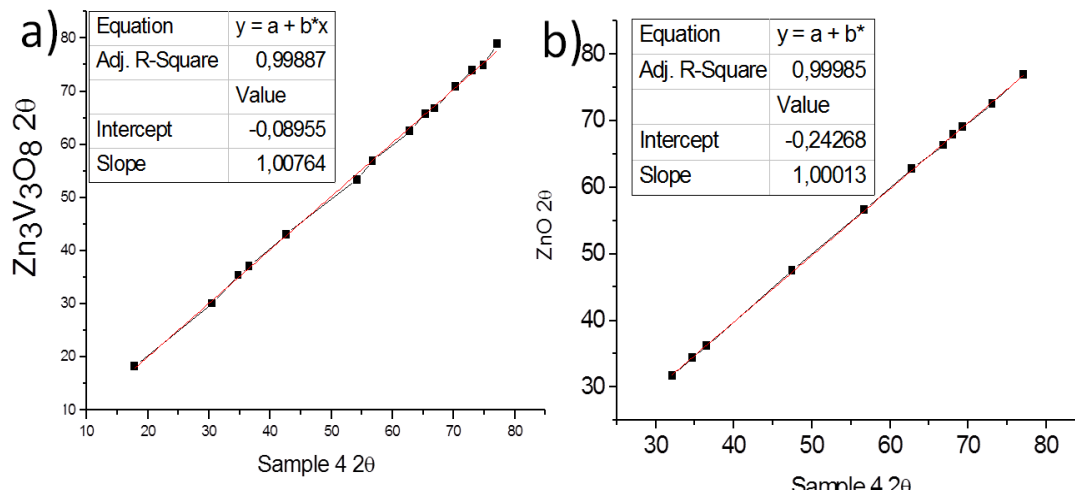


Figure 2.10 S- 4 ESEM/EDX results.

Figure 2.11 XRD Linear correlation of $Zn_3V_3O_8$ (a) and ZnO (b) with S- 4.

ANNEX-IV

4.1 AIO-T ALD-MLD.

Table 4.1 Model 1-4 and TCl bond distances (Å).

Number	Bond (A°)	Model 1	Model 2	Model 3	Model 4	TCL
25-26	O-H	-----	-----	-----	0.96335	
25-3	O-Al	-----	-----	-----	1.71434	
1-2	H-O	0.96368	0.96369	0.96372	0.96332	
2-3	O-Al	1.68457	1.67819	1.67641	1.71429	
3-4	Al-O	1.75055	1.75944	1.76140	1.91296	
3-5	Al-O	1.75439	1.76346	1.76503	1.91296	
5-6	O-C	1.39035	1.37736	1.37425	1.28481	(C-Cl) 1.81386
4-6	O-C	1.38942	1.37628	1.37345	1.28485	1.19570
6-7	C-C	1.35649 (C=C)	1.39280 (C:::C)	1.39267 (C:::C)	1.4765 (C-C)	1.4904
7-8	C-C	1.4513 (C-C)	1.43147 (C:::C)	1.43267 (C:::C)	1.40343(C:::C)	1.40562
8-11	C-H	1.08592	1.08525 (C=C)	1.08500 (C=C)	1.08477	1.08350
8-10	C-C	1.35496(C=C)	1.37999	1.37744	1.39124(C:::C)	1.39102
10-15	C-H	1.08590	1.08475	1.08529	1.08477	1.08467
10-14	C-C	1.45715 (C-C)	1.41529	1.41693	1.40344	1.40562
7-9	C-C	1.45729 (C-C)	1.43235	1.43265	1.40343	1.40562
9-13	C-H	1.08584	1.08518	1.08499	1.08477	1.08467
9-12	C-C	1.35479 (C=C)	1.37826	1.37747	1.39124	1.39102
12-16	C-H	1.08586	1.08549	1.08529	1.08477	1.08351
12-14	C-C	1.45728(C-C)	1.41628	1.41700	1.40343	1.40308
14-17	C-C	1.35649 (C=C)	1.46997 (C-C)	1.44751 (C:::C)	1.4766 (C-C)	1.49107
17-19	C-O	1.38935	1.23128 (C=O)	1.29728 (C:::O)	1.28480 (C=O)	(C-Cl) 1.81366
19-20	O-Al	1.75079	-----	1.89330	1.91301	----
17-18	C-O	1.39041	1.35497	1.29740	1.28486	1.19571
18-20	O-Al	1.75414	1.75630	1.89316	1.91301	-----
20-21	Al-O	1.68466	1.68466	1.72341	1.71429	-----
21-22	O-H	0.96371	0.96371	0.96367	0.96333	-----
20-23	Al-O	----	-----	1.72343	1.71411	-----
23-24	O-H	----	-----	0.96367	0.96322	-----

Table 4.2 Model 1-4 and TCI bond angles ($^{\circ}$).

Angle ($^{\circ}$)	Model 1	Model 2	Model 3	Model 4	TCL
26-25-3	-----	-----	-----	125.64647	
1-2-3	130.45486	131.98967	132.35769	125.72094	
2-3-5	143.23642	137.41843	144.09354	110.05168	
2-3-4	137.29184	137.41843	137.43407	113.98318	
3-4-6	86.64545	86.55829	86.57796	87.66364	
3-5-6	86.46641	86.36652	86.40935	87.66458	
4-6-7	126.28629	125.77925	125.74386	122.27617	125.23925
5-6-7	126.29730	125.82728	125.71565	122.26157	115.73628
6-7-9	121.32995	120.71164	120.59312	119.60880	116.49180
6-7-8	121.40930	120.81811	120.62449	119.59684	123.73991
10-14-17	121.41613	122.20666	120.23558	119.60936	116.49286
12-14-17	121.32342	118.93006	120.27320	119.59637	123.73861
14-17-19	126.34479	123.77187	122.94564	122.26147	(C-C-Cl)115.73743
14-17-18	126.23845	114.93484	122.91525	122.27577	125.23487
17-18-20	86.47384	122.32080	87.82143	87.66382	
17-19-20	86.63758	-----	87.81860	87.66580	
19-20-21	137.33380	-----	115.29420	113.91616	
18-20-21	143.19420	115.68911	110.99761	110.13695	
20-21-22	130.38572	122.53190	123.8002	125.67648	
18-20-23	-----	123.72539	115.31248	113.92293	
20-23-24	-----	112.38434	123.75590	125.90864	

Table 4.3 Model 1-4 and TCl dihedral angles ($^{\circ}$).

Dihedral Angle($^{\circ}$)	Model 1	Model 2	Model 3	Model 4	TCL
26-25-3-4	-----	-----	-----	161.10805	
1-2-3-4	-179.98379	-179.99930	179.90056	-123.59762	
1-2-3-5	0.01188	-0.00209	0.06583	160.94998	
3-4-6-7	179.98265	-179.96559	- 179.82794	179.92510	
3-5-6-7	-179.98266	179.96558	179.82807	-179.92510	
4-6-7-9	0.00159	-0.01513	-0.03101	0.19941	-0.00223 (Cl-C-C-C)
5-6-7-8	0.0000	0.02602	0.09096	0.15860	-0.00162
10-14-17-18	-0.06098	0.06936	-0.02583	-0.18104	0.00500
12-14-17-19	0.03025	0.06896	-0.02562	-0.17881	0.00729
12-14-17-18	179.94373	-179.92538	179.98800	179.79902	-179.993
10-14-17-19	-17997845	-179.93830	179.96055	-0.17881	-179.994 (C-C-C-Cl)
14-17-19-20	179.89356	-----	- 179.94036	179.95013	
14-17-18-20	-179.89369	179.93784	179.94036	-179.95013	
18-20-21-22	-0.40895	-0.08613	- 162.41779	-160.54201	
19-20-21-22	179.80280	-----	120.26303	123.99430	
18-20-23-24	-----	0.00539	- 161.92456	124.26194	

4.2 Others lamellar nanocomposites obtained by ALD and MLD processes.

4.2.1 ZnO-T ALD-MLD.

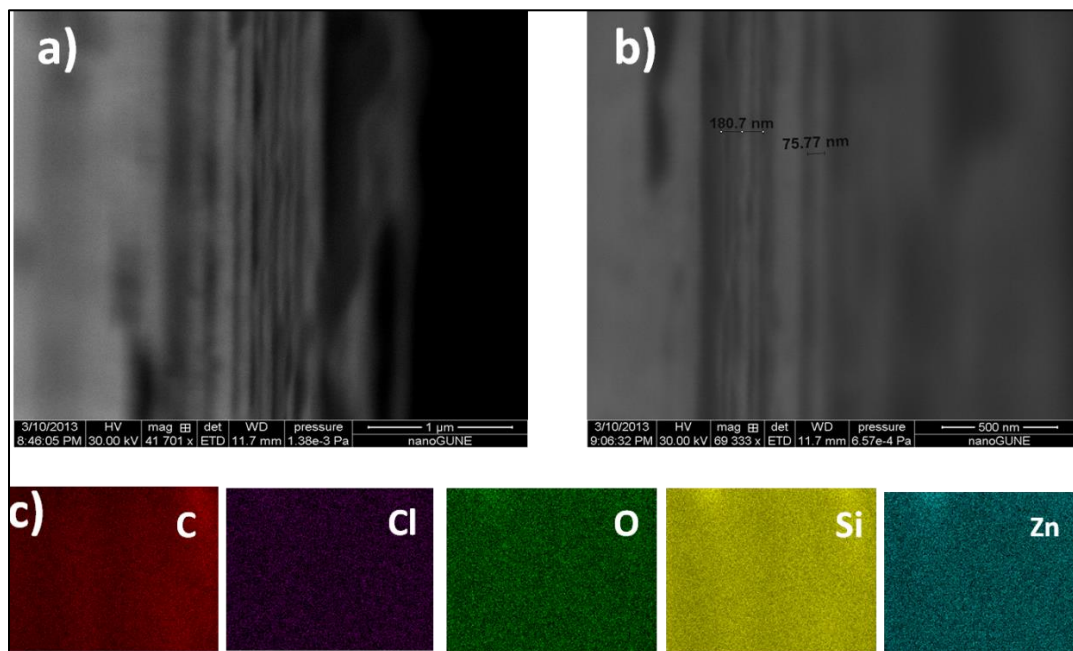


Figure 4.1 2ZnO-T Cross-section SEM micrograph; a, b) lamellar overview, and c) EDX-map.

4.2.2 ZnO-EG ALD-MLD.

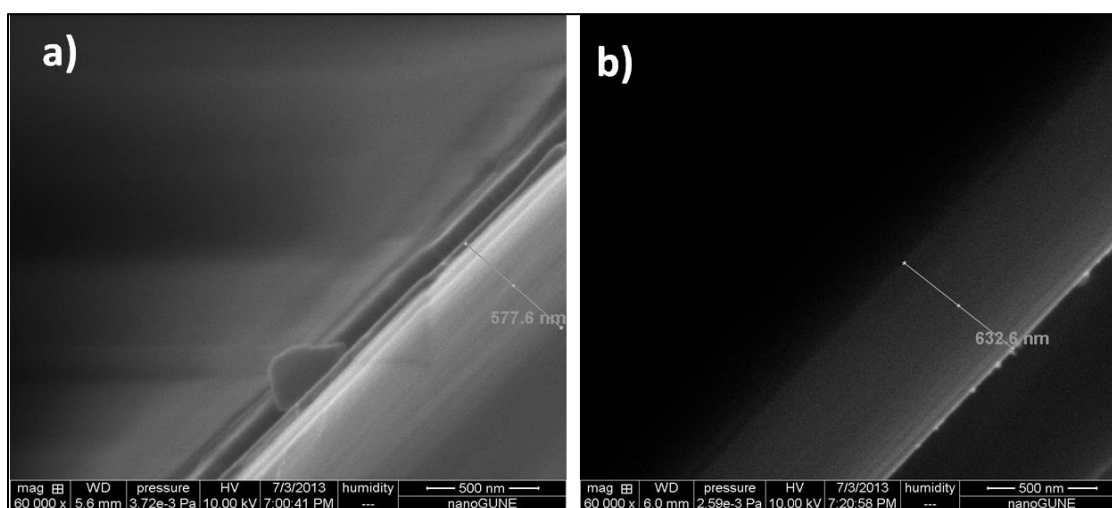


Figure 4.2 2ZnO-EG Cross-section SEM micrograph; a) and b) lamellar overview.

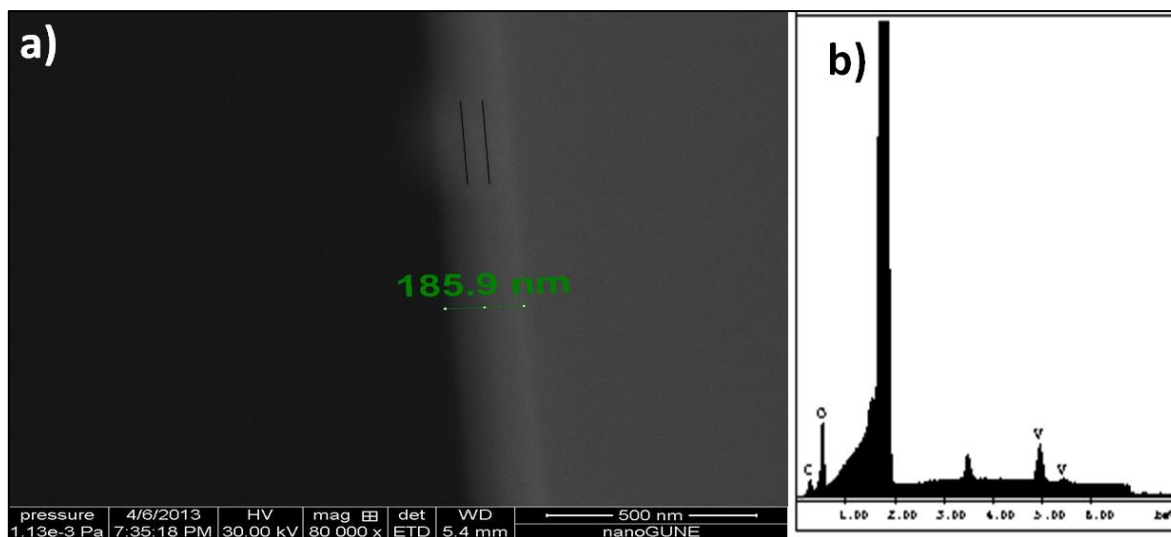
4.2.3 2α - V_2O_5 -T ALD-MLD.

Figure 4.3 2α - V_2O_5 -T cross-section SEM micrograph; a) lamellar nanostructures, and b) EDX-analysis.

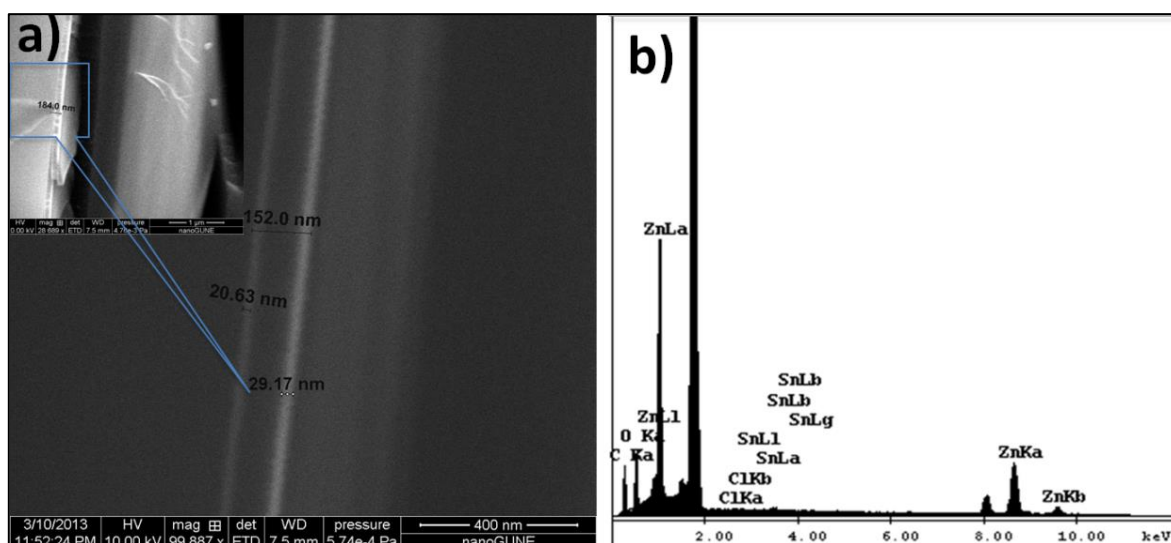
4.2.4 ZnO-T- Sn_xO_y ALD-MLD-ALD.

Figure 4.4 ZnO-T- SnO_2 cross-section SEM micrograph; a) lamellar nanostructures and b) EDX-analysis.

4.2.5 Al₂O₃-SnO₂- AIOT- Mn_xO_y (ALD-MLD-ALD).

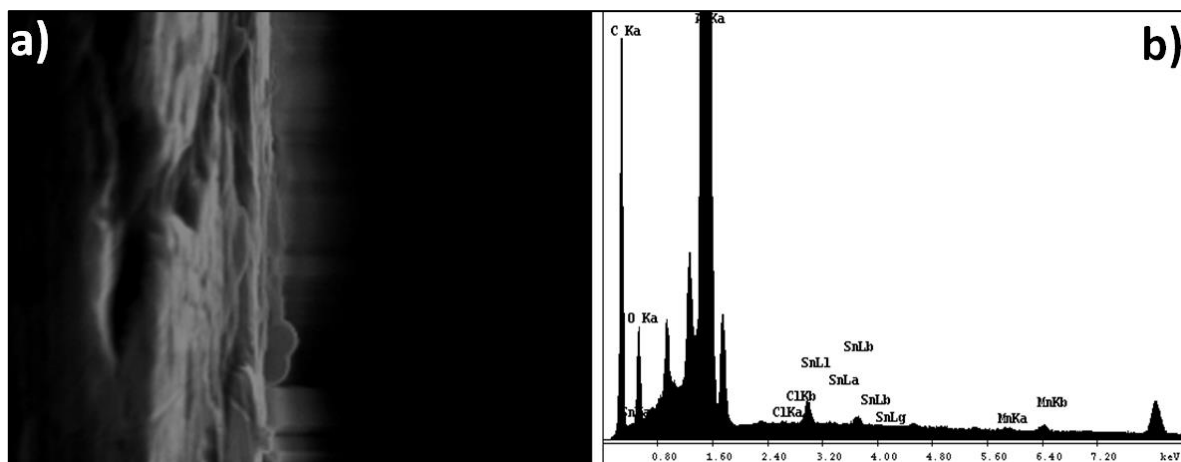


Figure 4.5 SiO₂-Cu-Al₂O₃-SnO₂(anode)- AIOT (polymer electrolyte)- Mn_xO_y (Cathode) cross-section SEM micrograph; a) lamellar nanostructures and b) EDX- analysis.

"I have always considered the search for the absolute as the highest goal of all scientific activity ...
and I set to work with passion"

Max Planck